

Titre: On the Aluminium Alloy Design Using Molecular Dynamics
Title:

Auteur: Juan-Ricardo Castillo-Sánchez
Author:

Date: 2022

Type: Mémoire ou thèse / Dissertation or Thesis

Référence: Castillo-Sánchez, J.-R. (2022). On the Aluminium Alloy Design Using Molecular Dynamics [Master's thesis, Polytechnique Montréal]. PolyPublie.
Citation: <https://publications.polymtl.ca/10541/>

 **Document en libre accès dans PolyPublie**
Open Access document in PolyPublie

URL de PolyPublie: <https://publications.polymtl.ca/10541/>
PolyPublie URL:

Directeurs de recherche: Jean-Philippe Harvey, & Aïmen E. Gheribi
Advisors:

Programme: Génie chimique
Program:

POLYTECHNIQUE MONTRÉAL

affiliée à l'Université de Montréal

On the aluminium alloy design using molecular dynamics

JUAN RICARDO CASTILLO SANCHEZ

Département de génie chimique

Mémoire présenté en vue de l'obtention du diplôme de *Maîtrise ès sciences appliquées*

Génie chimique

Août 2022

POLYTECHNIQUE MONTRÉAL

affiliée à l'Université de Montréal

Ce mémoire intitulé :

On the aluminium alloy design using molecular dynamics

présenté par **Juan Ricardo CASTILLO SANCHEZ**

en vue de l'obtention du diplôme de *Maîtrise ès sciences appliquées*

a été dûment accepté par le jury d'examen constitué de :

Patrice CHARTRAND, président

Jean-Philippe HARVEY, membre et directeur de recherche

Aimen GHERIBI, membre et codirecteur de recherche

Alain ROCHEFORT, membre

DEDICATION

*To my parents, Juan and Josefina.
For their love, endless support, and encouragement.
I appreciate everything that you have done for me.*

ACKNOWLEDGEMENTS

First and foremost, I have to thank my research supervisors Professor Jean-Philippe Harvey and Dr. Aïmen E. Gheribi. I would like to thank Antoine Rincant, the *Centre de Caractérisation Microscopique des Matériaux* (CM)², the Centre for Research in Computational Thermochemistry (CRCT), and the Digital Research Alliance of Canada. I would like to extend my sincere thanks to the Constellium Technology Center (C-TEC) and to Dr. Georges Salloum-Abou-Jaoude for hosting me during an internship for the experimental part of this work. I would like to show gratitude to my committee members, Professor Patrice Chartrand and Professor Alain Rochefort, for their careful reading of the master's thesis and for their insightful comments and suggestions. I would like to say a special thank you to The Ministry of Education and Higher Education of Quebec (*Ministère de l'Éducation et de l'Enseignement Supérieur du Québec*) for covering most of my tuition fees as an international student and to the Department of Chemical Engineering of *Polytechnique Montréal* for the financial support.

RÉSUMÉ

Le présent travail porte sur le développement des alliages d'aluminium à l'aide de la dynamique moléculaire (MD, son acronyme commun en anglais), la thermodynamique classique ainsi que des essais expérimentaux. La combinaison de ces outils facilite la compréhension de la physique des procédés lors de l'élaboration des nouveaux alliages. Elle identifie leurs limites d'application et leurs possibilités d'amélioration. Traditionnellement, la thermochimie est utilisée pour déterminer l'assemblage de phases et les coûts énergétiques lors du design des alliages. De plus, le développement rapide d'outils informatiques permet d'étudier la dynamique des systèmes métalliques à la meso-échelle, c'est-à-dire entre 10 nm et 1 μ m (voir Figure 0.1). Par ailleurs, des essais expérimentaux sont requis pour l'amélioration des outils numériques.

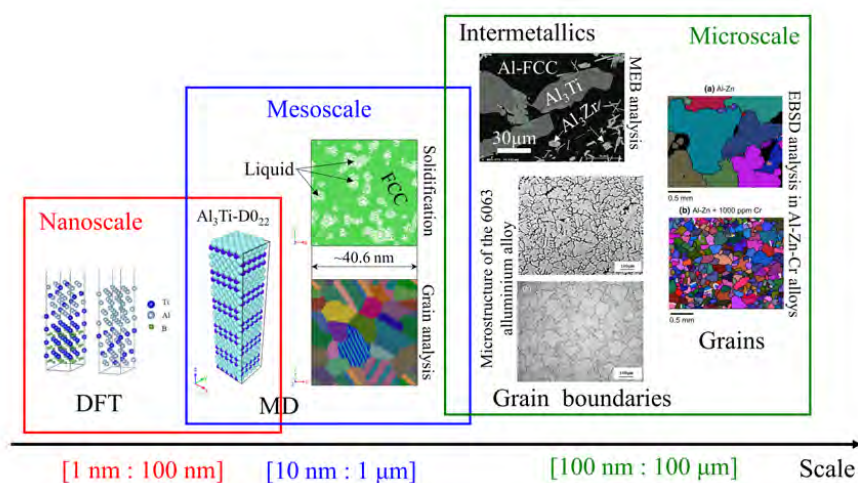


Figure 0.1 Schéma montrant les différentes échelles de grandeur utilisées dans ce travail selon la définition d'échelle de Yen et al. [1]. L'image DFT a été tirée de [2], la microstructure de l'alliage d'aluminium 6063 a été obtenue de [3], les images EBSD pour les alliages Al-Zn-Cr ont été adaptées de [4].

Les applications de la MD se concentrent sur deux aspects principaux : la description thermodynamique des systèmes solides et liquides ; et l'étude de la solidification des alliages. La transférabilité des potentiels interatomiques actuels en MD a été analysée sur la modélisation des solides et liquides dans les systèmes constitués de : Zr, Al-Cu, Al-Cr et Al-Zr-Ti. Les études de solidification couvrent trois cas : La solidification de l'aluminium pure, l'effet de l'ordre icosaédrique sur la nucléation de la phase FCC dans des alliages Al-Cr et la précipita-

tion des intermétalliques Al_3Zr (D0_{23}) and Al_3Ti (D0_{22}) dans le système Al-Zr-Ti. Ce dernier cas a été aussi exploré expérimentalement en incluant le Si dans le système Al-Si-Zr-Ti. Les résultats des simulations révèlent que les modèles de potentiels interatomiques actuels en MD ne peuvent être extrapolés correctement pour des systèmes multicomposants, ceci est dû aux hypothèses propres au formalisme pour la paramétrisation des forces intermoléculaires. C'est-à-dire, à cause de la simplification des contributions énergétiques par paires. Cependant, la description des systèmes métalliques reste acceptable pour des cas spécifiques et systèmes simples. La solidification, étant un phénomène complexe, ne peut pas être modélisée proprement avec la MD classique pour les raisons suivantes : (1) Limitation des ressources computationnelles : actuellement la taille et le temps de simulations sont amplement courts par rapport aux cas d'étude réels, même en utilisant des superordinateurs. (2) Non-homogénéité des potentiels interatomiques : Il existe plusieurs formalismes pour décrire les interactions intermoléculaires, malheureusement, la description énergétique de phases avec ces potentiels peut changer fortement d'un formalisme à l'autre. Ceci amène des erreurs supplémentaires durant l'intégration de plus d'éléments dans le système. Donc, la modélisation des alliages à haute entropie (High-Entropy Alloys) devient difficile. (3) Manque de description entropique : Puisque la MD est basée sur des apports purement enthalpiques, l'effet entropique n'est pas considéré lors d'une simulation classique, ce qui empêche la prédiction des phases primaires lors d'un refroidissement. Quand la teneur des éléments d'alliage dépasse la limite acceptée pour cristalliser la phase α -Al FCC, des verres métalliques sont obtenus. En revanche, la MD donne accès aux propriétés physiques à pression et température constantes. Aussi, elle donne également des indices sur les phénomènes de nucléation en accord avec la théorie de la nucléation de la phase FCC assisté par l'ordre icosaédrique dans le system simple Al-Cr.

Les essais expérimentaux ont été réalisés sur un montage innovant basé sur la technologie *Porous Disc Filtration Apparatus (PoDFA)*. Les résultats sur la précipitation des phases Al_3Zr et Al_3Ti ont montré que la cinétique de précipitation peut décaler l'équilibre de phases primaires prévues par la thermodynamique classique. Les intermétalliques Al_3Ti sont cinétiquement favorisés par rapport aux intermétalliques Al_3Zr . La cristallographie de ces intermétalliques a été confirmée par microscopie électronique à transmission. La substitution des sites de sous-réseau Al par le Si a été quantifiée par Microscopie Electronique à Balayage (MEB). *FactSage*, étant un logiciel spécialisé en métallurgie, a confirmé qu'une telle substitution est possible pour la phase de nature $\text{Al}_{3-x}\text{Si}_x(\text{Ti}_{y-1}\text{Zr}_y)\text{-D0}_{22}$. Tandis que pour le modèle actuel de la phase $\text{Al}_3(\text{Zr}_{1-x},\text{Ti}_x)\text{-D0}_{23}$, le Si n'est pas considéré dans sa liste de *end-members* des bases de données. Finalement, il a été expérimentalement montré que les intermétalliques tétraogonales type Al_3X ($\text{X}=\text{Zr},\text{Ti}$) agissent comme des sites de nucléation pour la phase FCC. Et donc, ils pourront être utilisés comme affinant des grains.

ABSTRACT

This master's thesis focuses on the applications of classical Molecular Dynamics (MD) simulations for the design of aluminum alloys. The predicting capability of this emerging tool has been compared to classical thermodynamics and experimental work. MD has gained popularity as a result of the accelerated development of computer science. Current computational resources already allow to perform simulations at the mesoscale, i.e. between 10 nm and 1 μm (see Figure 0.2). Nevertheless, most force field models are still based on pairwise interactions. Limitations of such as approximation have been identified for a series of applications of interest for aluminum alloy design.

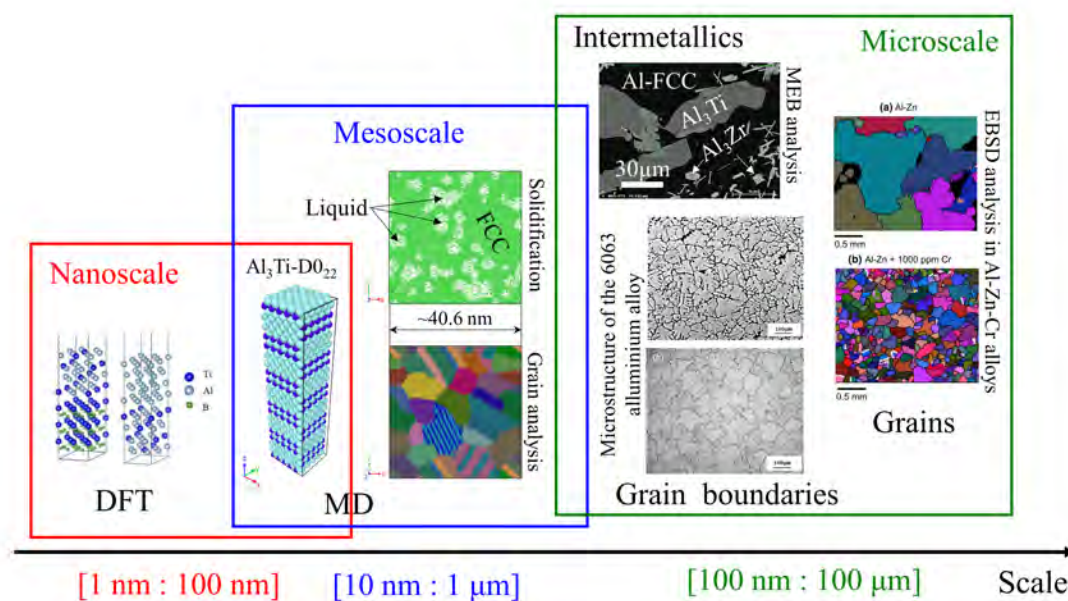


Figure 0.2 Diagram showing the different length scales used in this work according to the scale definition of Yen et al. [1]. The DFT image was taken from [2], the microstructure of the 6063 aluminum alloy was obtained from [3], EBSD images for the Al-Zn-Cr alloys were adapted from [4].

MD simulations of this work include two main aspects: 1. Metallic solution modeling and 2. Solidification of aluminum alloys. Systems analyzed for solution modeling were Zr, Al-Cu, Al-Cr, and Al-Ti-Zr. Solid and liquid solutions were evaluated and compared to experiments, first-principles calculations, and other interatomic potentials when available in the literature. Overall, it has been confirmed that the modified embedded-atom method (MEAM) formal-

ism for modeling interatomic interactions is robust enough for describing metallic systems. However, it is not transferable for simultaneous modeling of liquids and anisotropic solids. Its predicting capability is also weakened as more elements are included in a system. Simulations of Zr have shown that there is a strong correlation between unary interactions of a liquid and the allotrope used during potential parametrization. The effect of a reference structure for the Al-Cu interactions has been studied. Three metastable binary compounds were used to show that the universality of MEAM potentials is questionable and highly dependent on the users' compound choice. Modeling of the Al-Cr interactions has demonstrated that the MEAM potential is partially transferable for solution modeling but still robust enough when compared to other interatomic potentials available in the literature.

Large-scale MD studies for solidification were concentrated in pure Al, Al-Cr alloys, and Al-Zr-Ti alloys. Simulations for pure Al and Al-Cr alloys have been performed using a Finnis and Sinclair (FS) interatomic potential available in the literature and with a MEAM potential developed in this work. Notably, melting and solidification have been found to be affected by the formalism of the interatomic potential. MEAM potential showed the best predicting capability for primary solidification of the α -FCC phase. Moreover, simulations with the MEAM formalism were in agreement with the icosahedral-enhanced nucleation theory of the α -Al phase in Al-Cr alloys. A clear correlation between the local structure and nucleation was observed. Simulations for the prediction of primary phases within the Al-Cr and Al-Zr-Ti systems were explored. The latter is geared to the precipitation of Al_3X ($\text{X}=\text{Zr},\text{Ti}$) phases. Precipitation of primary phases other than the FCC and HCP phases was not achieved. MD's limitations for describing the solidification of multi-component systems were discussed. Such restrictions are related to MD's short time/length scales and the missing entropic effects for classical MD simulations.

Finally, solidification of Al-Si-Ti-Zr alloys was carried out experimentally. In the same way as in the MD simulations, these experiments were targeted toward the precipitation of Al_3X ($\text{X}=\text{Zr},\text{Ti}$) intermetallics. An innovative setup based on Porous Disc Filtration Apparatus (PoDFA) technology is presented for the synthesis of primary phases. Si sublattice substitution within Al sites of Al_3X ($\text{X}=\text{Zr},\text{Ti}$) $\text{D}0_{22}$ and $\text{D}0_{23}$ intermetallics was quantified. This finding is a benchmark for further refinement of current thermodynamic models stored in the FTlite database of the FactSage software. TEM results showed that Al_3X intermetallics acted as nucleant particles for the Al-FCC phase. As such, they can be used for grain refinement purposes in aluminum alloy design.

TABLE OF CONTENTS

DEDICATION	iii
ACKNOWLEDGEMENTS	iv
RÉSUMÉ	v
ABSTRACT	vii
TABLE OF CONTENTS	ix
LIST OF TABLES	xiii
LIST OF FIGURES	xiv
LIST OF SYMBOLS AND ACRONYMS	xxi
LIST OF APPENDICES	xxii
CHAPTER 1 INTRODUCTION	1
1.1 Context	3
1.1.1 Aluminum alloys and V-lab project	3
1.1.2 Availability of supercomputers	4
1.2 History of the project	5
CHAPTER 2 LITERATURE REVIEW	6
2.1 Aluminium alloys	6
2.1.1 Cu in 2xxx and 2xx.x series	7
2.1.2 Si in 4xxx, 6xxx, 4xx.x, 3xx.x and series	7
2.1.3 Ti and Zr in aluminium alloys	8
2.1.4 Cr in aluminum alloys	8
2.2 Theory of solidification	8
2.2.1 Nucleation	8
2.2.2 Classical Nucleation Theory (CNT)	9
2.2.3 Two-Step Nucleation Theory	9
2.3 Grain refiner theories in Al-alloys	10

2.3.1	Grain refinement by Grain Refiner (GR)	10
2.3.2	Icosahedral quasicrystal-enhanced nucleation of the fcc phase	12
2.3.3	Grain refinement by rapid Solidification (RS)	13
2.4	State-of-the-art of MD in real alloys	14
2.4.1	Homogeneous nucleation	14
2.4.2	Heterogeneous nucleation	14
2.4.3	Effect of Cr on the icosahedral-enhanced nucleation of the fcc phase	15
CHAPTER 3 GAP OF KNOWLEDGE AND OBJECTIVES		16
3.1	General objective	16
3.2	Specific objectives	16
CHAPTER 4 METHODOLOGY		18
4.1	Classical Molecular Dynamic (MD) simulations	18
4.1.1	Equations of motion	18
4.1.2	Force field models	19
4.1.3	Size of simulation cells and its effect on solidification	19
4.2	Experimental work: Al-Si-Zr-Ti alloys	23
4.2.1	PoDFA setup	23
4.2.2	Characterization	23
4.2.3	Crystallographic determination	25
CHAPTER 5 ARTICLE 1 : ON THE TRANSFERABILITY OF CLASSICAL PAIRWISE ADDITIVE ATOMISTIC FORCE FIELD TO THE DESCRIPTION OF UNARY AND MULTI-COMPONENT SYSTEMS: APPLICATIONS TO THE SOLIDIFICATION OF AL-BASED ALLOYS		26
5.1	Abstract	26
5.2	Introduction	27
5.3	Force field development	31
5.4	Simulations details	37
5.4.1	Thermodynamic property evaluation	38
5.4.2	MD simulations of solidification and precipitation	38
5.4.3	Energetics of partially ordered D0 ₂₂ and D0 ₂₃ solid solutions	39
5.5	Results and discussion	40
5.5.1	Effect of the reference structure on the modeling of liquid Zr	40
5.5.2	Potential transferability when evaluating the enthalpy of mixing of binary liquid solutions	41

5.5.3	Potential transferability for describing the internal structure of the $\text{Al}_{80}\text{Cu}_{20}$ melt	43
5.5.4	Potential transferability for the energetic description of isotropic and anisotropic solids	47
5.5.5	MD simulations of the crystallization of pure aluminum	49
5.5.6	Crystallization of model Al-Cr alloys by icosahedral-enhanced nucleation	53
5.5.7	Crystallization of Al-Zr-Ti alloys	63
5.5.8	Modelling of pseudo-binary solid solutions: $\text{Al}_3(\text{Zr,Ti})\text{-D0}_{23}$ and $\text{Al}_3(\text{Ti,Zr})\text{-D0}_{22}$	68
5.6	Conclusions	71
5.7	Acknowledgements	72
5.8	Acknowledgement of submission	72
CHAPTER 6 SYNTHESIS AND CHARACTERIZATION OF $(\text{AL,SI})_3(\text{ZR,TI})\text{-D0}_{23}$ AND $(\text{AL,SI})_3(\text{TI,ZR})\text{-D0}_{22}$ INTERMETALLICS: REVEALING SILICON SUBLATTICE SUBSTITUTION AND INTERMETALLIC ENHANCED NUCLEATION OF THE α -Al PHASE		73
6.1	Abstract	73
6.2	Introduction	73
6.3	Experimental procedures	78
6.4	Results	79
6.4.1	Chemical composition of molten alloys and their equilibrium phase diagram	79
6.4.2	Microstructural analysis	79
6.4.3	Phase identification	80
6.4.4	Thermodynamic calculations	83
6.4.5	Crystallographic analysis	86
6.4.6	Elemental mapping analysis	93
6.5	Conclusions	93
CHAPTER 7 GENERAL DISCUSSION		95
CHAPTER 8 CONCLUSION		97
8.1	Summary of works	97
8.2	Limitations	98
8.3	Future Research	98

REFERENCES 99

APPENDICES 122

LIST OF TABLES

Table 5.1	2NN-MEAM potential parameter sets for pure Al, Zr, Cu, Cr and Ti. The units of the cohesive energy E_c , equilibrium nearest-neighbor distance r_e , and bulk modulus B are eV, Å and 10^{12} dyne/ cm ² , respectively. The reference structure for Al and Cu is fcc, bcc for Cr, hcp for Ti and two references for Zr, i.e. bcc and hcp.	33
Table 5.2	Optimized 2NN-MEAM potential parameters for individual binary systems. The units of the cohesive energy E_c , equilibrium nearest-neighbor distance r_e , and bulk modulus B are eV, Å and 10^{12} dyne/ cm ² , respectively.	36
Table 5.3	Default value for MEAM-2NN potential parameters of the Ti-Zr-Al ternary system.	37
Table 5.4	Crystallization of Al-Ti-Zr alloys	39
Table 5.5	Calculated enthalpy of formation (eV/atom) for Al-Cu metastable compounds. Results are compared to other MD models and first-principle calculations.	47
Table 5.6	Enthalpy of formation of different Al-Cr solid compounds at 0K compared with first-principle calculations and MD simulations. Formation energies are reported in eV/atom.	48
Table 5.7	Enthalpy of formation of different solid compounds within the Al-Zr-Ti system compared with first-principle calculations. Formation energies are reported in eV/atom.	48
Table 5.8	Lattice parameters and elastic constant of Al ₃ Zr-D0 ₂₃ , Al ₃ Ti-D0 ₂₂ and Zr ₂ TiAl compounds by MD simulations compared to DFT calculations.	69
Table 6.1	Nominal composition of S2 and S6 molten alloys and their corresponding equilibration temperature.	79
Table 6.2	Chemical composition of phases reported in Figure 6.4	82
Table 6.3	Summary of lattice parameters for the different phases synthesized in this work compared to values from the literature. Lattice misfit between the intermetallics and the α -Al phase are also presented.	90

LIST OF FIGURES

Figure 0.1 Schéma montrant les différentes échelles de grandeur utilisées dans ce travail selon la définition d'échelle de Yen et al. [1]. L'image DFT a été tirée de [2], la microstructure de l'alliage d'aluminium 6063 a été obtenue de [3], les images EBSD pour les alliages Al-Zn-Cr ont été adaptées de [4].	v
Figure 0.2 Diagram showing the different length scales used in this work according to the scale definition of Yen et al. [1]. The DFT image was taken from [2], the microstructure of the 6063 aluminum alloy was obtained from [3], EBSD images for the Al-Zn-Cr alloys were adapted from [4].	vii
Figure 1.1 Diagram showing the main computational tools available at CRCT (left side) in order to optimize thermodynamic databases for the industrial partners (right side) within the V-lab collaboration.	4
Figure 2.1 Sketch of the free energy of formation of a nucleus, as a function of the crystalline nucleus size for homogeneous nucleation (purple), heterogeneous nucleation (green), and spinodal decomposition (orange) showing the maximum of energy to overcome to promote the formation of the nuclei. Taken from [5].	10
Figure 2.2 Sketch of two-step nucleation theory and its free energy barriers to overcome. Taken from [6].	11
Figure 2.3 Electron Backscatter Diffraction (EBSD) analysis of Al-Zn-Cr alloys, with (b) and without (a) Cr. Different orientations of grains are represented with different colors. Adapted from [4].	13
Figure 2.4 Representation of the iQC-mediated nucleation mechanism. Taken from [7].	13
Figure 4.1 Initial and final configurations of melting and re-solidification simulations of pure Cu starting with a perfectly ordered FCC structure. Local ordering was evaluated with the Polyhedral Template Matching (PTM) reported by Larsen et al. [8]. Orientation of atoms is displayed by colors: green (FCC), red (HCP), blue (BCC), yellow (icosahedral), purple (Simple cubic) and gray (other).	20

Figure 4.2	Representation of the quasi-two-dimensional cells proposed by (a) Shibuta et al. [9] during their study on the homogeneous solidification of iron, and by (b) Zhan et al. [10] for the solidification on an Al-Cu alloy. " a_0 " in (b) stands for the lattice constant of Al-FCC.	21
Figure 4.3	Evolution of temperature (a), the FCC-oriented local ordering fraction (b), and the icosahedral ordering (c), as a function of the simulation time (ns) for different simulation boxes exposed to the thermal program, which consisted of linear heating, isothermal holding and linear coolings.	22
Figure 4.4	Diagram showing different steps during the synthesis of intermetallics in a PoDFA setup	23
Figure 4.5	Polishing for light and electron microscopy analysis	24
Figure 4.6	Polishing for TEM analysis.	24
Figure 5.1	Enthalpy of formation of different compounds from DFT calculations (black spheres) [11] compared with the solid (25°C) and liquid (1500°C) enthalpies of formation computed to the critically assessed value [12].	34
Figure 5.2	Enthalpy of formation of different compounds from DFT calculations (black spheres) [11], and the hypothetical Zr_3Ti-L1_2 reference (black triangle) compared with the solid enthalpy of formation at 25°C computed to the critically assessed value [12].	35
Figure 5.3	Ti-Zr phase diagram computed with Factsage [12]. Filled triangles, squares and circles are experimental data obtained from [13].	35
Figure 5.4	(a) Total Radial Distribution Function (RDF) for liquid Zr at 2000 K computed with MD for BCC (blue line) as reference structure and HCP (red line) as reference structure using the MEAM formalism. Diamond symbols are results from <i>Ab Initio</i> Molecular Dynamics at 2000 K from Jakse & Pasturel [14]. Dark yellow circles correspond to experimental data of Schenk et al [15]. The Angular Distribution Function (ADF) is presented in (b) for liquid Zr at 2000 K for BCC as reference structure (blue line) and HCP as reference structure (red line). Diamond symbols are results from <i>Ab Initio</i> Molecular Dynamics at 2000 K from Jakse & Pasturel [14].	42

- Figure 5.5 Molar enthalpy of mixing for liquid Al-Cu. Filled circles and line are the thermodynamic data calculated with MD at $T=1500$ K. Experimental data from Stolz et al. [16] (orange triangles) at 1467 K, Kanibolotsky et al. [17] (blue triangles) at 1590 K, Gizenko et al. [18] (purple squares) at 1473 K, and Sandakov et al. [19] (cyan triangles) at 1773 K are presented as filled symbols. Dashed line are results at 1500 K from classical thermodynamics performed with FactSage [12]. 43
- Figure 5.6 Enthalpy of mixing at 2000K calculated with MD using the MEAM potential (filled blue circles and line) and the FS potential (filled red circles and line) [20]. Experimental data from Saltykov et al. [21] (orange triangles) at 1723 and Sudavtsova et al. [22] (cyan triangles) at 1920 K are as open symbols. Dashed line are results at 2100 K from classical thermodynamics performed in FactSage [12]. Shaded grey zone correspond to the meta-stability zone of the liquid at 2000K. 44
- Figure 5.7 Molar enthalpy of mixing for liquid Al-Zr. Open circles and line are the thermodynamic data calculated with MD at $T=2000$ K. Experimental data from Esin et al. [23] (diamonds) at 1970 K, Sudavtsova et al. [24] (squares) at 1790 K, and Witusiewicz et al. [25] (triangles) at 2080 K are presented as open symbols. Dashed line are results at 2000 K from classical thermodynamics performed in FactSage [12]. The shaded grey zone corresponds to the meta-stability zone of the liquid at 2000K. 44
- Figure 5.8 Molar enthalpy of mixing for liquid Ti-Zr. Open circles and line are the thermodynamic data calculated with MD at $T=2000$ K. Dashed line are results at 2000 K from classical thermodynamics performed in FactSage [12]. Shaded grey zone correspond to the meta-stability zone of the liquid at 2000K. 45
- Figure 5.9 Calculated total (a), and partial Al-Cu (b), Al-Al (c) and Cu-Cu (d) radial distribution functions for liquid $\text{Al}_{80}\text{Cu}_{20}$ at 1818 K. Results from different classical MD models are compared to AIMD data. The first nearest neighbor distance (r_{1NN}), the shell of the first nearest neighbors (r_{1NN}^{shell}), and the total coordination number (Z) are indicated. 46

Figure 5.10 Scheme for time versus temperature during the classical MD simulation of melting/cooling of pure aluminum using the FS and MEAM potentials. Snapshots of simulated microstructures at specific simulation times are reported. Only FCC-oriented atoms are presented in the simulation boxes. Systems were first equilibrated into the NVT ensemble at 2.5 K for 0.5 ns. NPT heating at 1.66 K/s was subsequently imposed. Then, NVT equilibration was carried at 2000K during 0.5 ns followed by 0.5 ns of NPT modeling at the same temperature. Cooling was executed at -1K/ps. Finally, systems were equilibrated at 300K.	51
Figure 5.11 Time-temperature evolution of the local ordering in solid/liquid aluminum, calculated via the Polyhedral Template Matching method [8,26]. Calculated values with the MEAM potential (solid lines) in comparison with that obtained with the FS interatomic potential [20] (dashed lines).	52
Figure 5.12 Different perspectives of an Al ₁₂ Cr icosahedral cluster equilibrated at 0K (Al is in grey, Cr is in red).	52
Figure 5.13 Simulated partial local ordering via FS potential at specific simulation steps. Icosahedral-oriented atoms are presented in yellow and FCC in green.	53
Figure 5.14 Representation of the initial configurations for the simulations of Al-Cr alloys (Al atoms are presented in grey, Cr atoms are in red). Cr atoms were randomly distributed across an FCC simulation box followed by a volume minimization.	55
Figure 5.15 Computed Al-Cr phase diagram using the FTlite database. The different compositions studied in this work are indicated with dashed lines.	55
Figure 5.16 Simulated microstructures for Al-Cr alloys at different compositions. The local ordering was determined via Common-Neighbor Analysis (CNA) and Polyhedral Template Matching (PTM).	56
Figure 5.17 Simulated temperature vs time for the different Al-Cr alloys. The inside figure shows the zoom of temperature perturbations during the cooling, which corresponds to the latent energy release of solidification.	57
Figure 5.18 Evolution of the icosahedral fraction over simulation time for different Al-Cr alloys using the MEAM (top) and FS (bottom) potentials.	59
Figure 5.19 Maximum icosahedral-related undercooling in Al-Cr alloys.	59
Figure 5.20 Solidification stages correlated with the icosahedral ordering and the stationary point in the cooling curves of Al-Cr alloys.	60
Figure 5.21 Total energy versus temperature of for the different Al-Cr simulations during cooling.	60

Figure 5.22 Analysis of the local ordering via PTM analysis (first column) compared to the grain segmentation analysis for different Al-Cr alloys.	62
Figure 5.23 Initial configurations for two model aluminum alloys showing only Zr and Ti inside the Al-FCC. a) and b) correspond to Sample 1 (S1), which contains 0.11 wt% of Zr and 0.18 wt% of Ti. c) and d) stand for Sample 2 (S2), having 0.23 wt% of Zr and 1.2 wt% of Ti.	63
Figure 5.24 Phase diagrams generated with FactSage [12] showing the isoplethal section (gray dashed lines) for samples S1 (a) and S2 (b). Sample S1 contains 0.11 wt% of Zr and 0.18 wt% of Ti. Sample S2 has 0.23 wt% of Zr and 1.2 wt% of Ti.	64
Figure 5.25 Simulation time vs temperature for samples S1 and S2 using the Al-Zr-Ti MEAM potential. Both simulations were first equilibrated into the NVT ensemble at 2.5 K for 0.1 ns. NPT heating at 2.3 K/s was subsequently imposed. Then, NPT equilibration was carried at 2073.15K during 1 ns. Cooling was executed at -1K/ps up to 1073.15 K. A second equilibration took place at 1073.15K during 1 ns follow by cooling at -1K/ps up to 298.15 K. Finally, systems were equilibrated at 298.15 K.	65
Figure 5.26 Simulation time versus partial local ordering in samples S1 and S2. FCC, HCP, and Icosahedral configurations were computed using the Polyhedral Template Matching (PTM) [8].	65
Figure 5.27 Local ordering was computed with PTM for S1 and S2 simulation boxes at 4.5 ns, 4.6 ns, and 6 ns. FCC(green) and icosahedral (yellow) oriented atoms are presented independently. An additional picture showing the HCP (red) along with FCC and icosahedral ordering is provided.	66
Figure 5.28 a), b) c) and d) show the final orientation of Zr and Ti atoms in the last simulations cells (6ns) for simulations S1 and S2. e) and f) show the percentage of the local ordering of Zr and Ti atoms respectively.	67
Figure 5.29 Pseudo-binary $\text{Al}_3(\text{Zr,Ti})\text{-D0}_{23}$ solid solution	70
Figure 5.30 Pseudo-binary $\text{Al}_3(\text{Ti,Zr})\text{-D0}_{22}$ solid solution.	70
Figure 5.31 Acknowledgment of receipt of submitted article to <i>Physical Chemistry Chemical Physics</i>	72
Figure 6.1 Diagram showing different steps during the synthesis of intermetallics in a PoDFA setup	78
Figure 6.2 Equilibrium phase diagrams for samples S2(a) and S6(b) obtained with FTlite database of FactSage. Black squares correspond to the experimental equilibration temperature before filtration in PoDFA setup	80

- Figure 6.3 Light microscopy micrographs at x100 magnification for solidified samples: S2 (b) and S6 (c). An example of the zone of analysis for the polished samples is presented in (a). 80
- Figure 6.4 Scanning electron microscope (SEM) micrographs. (a) and (b) correspond to sample S2, (c), (d) and (e) stand for sample S6. Green letters highlight the different phases within each sample. The chemical composition of the phases is reported in Table 6.2. 82
- Figure 6.5 Activities of $D0_{22}$ and $D0_{23}$ phases in samples S2 (a) and S6(b) considering variations on the concentration of Zr, the maximum in the x-axis corresponds to the actual amount of Zr in the studied alloys. Evolution of elements inside $D0_{22}$ and $D0_{23}$ phases (contemplating Zr variations) for samples S2 (c and e) and S6 (d and f) are also reported. Thermodynamic calculations were computed at the target equilibrium temperature in PoDFA setup, i.e. at 703°C for sample S2 and 716°C for S6; and by keeping constant the concentrations of Ti and Si as reported in Table 6.1. Symbols are the experimental molar fractions of phases reported in Table 6.2. 85
- Figure 6.6 Summary of the TEM analysis performed for sample S2. (a) and (b) are micrographs showing the target zone for FIB sectioning (blue rectangle) to obtain a FIB lamella (c). Selected area electron diffraction patterns are presented in (d), (e) and (f) for the α -phase; (g), (h) and (i) for the $\text{Al}_{2.98}\text{Si}_{0.02}\text{Ti}-D0_{22}$ phase; and (j), (k) and (l) for the $\text{Al}_{2.99}\text{Si}_{0.01}\text{Ti}_{0.93}\text{Zr}_{0.07}-D0_{22}$ phase. 87
- Figure 6.7 Summary of the TEM analysis performed for sample S6. (a) and (b) are micrographs showing the target zone for FIB sectioning (blue rectangle) to obtain a FIB lamella (c). Selected area electron diffraction patterns are presented in (d), (e) and (f) for the $\text{Al}_3\text{Ti}-D0_{22}$ phase; (g), (h) and (i) for the grain "G2" of the $\text{Al}_3\text{Zr}-D0_{23}$ phase; (j), (k) and (l) for grain "G1" of the $\text{Al}_3\text{Zr}-D0_{23}$ phase. m) and n) show the crystallographic coherence between α -phase/ $\text{Al}_3\text{Ti}-D0_{22}$ and α -phase/ $\text{Al}_3\text{Zr}-D0_{23}$, respectively. 89
- Figure 6.8 Lattice parameters for some intermetallic phases found in sample S2 (brown squares and dark red diamond) and sample S6 (orange squares). Compared to MD (red circles) and DFT (blue circles) calculations from [27], DFT (magenta open circles) from [28], a fitting with the Vegard's rule (purple line) of [29] and the "a" parameter of Al-FCC from DFT calculations from [11]. 92
- Figure 6.9 Electron microprobe elemental maps for sample S2. (a) Al map, (b) Si map, (c) Ti map and (d) Zr map. 93

Figure 6.10 Electron microprobe elemental maps for sample S6. (a) Al map, (b) Si map, (c) Ti map and (d) Zr map.	94
Figure A.1 Al-Cu phase diagram.	122
Figure A.2 Al-Si phase diagram.	122
Figure A.3 Al-Ti phase diagram.	123
Figure A.4 Al-Zr phase diagram.	123
Figure A.5 Al-Cr phase diagram.	124
Figure B.1 Example of thermal program for an Al-Cr alloy.	125

LIST OF SYMBOLS AND ACRONYMS

MD	Molecular Dynamics
LAMMPS	Large-scale Atomic/Molecular Massively Parallel Simulator
KISSMD	Kinetic Simulation System based on Molecular Dynamics
AIMD	Ab initio Molecular Dynamics
DFT	Density-Functional Theory
CALPHAD	CALculation of PHAse Diagrams
CNT	Classical Nucleation Theory
RDF	Radial Distribution Function
ADF	Angle Distribution Function
MEAM	Modified Embedded-Atom Method
FS	Finnis and Sinclair Formalism
ADP	Angular-Dependent Potential
PoDFA	Porous Disc Filtration Apparatus
SEM	Scanning Electron Microscopy
EDX	Energy-Dispersive X-ray Spectroscopy
EMP	Electron Microprobe
TEM	Transmission Electron Microscopy
FIB	Focused Ion Beam

LIST OF APPENDICES

Appendix A	Binary phase diagrams for the studied aluminum alloying elements	122
Appendix B	Example of input file for LAMMPS	125

CHAPTER 1 INTRODUCTION

Solidification plays an important role in metal alloy manufacturing processes. Casting is one of the principal techniques to produce aluminum alloy ingots and parts [30,31]. In fact, 90% of the processed metals used in the industry are obtained from at least one pyrometallurgical operation involving a metallic melt [32]. The resulting microstructures from solidification are made up of various phases and have a direct effect on the mechanical and physical properties of the alloy [33–35]. Scientists can rely on classical thermodynamics to predict the equilibrium phases for a given mass balance and under certain constraints (e.g., pressure, temperature, chemical potential, para-equilibrium stoichiometry, etc.) [36, 37]. Since pressure is usually constant during solidification, these diagrams are usually computed as a function of temperature and with composition variations of alloying components. This allows to obtain the optimal conditions to assist precipitation of desired primary phases. Nevertheless, solidification of secondary and/or ternary phases does not necessarily follow the *equilibrium* path conditions of a phase diagram. That is because the composition of the liquid phase changes over time during solidification. Micro-segregation inside phases is not anticipated with these typical equilibrium phase diagrams either. All these challenges can be partially addressed with classical thermodynamics by performing *Scheil-Gulliver Cooling* calculations [38]. They can provide a more realistic phase assemblage determination. Additionally, they can come up with suggestions about the micro-segregation inside phases. Still, these calculations are purely thermodynamic, so they do not provide information about solidification mechanisms and grain size of resulting alloys.

Since the early stages of nucleation consist of extremely small time and length scales, atomistic simulations are believed to be useful in providing intuitions about the fundamental aspects of solidification [5]. As such, this work aims to study the solidification of primary phases of different model Al-alloys by means of molecular dynamics (MD) and experiments. Aluminum alloys are classified into different series depending on their alloying elements. The main alloying components of these series are typically eutectic elements to aluminum (Cu for 2xxx series, Mg for 5xxx series, and Zn for 7xxx series); as such, they are added at relatively high amounts and are accepted into the primary α -FCC phase depending on their partition coefficient. Rejected eutectic elements from the α -Al phase to the liquid participate later on in the precipitation of secondary and/or ternary phases that define the mechanical properties of the resulting alloy. The α -Al phase is usually the desired primary phase for ingot casting. While eutectic elements do not inhibit the α -FCC formation as the first precipitate upon solidification, an excess in ppm (weight) of peritectic elements can lead to the formation of

intermetallics as primary precipitates. Some typical peritectic elements providing strength to Al are Cr, Zr and Ti [39–41]. Therefore, the Al-Cu, Al-Cr, and Al-Zr-Ti systems are relevant for aluminum alloy design.

One key ingredient in the numerical exploration of the energetic behavior of solid phases in MD is the selection of the adequate interatomic potential to describe the strength of the energetic interactions in the considered phase(s). Here, the transferability (i.e. ability to produce properties of characteristic phases) of interatomic potentials for Zr, Al-Cu, Al-Cr, and Al-Zr-Ti has been inspected. This is a fundamental procedure for potential validation and further exploration in higher-order systems. Primarily, it allows to evaluate the congruence of potential models to describe interatomic interactions in solids and liquids phases. Pure Zr was selected as the first case of study because it undergoes a phase transformation (i.e. an allotropic transition) at high temperature. The effect of selecting one of the two allotropes as a reference structure on the structural description of the liquid phase was evaluated. The parametrization of the Al-Cu interatomic potential described with the second nearest-neighbor Modified Embedded Atom Method (MEAM) formalism using three metastable reference structures was studied. The best model (out of these three force fields) was later compared to other interatomic potentials from literature. Specifically, one model from the MEAM formalism reported by Mahata et al. [42] and another force field based on the Angular-Dependent Potential (ADP) formalism from Apostol & Mishin [43]. These models were also compared to ab-initio molecular dynamics (AIMD) calculations of Wang et al. [44] for the structural description of Al₈₀Cu₂₀ melts. Solidification of pure Al has been investigated using the MEAM model and an force field from the Embedded Atom Method (EAM) using the Finnis and Sinclair (FS) approach to describe the Al-Al interatomic interactions. These simulations illustrate the inconsistency between classical pairwise models in describing pure elements. Indeed, the solidification of the primary Al-FCC phase is dependent on the formalism used in the parametrization. In recent literature, it has been reported that Cr promotes the icosahedral enhanced nucleation of the α -FCC phase in Al-Cr alloys [7]. For this reason, solidification of Al-Cr alloys has been performed using both the MEAM and FS models. Simulations results have shown that Cr promotes the formation of the Icosahedral Short-Range ordering (ISRO) in Al-Cr melts. This ordering appears to be favorable for the nucleation of the α -Al phase. Indeed, the more Cr was present in the system, the less undercooling was observed during the solidification of Al-Cr alloys. By tracking of the ISRO, it was also possible to identify the different steps of solidification, i.e. formation of nuclei, effective germination of the α -Al phase and end of solidification. However, precipitation of intermetallics at the hyperperitectic compositions was not achieved in Al-Cr alloys. This was associated with the high cooling rates used in classical MD of this work (-1 K/ps). On the

other hand, the Al-Zr-Ti interatomic potential was used to study the precipitation of Al_3Zr and Al_3Ti intermetallics due to their importance as nucleant particles for the α -FCC phase in Al-Zr-Ti-based alloys [45–48]. Unfortunately, these tasks were not accomplished, the FCC and HCP phases were rather the main phases found for these alloys. This implies that Zr and Ti supersaturated the stable FCC and metastable HCP phases due to the high cooling rates. Modeling of pseudobinary solid solutions based on these intermetallics was performed using MD and first-principles calculations to understand the energetic contribution of Zr/Ti sub-lattice substitution.

Because of the limitations encountered during the MD simulations, it has been decided to perform solidification experiments for one of the simulated systems. The system selected for this task was Al-Si-Zr-Ti. As in MD simulations, the experimental work was axed towards identifying $\text{Al}_3(\text{Zr},\text{Ti})$ -based intermetallics. Si was added to the initial Al-Zr-Ti system because it is a highly used alloying element in aluminium alloys [49]. Experimental solidification was performed in a set-up based on the Porous Disc Filtration Apparatus (PoDFA) technology. This mounting generates an environment close to thermodynamic equilibrium, ensuring optimal conditions to precipitate specific phases. Additionally, it allows to partially filter the equilibrated liquid so that the intermetallics of interest are concentrated in a modest FCC-matrix. This is essential because peritectic elements (i.e. Ti and Zr) are usually added in small amounts for industrial applications. In fact, the selected compositions for this work correspond to the precipitation of <10 g of intermetallics/kg of alloy, according to thermochemical simulations performed with FactSage [12]. Experimentally obtained intermetallics were characterized to investigate Al/Si sub-lattice substitution, their crystallography, and the partitioning of Zr and Ti within these phases.

1.1 Context

1.1.1 Aluminum alloys and V-lab project

The Virtual Laboratory for the aluminum industry (V-lab) was created as a collaboration of the Centre for Research in Computational Thermochemistry (CRCT) from Polytechnique Montréal and several primary aluminum and aluminum alloy industrial partners (i.e. Rio Tinto, Elysis, Alcoa, Hydro-Aluminium and Constellium). This alliance aims to generate accurate databases for the thermodynamic modeling of the primary aluminum production as well for the fundamental understanding, from a thermodynamic perspective, of aluminum alloy production (including their synthesis in the molten state, their casting and their heat treatment) and recycling. Traditionally, optimization of databases is performed according to

the CALPHAD approach, which relies on the availability of experimental data [50]. Progress and development of supercomputers have opened up a fresh opportunity for using atomic-scale tools to improve the thermodynamic modeling of Al-alloys (Figure 1.1). AIMD with Density Functional Theory (DFT) and classical MD simulations are two popular computational tools for describing metallic systems. This master's dissertation had the main purpose of studying the solidification of aluminum alloys using MD, as well as its capability for identifying primary phases upon (extremely) fast solidification. One of our industrial partners, i.e. Constellium, has directly contributed to this project by hosting my internship so I could perform some key experiments for this work.

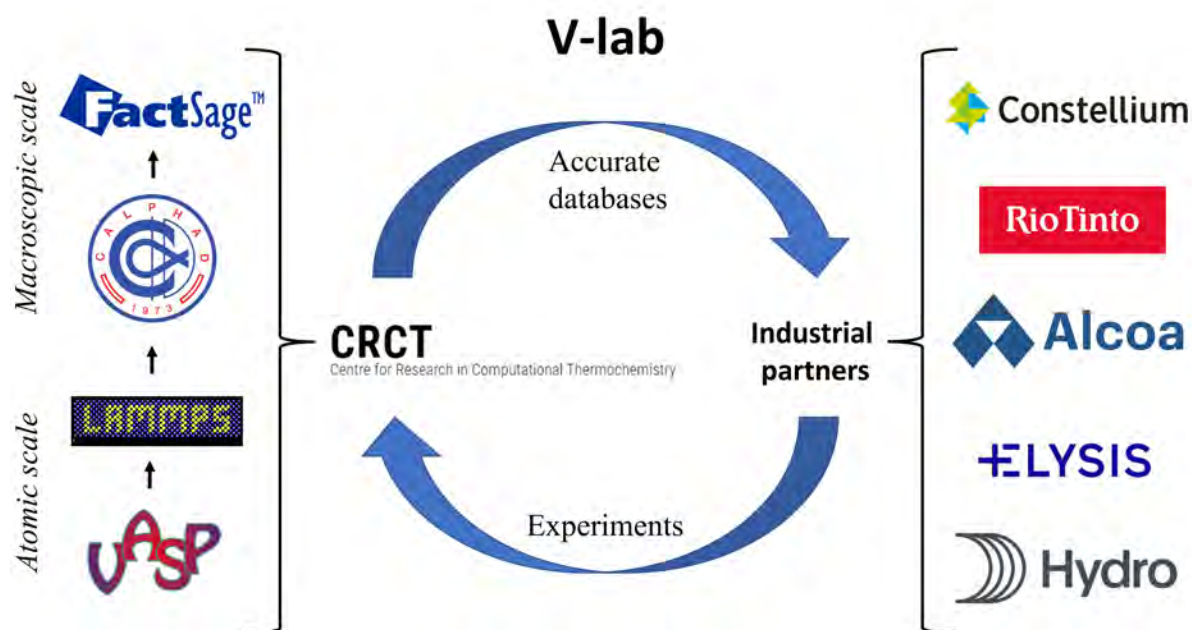


Figure 1.1 Diagram showing the main computational tools available at CRCT (left side) in order to optimize thermodynamic databases for the industrial partners (right side) within the V-lab collaboration.

1.1.2 Availability of supercomputers

The Digital Research Alliance of Canada is an organization providing a national advanced research computing platform. It includes a conglomeration of cutting-edge technology clusters across Canada. CRCT is granted computational resources every year for research in metallurgy. More specifically the Large-scale Atomic/Molecular Massively Parallel Simulator (LAMMPS) [51] and the Vienna Ab initio Simulation Package (VASP) [52] software have been used by the highly trained personal (HQP) of the V-Lab project to gain fundamental

energetic insights about many distinct condensed phases (such as intermetallics, molten salts, oxides and more).

1.2 History of the project

This project was originally oriented toward the understanding of nucleation mechanisms in aluminum alloys using MD simulations. Initially, interatomic potential models were directly taken from the open literature. However, the transferability of these reported potentials was questionable when one aimed to simultaneously model solid and liquid phases with a high accuracy. For example, by using an EAM model based on the Finnis-Sinclair (FS) approach for the Fe-Al-Cr interatomic potential [20], it was found that the strength of the Al-Cr energetic interaction was significantly overestimated (meaning that the Al-Cr interaction was too energetically stable leading to large and negative enthalpy of mixing when compared to pure Al and pure Cr). While the authors of this model reported good modeling for specific FeCrAl ferrite alloys [20], this inter-atomic potential was not transferable for solid and liquid systems within the binary Al-Cr system. This was a motivation to build a database containing reliable interatomic potentials. The produced database was constructed according to the MEAM (or 2NN-MEAM) formalism [53]. MEAM-based potentials are some of the most robust models to describe metallic systems nowadays. Parametrization of MEAM potentials is particularly convenient as it only requires a few sets of physical-related parameters. Parametrized Al-Cr and Al-Zr-Ti models were later used to study solidification. More specifically, these potentials were used to understand the icosahedral enhanced nucleation of the α -Al phase in Al-Cr alloys and to predict the formation of key intermetallics within the Al-Zr-Ti system, i.e. the Al_3Ti and Al_3Zr phases. Additionally, the Al-Cu system was also parametrized and validated because of its importance in the 2xxx aluminum alloys. The performance of this model was evaluated for $\text{Al}_{80}\text{Cu}_{20}$ melts and compared to two other interatomic potentials reported in the literature. Modeling of liquid Zr using two allotropes was also carried out to highlight the reference dependence even for unary interatomic interactions. Finally, in situ precipitation of Al_3Zr and Al_3Ti intermetallics were achieved during the solidification of Al-Si-Zr-Ti aluminum alloys during the internship at Constellium. Characterization of these phases offers a starting point for the refinement of thermodynamic databases through the V-lab project.

CHAPTER 2 LITERATURE REVIEW

2.1 Aluminium alloys

Aluminum is the second most abundant metallic element in the earth crust [54]. Aluminum alloys are the most widely employed nonferrous alloys due to their corrosion resistance, high strength, and lightweight [55, 56]. Corrosion resistance of aluminum is due to its affinity to oxygen, which allows to form a thin protective oxide layer as soon as it is exposed to the atmosphere [57]. For aluminum alloys, additional passivation treatment is required when the natural oxide layer is not efficient. Some of the passivation treatments are: chromate conversion coating [58], and anodizing [59]. Aluminum alloys are not usually used for high-temperature purposes because of their relatively low melting point ($\sim 660^\circ\text{C}$). Instead, they are preferred for low-weight applications, such as in the automobile, aerospace, and technology industries [60]. For structural parts, aluminum alloys present several advantages compared to other materials. For example, aluminum is easier to extrude than steel. This allows to obtain parts with one simple extruded section rather than the more complex technologies required for steel molding, which usually involves welding steps [61]. Aluminum is also interesting because of its important recyclability [62]. Aluminum recycling can result in reductions in energy requirements up to 95% for its production [54].

Wrought aluminium alloys are categorized into nine series using a four-digit system implemented by the Aluminum Association Inc. The first digit (Xxxx) denotes the principal alloying element, the second one (xXxx) indicates the modification of the specific alloy, and the last two numbers (xxXX) are arbitrary numbers to distinguish a particular alloy within the series [56]. On the other hand, cast alloys follow a 3-digit-plus decimal designation (xxx.x), the first digit being the main alloying element, the second and third indicate a specific alloy, and the number after the decimal point (.x) denotes if the alloy is a casting (.0) or an ingot (.1 and .2) [63]. Some of these series are briefly described according to the selected alloying elements for this study, i.e. Cu, Si, Ti, Zr and Cr. Cu and Si are eutectic elements to aluminium (see Figures A.1 and A.2), while Ti, Zr and Cr are peritectics (see Figures A.3, A.4 and A.5). Although phase diagrams of real alloys are more complex than the binary phase diagrams presented in Appendix A, it can be observed that Cu and Si have a significant solubility within the α -Al phase, and allow the precipitation of primary α -Al phase at relatively high amounts of solute (or main alloying element) due to their eutectic nature. Contrastingly, the formation of the α -Al phase as a primary precipitate is highly compromised by small amounts of peritectic elements (Ti, Zr, and Cr). Along with the vi-

tal α -Al phase, the presence of secondary/ternary phases is responsible for the mechanical properties of the different aluminum alloys. Some important phases related to the elements considered in this work are mentioned in the following subsections.

2.1.1 Cu in 2xxx and 2xx.x series

Cu is the main alloying element for the 2xxx and 2xx.x series of aluminum alloys. They are heat treatable and widely employed in the automotive and aviation industries [64,65]. Their mechanical properties are enhanced through age hardening. This allows to precipitate ordered phases that provide strength to the alloys [66]. The Cu content in Al-Cu alloys is 2-10 %, along with minor additions of other elements [67]. According to the Al-Cu phase diagram (Figure A.1), this range of compositions leads to the precipitation of the α -Al phase as a primary phase. The Al_2Cu phase is a secondary phase resulting from the eutectic reaction. Additional alloying elements participate in the formation of secondary and further phases. Globally, some of the most important phases for Al-Cu alloys are: Al_2Cu ($I4/mcm$) [68], $\text{Al}_7\text{Cu}_2\text{Fe}$ ($P4/mnc$) [69], $\text{Al}_6\text{Cu}_2\text{Fe}$ ($Fm\bar{3}5$) [70, 71], $\text{Al}_{10}\text{Cu}_{10}\text{Fe}$ ($P\bar{3}m1$) [72], Al_2CuMg ($Cmcm$) [73], Al_2CuLi ($P6/mmm$) [74, 75], Al_3Li ($Pm\bar{3}m$) [75], and $\text{Al}_{20}\text{Cu}_2\text{Mn}_3$ ($Bbmm$) [76].

2.1.2 Si in 4xxx, 6xxx, 4xx.x, 3xx.x and series

The principal alloying element of the 4xxx series is Si. They also contain limited amounts of Fe that promotes the formation of secondary phases [77]. Even though Mg is the main alloying element in the 6xxx series, Si is usually present in these alloys to promote the formation of Mg-Si phases [78, 79]. For cast alloys, Si is not only a principal alloying element for the 4xx.x, but also for the 3xx.x series. However, Si is combined with copper and/or magnesium in the 3xx.x series [80]. According to the Al-Si phase diagram (Figure A.2), Si can be accepted in high amounts of an alloy without jeopardizing the primary precipitation of the α -FCC phase (Figure A.2). Nonetheless, Si is sometimes added at higher concentrations than its solubility limit in order to precipitate eutectic Si and primary Si. In that case, they are respectively called eutectic [81] and hyper-eutectic alloys [82]. Important phases for Al-Si alloys include: α -AlFeSi ($P6_3/mmc$) [83, 84], β -AlFeSi ($C2/C$) [84], Al_3FeSi_2 ($I4/mcm$) [85], $\text{Al}_{13}\text{Si}_4\text{Cr}_4$ ($F\bar{4}3m$) [86], Mg_2Si ($Fm\bar{3}m$) [87], and π -AlFeMgSi ($P\bar{6}2m$) [88].

2.1.3 Ti and Zr in aluminium alloys

Ti and Zr are used in aluminium alloys to control the as-cast grain size and to prevent recrystallisation [89, 90]. The presence of Ti is highly important for grain refinement mechanisms, which are assisted through the Al_3Ti ($I4/mmm$) phase [91]. Grain size in aluminium alloys is controlled through TiB_2 particle from Al-Ti-B master alloys, and with TiC particles from Al-Ti-C master alloys [92]. Nonetheless, the effectiveness of both TiB_2 and TiC refiner particles is broadly dependent on the Ti content in aluminum melts. This is because an Al_3Ti layer is needed at the interface of the refiner particles before they act as nucleation sites for the α -Al phase [46, 93–96]. Zr in aluminum alloys can form the tetragonal stable Al_3Zr ($I4/mmm$) phase, or the cubic metastable Al_3Zr ($Pm\bar{3}m$) phase [97]. The latter being promoted at high cooling rates and believed to act as nuclei for the α -Al phase during lasing [98]. Recent studies have shown that Al_3Zr primary intermetallic can also act as heterogeneous nucleation sites for the Al-FCC phase [47, 99, 100].

2.1.4 Cr in aluminum alloys

Al-Mg, Al-Mg-Si, and Al-Mg-Zn alloys usually contain Cr as alloying element. It is added at a limited concentration of 0.035 wt% or less in order to avoid the formation of coarse intermetallic phases. It is included into Al-Mg alloys to restrain grain-growth, and into Al-Mg-Zn and Al-Mg-Si alloys to prevent recrystallization [67]. New studies have shown that Cr can participate in grain refinement mechanisms in Al-alloys. Specifically, Kurtuldu et al. [7] found that minor additions of Cr (in ppm) can lead to the formation of a refined microstructure of 7xxx-like alloys.

2.2 Theory of solidification

2.2.1 Nucleation

Nuclei (sometimes referred to as nucleus or cluster) is a small ensemble of atoms of a new solid daughter phase coexisting with its parent liquid phase. Nucleation is therefore the abrupt formation of nuclei in a first-order transition (liquid to solid) [101, 102]. Control of nucleation is crucial during alloy engineering in order to manage grain size and growth [103]. There exist several theories regarding homogeneous and heterogeneous nucleation. The former implies that the atoms which form the melt can spontaneously arrange themselves into a lattice structure without any preference over the whole melt [104], the latter suggests that impurities or external substances/materials to the melt act locally as the nuclei [105].

2.2.2 Classical Nucleation Theory (CNT)

The Classical Nucleation Theory (CNT) establishes that portions (clusters) of the crystalline phase are separated from the liquid phase by vanishing thin interphase. This hypothesis is called the capillarity approximation. In spite of the small size of the clusters, they are treated as macroscopic objects (i.e. as if they have the same properties as the bulk material) in order to adjust the theory with Continuum Thermodynamics. This approximation could be reasonable for large clusters, but for small clusters, it results in inconsistencies due to the curvature on the surface [106]. From the assumptions of the capillarity approximation for homogeneous nucleation, a mathematical expression (2.1) of the free energy of formation for spherical crystalline nuclei of radius r , ΔG_N , as a function of the interfacial energy, γ_S , and the free energy difference between the crystal and the liquid, μ_V , was reported [5].

$$\Delta G_N = 4\pi r^2 \gamma_S - \frac{4\pi}{3} r^3 \Delta \mu_V \quad (2.1)$$

Figure 2.1 illustrates different scenarios for the free energy difference, ΔG_N (Equation 2.1), according to Gabriele et al. [5]. The free energy of formation presents a maximum, ΔG_N^* , that corresponds with the critical nucleus size, n^* (Figure 2.1) [5]. That is the number of atoms needed in a cluster to overcome the energy barrier to form a stable nucleus within the undercooled liquid. As shown in Figure 2.1, a lower free energy barrier appears for heterogeneous nucleation compared to the homogeneous one. At last, for spinodal decomposition, the mechanism is carried out in a barrierless way because the undercooled liquid is less stable than the crystalline phase [5].

Heterogeneous nucleation is more likely to occur since the presence of foreign substances lowers the energy barrier. This mechanism is actually the most common to occur in liquids. The modelling of heterogeneous nucleation with CNT takes into account geometric arguments and some approximate models can be obtained. However, impurities, in reality, are not necessarily spherical-shaped, and many morphologies can exist for the same impurity, so the modeling becomes more complicated [5].

2.2.3 Two-Step Nucleation Theory

The two-step nucleation theory establishes: (1) the formation of a dense liquid cluster, and after that, (2) the formation of a crystal nucleus inside the dense liquid cluster [6]. Then, there are two energy barriers corresponding to those steps that need to be overcome (Fig. 2.2). On the other hand, for the CNT, only a single energy barrier corresponding to the critical nucleus size has to be climbed. The two-step nucleation theory has been accepted to

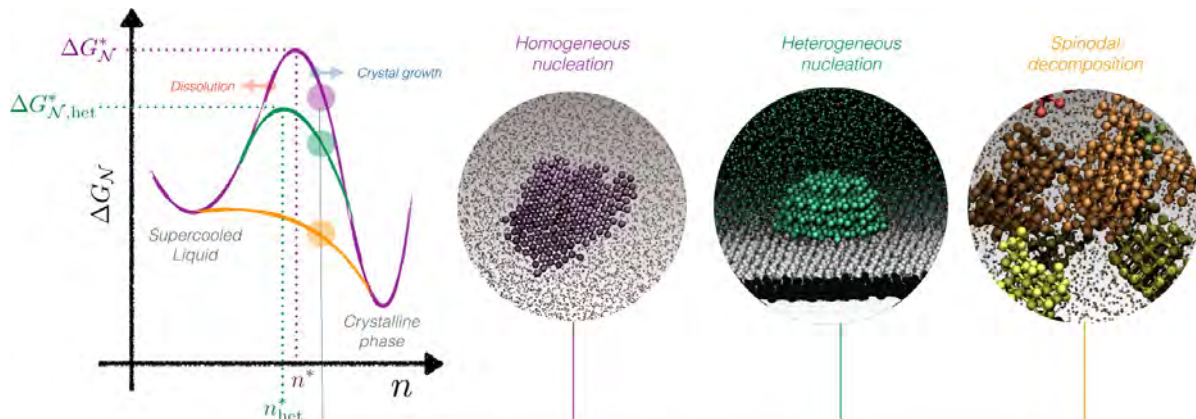


Figure 2.1 Sketch of the free energy of formation of a nucleus, as a function of the crystalline nucleus size for homogeneous nucleation (purple), heterogeneous nucleation (green), and spinodal decomposition (orange) showing the maximum of energy to overcome to promote the formation of the nuclei. Taken from [5].

describe several applications for crystal nucleation, such as in colloids, Lennard-Jones liquids, urea, NaCl, as well as in biomineralization and proteins [5].

2.3 Grain refiner theories in Al-alloys

Grain refinement is desirable in alloy engineering to promote the formation of a fine and equiaxed grain structure, which is useful to reduce casting defects [107]. Grain refinement can be achieved by using nucleant particles or by specific processing conditions [108]. Generally speaking, grain refinement methods are divided into: *chemical refining* (by adding inoculant substances to the alloy) and *physical refining* (by applying external forces to the melt) [109]. Guan & Tie [93] proposed a classification for current processing techniques, it includes four categories: the addition of grain refiner, rapid solidification, severe plastic deformation, and finally, grain refining by vibration and stirring during solidification. Only the categories related to the scope of this work are briefly described in further sections, i.e. by grain refiner, by rapid solidification and the recently published theory on the icosahedral-enhanced nucleation of the Al-FCC phase promoted by Cr [7].

2.3.1 Grain refinement by Grain Refiner (GR)

Grain refining theories by grain refiners share the same notion. That is, grain size depends on the nucleation and growth of the α -Al phase induced by nucleant agents. The addition of a grain refiner into aluminum alloy melts is believed to generate vast heterogeneous nucleation

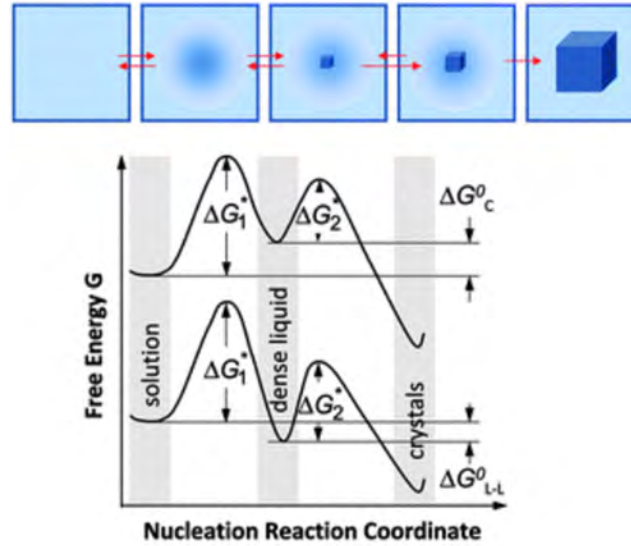


Figure 2.2 Sketch of two-step nucleation theory and its free energy barriers to overcome.
Taken from [6].

sites of the α -phase. The external elements can also induce constitutional supercooling, which has been reported to accelerate heterogeneous nucleation. Finally, the external insoluble particles or solution elements can restrict the growth grain by segregation [93]. Some of the most popular theories for the heterogeneous nucleation by grain refiners are listed here below:

- **The peritectic theory :** It states that grain refinement by adding a refiner comes from the peritectic reaction of the Al-rich side of the Al-Ti phase diagram, it was suggested by Crossley & Mondolfo [45]. It can be summarized as follows [93]:



- **The carbide-borides theory :** Cibula [110] suggested that carbide (Expression 2.3) or boride (Expression 2.4) particles can promote the nucleation of the α -Al during the solidification of aluminum alloys [93,110]. However, neither the borides nor the carbides particles are effective as grain refiners without solute Ti in the melts [93].



- **The duplex theory :** This theory states that an Al_3Ti layer is formed around the TiB_2 grain refiners and remains stable when the grain refiner is added to a hypo-peritectic alloy, consequently acting as a nucleation site for the α -Al phase [94]. Schumacher experimentally found that a layer of Al_3Ti coating the basal plane of a TiB_2 particle [111]. The authors explained that the non-equilibrium Al_3Ti layer is stabilized through the chemical interactions between Al_3Ti with the TiB_2 substrate. Wang et al. [112] also found that Al_3Ti grows at the surface of TiB_2 particles in an Al-Ti-B master alloy. On the other hand, Cui et al. studied the orientation relationships between Al_3Ti and TiB_2 upon solidification of hyperperitectic Al-rich melts [113], they found three main favorable crystallographic relationships for these phases to aggregate: $\{112\}_{\text{Al}_3\text{Ti}} \parallel \{0001\}_{\text{TiB}_2}$, $\{001\}_{\text{Al}_3\text{Ti}} \parallel \{0001\}_{\text{TiB}_2}$ and $\{100\}_{\text{Al}_3\text{Ti}} \parallel \{0001\}_{\text{TiB}_2}$. This theory explains the role of Ti to form an Al_3Ti layer, which was not specified in the initial carbide-borides theory [93].



- **The solute theory :** The solute theory states that a solute element causes constitutional supercooling which promotes heterogeneous nucleation. Also, it affirms that grain growth is restricted by the segregation of the alloying element close to the solid-liquid interface [93]. Wang et al. [114] studied three important eutectic-forming solutes in aluminium alloys, i.e. Mg, Si, and Cu. They reported that these elements slightly contribute to grain refinement mechanisms due to their segregation power.

2.3.2 Icosahedral quasicrystal-enhanced nucleation of the fcc phase

Grain refinement by icosahedral quasicrystal-enhanced nucleation of the fcc phase has been suggested in Al-Zn-Cr alloys. Rappaz et Kurtuldu [7] reported the effect of adding 1000 ppm (by weight) of Cr into an Al-20 wt.%Zn alloy, proving that the alloy containing Cr presented smaller grains than the non-doped alloy (see Figure 2.3). Solidification assisted by icosahedral quasicrystals (iQC) was suggested as follows: 1. Formation of the iQC in the liquid alloy (Figure 2.4a), 2. Nucleation of the alpha-fcc on the iQC facets (Figure 2.4c) and 3. Growth of the fcc phase (Figure 2.4d).

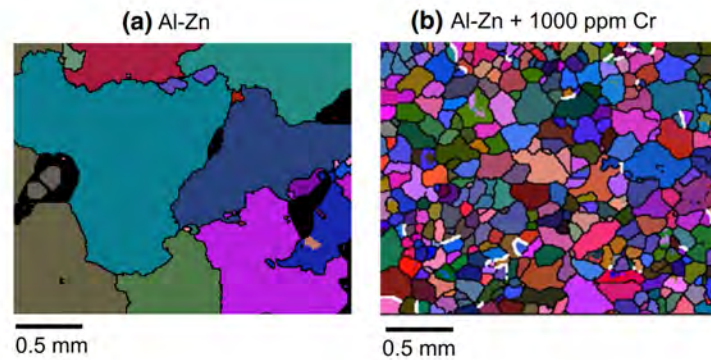


Figure 2.3 Electron Backscatter Diffraction (EBSD) analysis of Al-Zn-Cr alloys, with (b) and without (a) Cr. Different orientations of grains are represented with different colors. Adapted from [4].

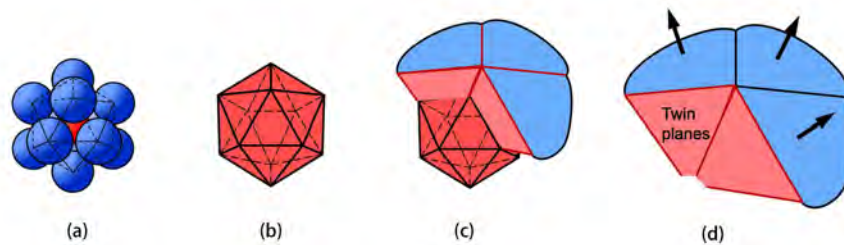


Figure 2.4 Representation of the iQC-mediated nucleation mechanism. Taken from [7].

2.3.3 Grain refinement by rapid Solidification (RS)

Refinement of grain size can be accomplished by rapid solidification processing, it is assisted whether by bulk melt undercooling or by heat extraction [115]. This is because nucleation rates are augmented by increasing the cooling rates. Cooling in regular large-scale casting processes occurs at less than 0.1K/s and between 1-1000 K/s in mold casting. Processing techniques involving cooling rates larger than 10^3 K/s are considered rapid solidification operations. Technologies reaching cooling rates of 10^2 - 10^3 K/s are water quenching, copper mold casting, twin-roll casting, high-pressure casting, and cooling slope. In melt spinning, cooling rates as high as 10^3 K/s can be reached. Gas atomization can range from 10^2 - 10^4 K/s. The fastest cooling rates are achieved by spray deposition, reaching 10^3 - 10^5 K/s [93]. Rapid solidification is believed to be affected by solute trapping and/or by the formation of metastable phases. Solute trapping refers to the incomplete solute partitioning at the solid-liquid interface due to the high cooling rates, which affects the morphology of phases [116]. Rapid solidification is also related to the formation of metastable phases. These intermetallics

can act as nucleation sites of the Al-FCC, which is the case of the $\text{Al}_3\text{Zr-L1}_2$ in Al-alloys. High cooling rates also promote the formation of metastable quasicrystals with icosahedral ordering [98].

2.4 State-of-the-art of MD in real alloys

2.4.1 Homogeneous nucleation

Large-scale molecular dynamics simulations have become of interest to studying solidification in metals. Hou et al. (2016) [117] studied the effect of the cooling rates between 0.1 and 10 K/ps in pure aluminum. They worked with simulation boxes of 1 048 576 atoms and used an embedded atoms method (EAM) potential [118] to describe the Al-Al interactions. They reported the formation of metallic glasses with short-range icosahedral ordering when using 10 K/ps (the fastest cooling rate). For slower cooling rates (≤ 4 K/ps), their simulation cells solidified into the FCC and HCP phases. Crystallization of the metastable HCP phase was associated with twinning. Zhang et al. (2019) [119] used cubic simulation boxes of 3 456 000 atoms to study the rapid solidification in pure iron melts. They used the embedded atoms method (EAM) potential [120] to describe the iron interatomic interactions and used cooling rates between 0.095 K/ps and 9.5 K/ps. They concluded that the icosahedral ordering was promoted in undercooled melts by increasing the cooling rate. They reported a critical cooling value of 4 K/ps for glass transition. i.e., above this value, the icosahedral-like configurations were dominant and led to the formation of amorphous structures. Below the critical value, crystalline structures were obtained. Papanikolaou et al. [121] reported equivalent conclusions during their study of pure aluminum using a Finnis-Sinclair (FS) potential and five different cooling rates ranging from 0.5 to 12 K/ps. They noted that the amorphous phase is favored by rapid solidification while the FCC and HCP are the main phases at low cooling rates. Zang et al. (2021) [10] studied the homogeneous nucleation of the Al-4 at.%Cu alloy using an EAM potential. They obtained nanocrystals made up of FCC and HCP phases.

2.4.2 Heterogeneous nucleation

Heterogeneous nucleation has recently been achieved with classical molecular dynamics by Sun et al. (2018) [122]. They artificially seeded a liquid with solid embryos and by applying external forces that prevent them from melting. Fujinaga et al (2020) [123] successfully accomplished the germination of the α -FCC phase by imposing $\text{Al}_3\text{Ti-D0}_{22}$ and $\text{Al}_3\text{Ti-L1}_2$ interfaces with liquid aluminum. Still, these methodologies can not be used for the prediction of primary phases because the user should know in advance the nature of the imposed

embryos.

2.4.3 Effect of Cr on the icosahedral-enhanced nucleation of the fcc phase

One principal motivation of this work was to explore the effect of Cr on the solidification of the fcc phase in Al-Cr alloys using large-scale MD simulations. This has not been reported yet in literature to the best of our knowledge. An explanation of this theory has only been addressed by Pasturel and Jakse [124] by describing the structural properties of liquid $\text{Al}_{90}\text{Zn}_{10}$ and $\text{Al}_{83}\text{Zn}_{19}\text{Cr}_7$ alloys. They used *ab initio* MD (or AIMD) with simulation boxes of 256 atoms. They reported that the presence of Cr promotes the formation of icosahedral short-range order. Although they did not solidify the alloys, they suggest that the structural heterogeneities caused by Cr may explain its role in the quasicrystal-based nucleation mechanisms [98, 124]. The simulation cells used by Pasturel and Jakse [124] for AIMD calculations are small because of their high computational cost compared to classical MD.

CHAPTER 3 GAP OF KNOWLEDGE AND OBJECTIVES

Applications of Molecular Dynamics (MD) to metallic systems continues to grow due to the accelerated development in computer science. The purpose of this master's thesis is to apply MD simulations to the prediction of primary phases in aluminum alloys. This includes the construction of interatomic potentials, description of solutions, and solidification simulations. Experiments were also included for specific and equivalent systems used in MD simulations. This was a crucial step to validate atomistic simulations and to identify their limitations. Results are separated into a submitted manuscript (Chapter 5) and a classical chapter (Chapter 6).

3.1 General objective

To identify primary phases during the solidification of Al-based alloys using MD simulations and experimental work.

3.2 Specific objectives

- **O1:** Develop force field models for the systems: Zr, Al-Cu, Al-Cr, and Al-Si-Ti-Z based on the second nearest-neighbor modified embedded-atom (MEAM) method (Chapter 5).
- **O2:** Investigate the impact of the reference allotrope for unary Zr interactions, as well as the effect of reference metastable compounds for the binary Al-Cu system using classical force field models (Chapter 5).
- **O3:** Validate the performance of developed inter-atomic potentials on the description of solutions (Chapter 5).
- **O4:** Perform mesoscale simulations for the solidification of pure Al, Al-Cr, and Al-Si-Ti-Z alloys at the mesoscale using molecular dynamics (Chapter 5)
- **O5:** Examine the influence of Cr in Al-Cr alloys and its impact on the icosahedral ordering and the nucleation of the α -Al phase (Chapter 5).
- **O6:** Identify primary phases within Al-Zr-Ti alloys using large-scale simulations of solidification (Chapter 5).

- **O7:** Identification of primary phases within Al-Si-Zr-Ti alloys using innovative setup based on the Porous Disc Filtration Apparatus (PoDFA) technology (Chapter 6).
- **O8:** Determine the Si sublattice substitution in Al_3Ti and Al_3Zr intermetallics via EDX analysis, and the viability of these intermetallics as nucleant particles of the α -phase through TEM analysis (Chapter 6).

CHAPTER 4 METHODOLOGY

4.1 Classical Molecular Dynamic (MD) simulations

Currently, there exist several computational methods to study the coexistence of liquid and solid phases in a system, however, most are limited to smaller scales compared to molecular dynamic simulations (MD) or are less predictive [125]. The interatomic potential is the basic ingredient to describe the energy properties of the system in MD simulations [126]. It allows the evaluation of the internal potential energy from a universal function that depends on the distance between atoms constituting the considered system. The atomistic simulations in this project were performed with the LAMMPS software [51] using periodic boundary conditions. Temperature and pressure were controlled by a Nose-Hoover thermostat and barostat [127–130]. Newton’s equation of motion was solved by means of the velocity-Verlet method [131] using a time step of 1 fs. Simulations were carried out in the NVT and NTP ensembles and were specified in each of the applications reported in Chapter 5. All the coolings were performed at 1 K/ps in the NTP ensemble. An example of the thermal program for the solidification of an Al-Cr alloy is presented in Appendix B, which describes the different parts of the input script for the simulations in LAMMPS. Structural analysis was performed with the Radial Distribution Function (RDF) [132] and also by post-treatment of the simulated position files using the OVITO software [133], with the Common Neighbor Analysis (CNA) [134] and the Polyhedral Template Matching (PTM) reported by Larsen et al. [8].

4.1.1 Equations of motion

Classical Molecular Dynamics simulations rely on Newton’s second law to compute the motion of atoms. Considering a system of N particles with the coordinates \mathbf{r}_i and a mass m_i , $i=1, \dots, N$, the following second order differential equation of motion is obtained:

$$\mathbf{F}_i = m_i \mathbf{a}_i = m_i \frac{d^2 \mathbf{r}_i}{dt^2} \quad (4.1)$$

Where \mathbf{F}_i is the force acting on particle i and \mathbf{a}_i is the acceleration. In LAMMPS, equations of motion (4.1) are solved by means of the velocity-Verlet method [131], which is an enhancement of the original Verlet algorithm [135]. This is a finite difference approach and it is derived from a truncated Taylor expansion. The velocity-Verlet algorithm provides the velocities \mathbf{v}_i

just after the new positions (\mathbf{r}_i) are computed [131], and the force, \mathbf{F}_i , was obtained with a force field model.

$$\mathbf{r}_i(t + \Delta t) = \mathbf{r}_i(t) + \mathbf{v}_i(t)\Delta t + \frac{1}{2}\mathbf{a}_i(t)\Delta t^2 \quad (4.2)$$

$$\mathbf{v}_i(t + \Delta t) = \mathbf{v}_i(t) + \frac{\Delta t}{2m_i}[\mathbf{F}_i(t) + \mathbf{F}_i(t + \Delta t)] \quad (4.3)$$

4.1.2 Force field models

In MD, the total force acting on atom i is the sum of all the i - j interactions :

$$\mathbf{F}_i = \sum_{i \neq j} F_{ij} \quad (4.4)$$

Computational costs are reduced thanks to the Newton's Third Law :

$$F_{ji} = -F_{ij} \quad (4.5)$$

Interatomic interactions of i and j atoms are computed from classical force field models. There exist several formalisms to tune the potential energy with pairwise models. For metallic systems, the Modified Embedded-Atom Method (MEAM) formalism is the of the most robust models. As such, it was used to tune the Zr, Al-Cu, Al-Cr, and Al-Ti-Zr systems of this work. A detailed description of the MEAM potential is provided in Chapter 5 of this work. The performance of models of this work is compared to other interatomic potential formalisms, such as the Embedded Atom Method of Finnis and Sinclair (EAM.FS) for the Al-Al and Al-Cr interactions [20]. Al-Cu interactions were compared to the Angular Dependent Potential (ADP) [43].

4.1.3 Size of simulation cells and its effect on solidification

While the MEAM database for aluminum alloys was being developed, preliminary MD calculations were performed with the EAM.FS model for Cu-Zr reported by Borovikov et al. [136]. Simulations of melting and solidification were executed only for pure Cu. Just as for Al, Cu has an FCC equilibrium structure under standard conditions (i.e. at 25°C and 1 atm). These simulations aimed to observe the effect of the size cell on the solidification of Cu. Initial cubic configurations were created based on FCC-unitary cells of: 10^3 , 20^3 , 30^3 , 40^3 , 50^3 and 60^3

unitary cells, which correspond to 4 000, 32 000, 108 000, 256 000, 500 000 and 864 000 atoms, respectively (Figure 4.1). Simulations were performed using periodic boundary conditions and a timestep of 10 fs. They followed the next stages: 1. 10 000 steps of equilibration at 2 K in the NVT ensemble, 2. NPT heating at 1.665 K/ps, 3. 50 000 steps of equilibration at 2 000 K in the NVT ensemble, 4. 50 000 steps of equilibration at 2 000 K in the NPT, 5. NPT cooling at 1 K/ps up to 300 K and 6. NPT equilibration at 300 K during 200 000 steps. The last configuration of all simulations is presented in the 3th column of Figure 4.1. It can be observed that, for the smaller box, only a few atoms had an FCC orientation (green atoms). It means that recrystallization of the FCC phase was not achieved for this simulation size. Instead, a metallic glass was obtained. From the simulation cell containing 32 000 atoms, small FCC grains were obtained.

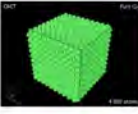
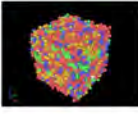
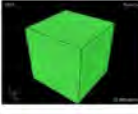
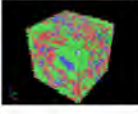

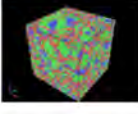

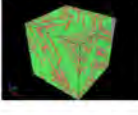

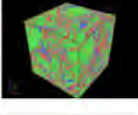

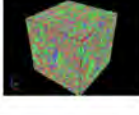
Size	Initial configuration	Final configuration
4 000 atoms (10 ³ unitary cells)		
32 000 atoms (20 ³ unitary cells)		
108 000 atoms (30 ³ unitary cells)		
256 000 atoms (40 ³ unitary cells)		
500 000 atoms (50 ³ unitary cells)		
864 000 atoms (60 ³ unitary cells)		

Figure 4.1 Initial and final configurations of melting and re-solidification simulations of pure Cu starting with a perfectly ordered FCC structure. Local ordering was evaluated with the Polyhedral Template Matching (PTM) reported by Larsen et al. [8]. Orientation of atoms is displayed by colors: green (FCC), red (HCP), blue (BCC), yellow (icosahedral), purple (Simple cubic) and gray (other).

Knowing that at least 32 000 atoms are required to obtain crystalline structures upon solidification and inspired by the quasi-two-dimensional cells proposed by Shibuta et al. [9] (Figure 4.2a), and by Zhan et al. [10] (Figure 4.2b). It was decided that solidification simulations for Chapter 5 would be performed with 200 000 atoms, corresponding to initial $100 a_0 \times 100 a_0 \times 5 a_0$ cells, where " a_0 " is the length of an unitary Al-FCC cell.

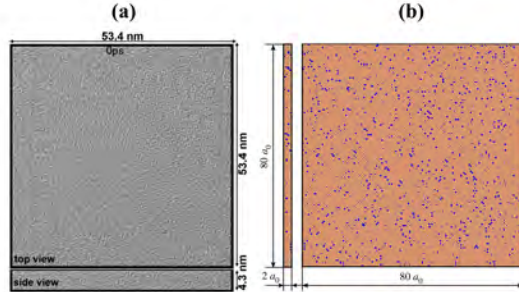


Figure 4.2 Representation of the quasi-two-dimensional cells proposed by (a) Shibuta et al. [9] during their study on the homogeneous solidification of iron, and by (b) Zhan et al. [10] for the solidification on an Al-Cu alloy. " a_0 " in (b) stands for the lattice constant of Al-FCC.

The tracking of temperature over simulation time for the simulations of pure Cu is presented in Figure 4.3a. Important deviations in temperature for the equilibration stage at 2000 K were observed. Islam et al. [137] reported that exploding (i.e. overlapping of atoms creating a strong repulsive force) occurs when large time steps are used in MD simulations and lead to a rapid increase in the total energy [137]. Therefore, the deviations at 2000 K are associated with the relatively high time step used for these simulations (10 fs). This problem was solved in further MD simulations (Chapter 5) by decreasing the simulation timestep from 10 fs to 1 fs. The literature on this subject shows that a timestep of 1 fs guarantees stable dynamics during a simulation [138, 139]. Indeed, MD solidification studies in metallic systems usually employ timesteps of 1 fs and 2 fs [10, 117, 119, 121–123].

The evolution of the FCC local ordering for pure Cu from our MD simulations was evaluated using the Polyhedral Template Matching (PTM) reported by Larsen et al. [8] (Figure 4.3b). Simulations with $\geq 32\ 000$ unitary cells were able to partially recrystallize into the FCC arrangement. FCC ordering at the end of the MD simulation (6ns) with 4 000 atoms had equivalent FCC ordering to the one of the undercooled liquid after cooling (around 4ns). This implies that a metallic glass was obtained, in spite of the further relaxation at 300 K (from 4 ns to 6 ns). This small size box is therefore not suited for crystallization/solidification studies.

Icosahedral ordering was also quantified using the Polyhedral Template Matching (PTM) for the different simulations (Figure 4.3c). This ordering is increased during the cooling process. In fact, Frank [140] predicted this ordering as an explanation for the local arrangement of small groups of atoms that can minimize their energy in undercooled liquids. Except for the small simulation with 4 000 atoms, the icosahedral ordering drastically decreased by the end of the cooling process (< 4 ns). The decreasing icosahedral ordering is directly connected to the increase of the FCC phase in Figure 4.3b. Therefore, the solidification stages can be followed by tracking the icosahedral ordering upon cooling, i.e. the maximal value of this ordering (between 3-4 ns in Figure 4.3c) indicates the beginning of solidification, while the minimal value (around 4 ns) indicates the end of solidification. Indeed, only small amounts of molecules within crystallized simulations kept this ordering. Icosahedral ordering also confirmed that a metallic glass was obtained for the smaller simulation (4 000 atoms).

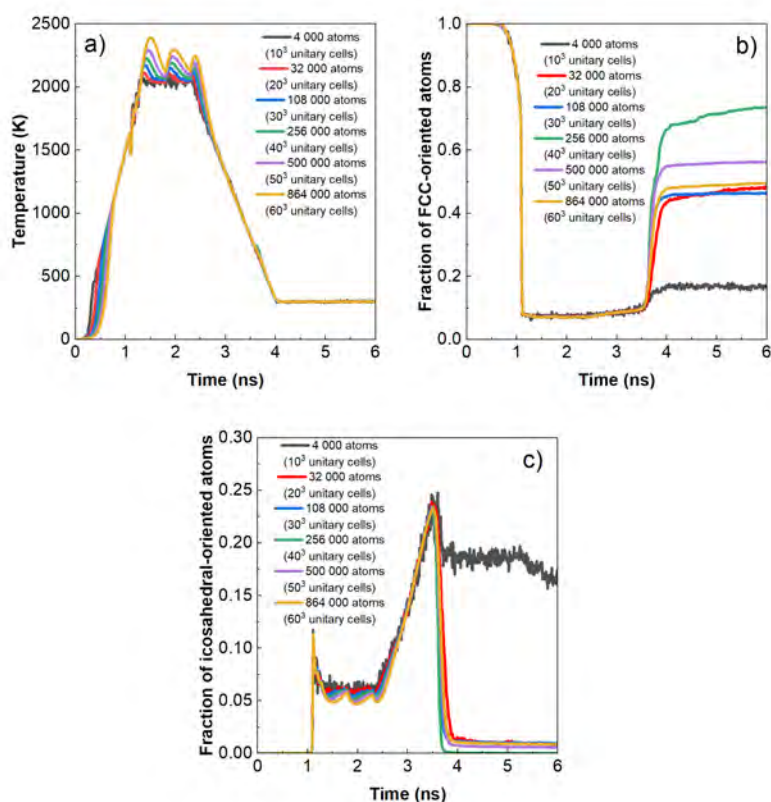


Figure 4.3 Evolution of temperature (a), the FCC-oriented local ordering fraction (b), and the icosahedral ordering (c), as a function of the simulation time (ns) for different simulation boxes exposed to the thermal program, which consisted of linear heating, isothermal holding and linear coolings.

4.2 Experimental work: Al-Si-Zr-Ti alloys

In the same manner as in MD simulations within the Al-Zr-Ti system, experimental work was performed in order to identify primary $\text{Al}_3(\text{Zr,Ti})$ -based intermetallic phases. The studied alloys also contain Si in order to investigate the possible substitution of Si within Al sublattices of the intermetallics. Synthesis was carried out in a setup based on the Porous Disc Filtration Apparatus (PoDFA) technology, which is useful to identify inclusions in alloys by filtering molten metals through a porous filter [141]. Samples were characterized and compared to classical thermodynamic simulations using the FTLite database of FactSage [12].

4.2.1 PoDFA setup

The PoDFA setup consists of a crucible adapted with a PoDFA filter (ABB Group). It is inserted in a heated chamber to control the temperature of a molten alloy (Figure 4.4a). The liquid is maintained at a target temperature for the precipitation of desired phases (Figure 4.4b). After that, pressure is increased to start filtration (Figure 4.4c). Finally, the heating source for the chamber is turned off and an α -matrix containing a high concentration of intermetallics is obtained at the bottom of the crucible (Figure 4.4d).

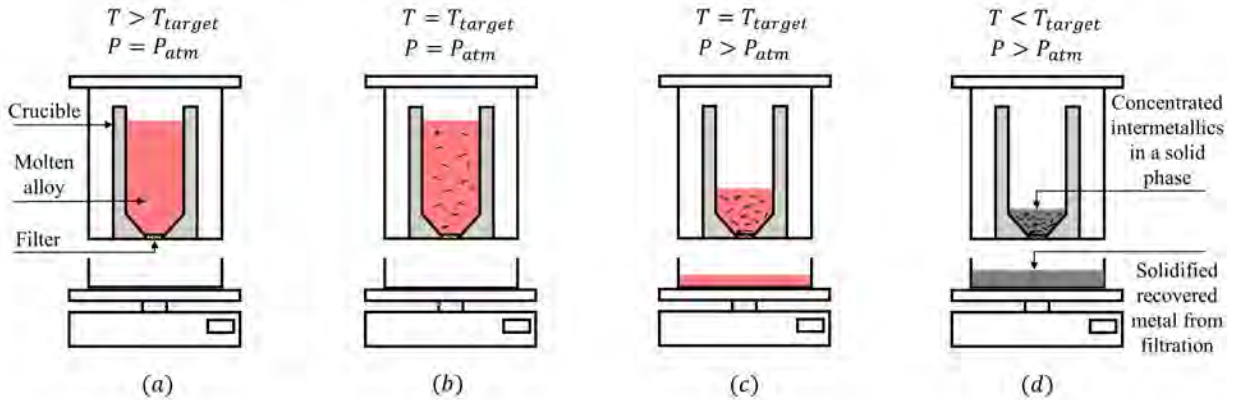


Figure 4.4 Diagram showing different steps during the synthesis of intermetallics in a PoDFA setup

4.2.2 Characterization

Obtained samples from the PoDFA setup were sectioned (Figure 4.5a and Figure 4.5b). Subsequently, they were chamfered (Figure 4.5c), cold mounted, and polished (Figure 4.5d). Polishing was carried out with water and sandpapers with granulation of P180, P600, P1200,

respectively, for 30 seconds each. This was followed by 6 min of polishing with a $6\mu\text{m}$ polishing pad, 6 min with a $3\mu\text{m}$ polishing pad, and 3 min with a $1\mu\text{m}$ polishing pad. The last three stages were assisted with Struers DiaPro diamond solutions. Micro-structure and chemical analysis was carried out by means of light microscopy, Electron Microprobe (EMP), and Energy-Dispersive X-ray Spectroscopy (EDS) analysis.

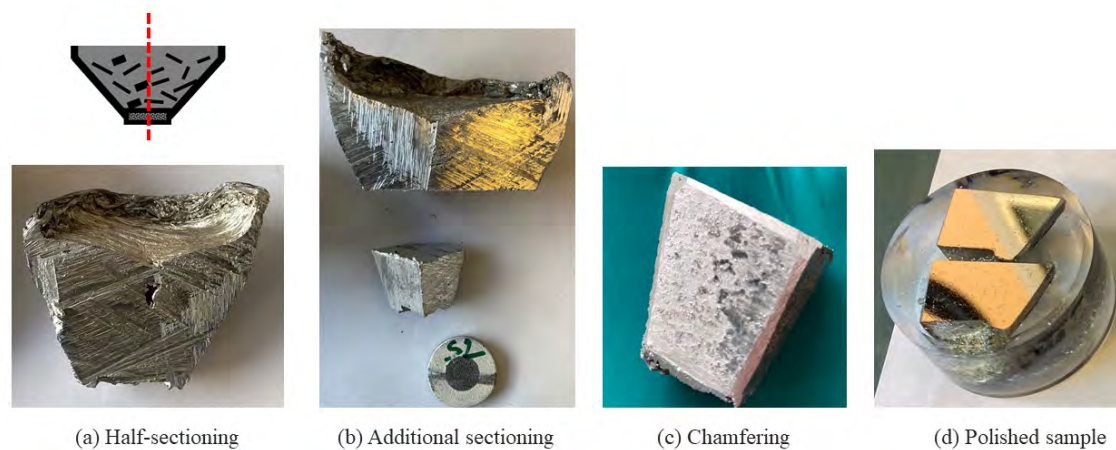


Figure 4.5 Polishing for light and electron microscopy analysis

Crystallography was evaluated through Transmission Electron Microscopy (TEM) analysis. To do so, supplementary sectioning of polished samples (Figure 4.6a) was carried out to extract $4\text{mm} \times 4\text{mm}$ specimens (Figure 4.6b), that were subsequently re-polished (4.6a and b) with a $0.5\mu\text{m}$ polishing pad. Focused Ion Beam (FIB) preparation was carried out to extract $4\mu\text{m} \times 20\mu\text{m}$ lamella for TEM analysis.

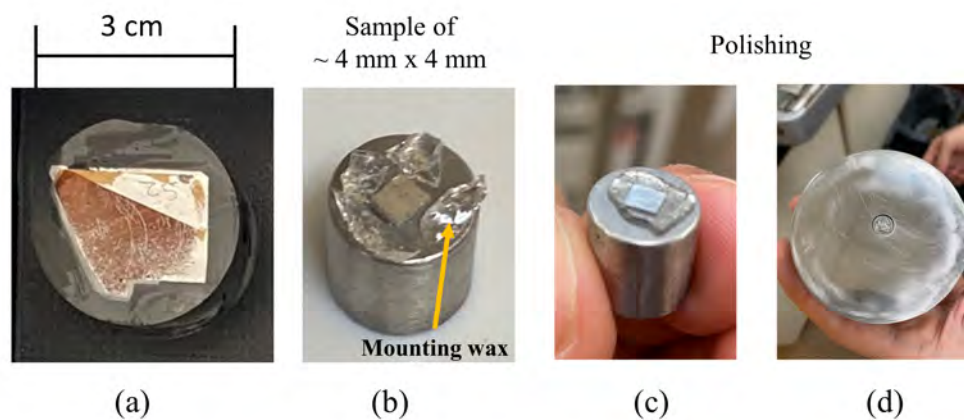


Figure 4.6 Polishing for TEM analysis.

4.2.3 Crystallographic determination

Lattice parameters for cubic and tetragonal phases were determined using equations 4.6 and 4.7, respectively [142].

$$\frac{1}{d^2} = \frac{h^2 + k^2 + l^2}{a^2} \quad (4.6)$$

$$\frac{1}{d^2} = \frac{h^2 + k^2}{a^2} + \frac{l^2}{c^2} \quad (4.7)$$

Where a and c are the lattice parameters and d is the distance between adjacent planes in the set (hkl) . The d parameter is obtained from the Selected Area Electron Diffraction (SAED) patterns from TEM analysis.

Angles, ϕ , between planes $(h_1k_1l_1)$ and $(h_2k_2l_2)$ were corroborated with equation 4.8 for cubic phases and with equation 4.9 for tetragonal intermetallics [142].

$$\phi = \arccos \left[\frac{h_1h_2 + k_1k_2 + l_1l_2}{\sqrt{(h_1^2 + k_1^2 + l_1^2)(h_2^2 + k_2^2 + l_2^2)}} \right] \quad (4.8)$$

$$\phi = \arccos \left[\frac{\frac{h_1h_2+k_1k_2}{a^2} + \frac{l_1l_2}{c^2}}{\sqrt{\left(\frac{h_1^2+k_1^2}{a^2} + \frac{l_1^2}{c^2}\right)\left(\frac{h_2^2+k_2^2}{a^2} + \frac{l_2^2}{c^2}\right)}} \right] \quad (4.9)$$

**CHAPTER 5 ARTICLE 1 : ON THE TRANSFERABILITY OF
CLASSICAL PAIRWISE ADDITIVE ATOMISTIC FORCE FIELD TO THE
DESCRIPTION OF UNARY AND MULTI-COMPONENT SYSTEMS:
APPLICATIONS TO THE SOLIDIFICATION OF AL-BASED ALLOYS**

Juan-Ricardo Castillo-Sánchez,^a Antoine Rincant,^a Aïmen E. Gheribi,^a Jean-Philippe Harvey^{a*}

^a Centre for Research in Computational Thermochemistry (CRCT), Department of Chemical Engineering, Polytechnique Montréal, C.P. 6079, Succursale “Downtown”, Montréal, Québec H3C 3A7, Canada. E-mail: jean-philippe.harvey@polymtl.ca

Submitted to Physical Chemistry Chemical Physics on June 17, 2022

5.1 Abstract

Multi-component and multiphase materials are continually being developed for electronics, aircraft, automotive, and general applications. Integrated Computational Materials Engineering (ICME) is a multiple-length scale approach that greatly benefits from atomistic scale simulations to explore new alloys. Meso-scale simulations are often used to account for the effect of metallurgical features such as grains and dislocations on diffusion. Molecular Dynamics (MD) allows to perform large-scale simulations by using classical interatomic potentials. Acquisition of a reliable force field model for describing the interactions between atoms constituting a system is one of the most pressing challenges in MD. For metals, parameters for such modeling can be directly derived via Density-functional theory (DFT) calculations. The main challenge of using such a classical approach is the transferability of the interatomic potentials from one structure to another when one aims to study multi-component systems. In this work, the reliability of Zr, Al-Cu, Al-Cr and Al-Zr-Ti force field potentials is examined. It has been found that current interatomic potentials are not completely transferable due to the structure dependence from their parameterization. Besides that, they provide an appropriate description of unary and binary systems, notably for liquids, isotropic solids, and partially isotropic compounds. The accuracy of current force field models is compromised for more complex tasks such as in modeling the Al₃(Zr,Ti)-based pseudo-binary solid solutions. For solidification purposes, it has been found that coherent primary solidification of the FCC-phase in pure Al is highly dependent on the formalism to tune interatomic interactions. For Al-Cr alloys, the icosahedral short-range ordering (ISRO) increased by adding Cr to the melts. The different steps of solidification (formation of nuclei, effective germination

of the α -Al phase and end of solidification) have been related to the evolution of the ISRO. The addition of Cr in melts prevented undercooling via icosahedral-enhanced nucleation of the α -Al phase. Precipitation of primary intermetallics in hyper-peritectic Al-Cr and Al-Zr-Ti alloys was also tested. Contrary to classical thermodynamics predictions, α -Al phase was the primary precipitate for these alloys. This implies that peritectic elements (Cr, Zr, Ti) supersaturated the α -Al phase rather than forming intermetallic phases due to the high cooling rates.

5.2 Introduction

During the last decade, the exploration of innovative materials based on multi-constituent and multi-phasic metallic systems has grown considerably [143–146]. For instance, High Entropy Alloys (HEAs) are a class of innovative materials made up of a large number of elemental components (more than five) with outstanding properties such as extraordinary wear strength, high hardness, phenomenal high-temperature strength, and strong corrosion resistance [147–149]. This is a result of their substantially higher mixing entropies compared to traditional alloys [150], which energetically stabilize disordered solid solutions at high temperature. To design these materials, one must predict their thermodynamic and elastic properties with regard to their chemical composition for some imposed temperature and pressure (or volume) [151, 152]. Experimental pilot tests to develop such complex materials result in expensive, time consuming and environmentally inefficient syntheses, machining and testing experiments. In this context, numerical physics could play an important role to overcome such challenges [153, 154]. Computational quantum mechanical modeling methods, notably those based on Density Functional Theory (DFT), have the highest predictive abilities since they explicitly consider the effect of the electronic structure of individual atoms on the energetic behavior of the considered system [155, 156]. Unfortunately, these calculations are limited to hundreds of atoms with the actual available computational resources [157], resulting in an overall deviation of the simulated thermodynamic, thermal and volumetric properties when compared to actual bulk materials. These materials often present metallurgical features such as grains and grain boundaries at a much larger scale (i.e. micron scale).

Simulations based on Equilibrium Molecular Dynamics (EMD) are nowadays widely employed to describe the equilibrium and dynamic properties, as well as thermal transport properties of metallic systems [158]. EMD typically cannot rigorously describe the electronic density surrounding individual atoms because of the simplified nature of the interatomic potential functions used in these simulations. Therefore EMD simulations cannot be as precise as DFT-

based calculations when it comes to the evaluation of energetic properties, especially when metallic interactions are involved. Instead, EMD is based on a force field function depending mainly on interatomic distances between atoms constituting the system under study, which lowers the computational cost compared to DFT [159]. The accuracy of EMD in predicting the material's thermodynamic properties strongly depends on the reliability of the force field formulated to describe the different contributions of the interactions between each atom of the studied supercell. For metallic systems, there exists a large variety of analytical force field formalisms to modulate the interatomic interactions; for instance, the Embedded Atom Method (EAM) [160], the Finnis–Sinclair (EAM-FS) [161], Second-Moment Approximation of the Tight-Binding scheme (TB-SMA) [162] and the Modified Embedded Atom Method (MEAM) potential [163]. The original MEAM formalism was extended in order to consider the second nearest-neighbor interactions, which is called the Second Nearest-Neighbor Modified Embedded-Atom-Method (2NN-MEAM) [53]. This formalism is widely used in the recent literature, especially for metallic systems, due to its good predictive abilities. Remarkably, a potential database is available for almost all pure metals [164–169]. Recent research on the description of binary [170] and ternary [171–173] systems is paving the way towards the numerical exploration of high entropy alloys of tremendous interest for various applications. In particular, those based in Al-Cu-Fe-Ni-Mn-Cr-Ti-Zr-X (X=others important metals) systems. The advantage of the MEAM potential is that only a few set of parameters is needed for its modeling, this allows to create homogeneous databases.

The parameterization strategy of the force field using the 2NN-MEAM formalism has been explained in detail by Lee and Baskes [53]. Elements are commonly parameterized from well-known crystallographic structures (such as face-centered cubic FCC, body-centered cubic BCC, and hexagonal close-packed HCP structures) at standard conditions of pressure and temperature (10^5 Pascal and 298.15 K) [165]. For binary systems, force field parameters can be directly obtained from first-principles calculations. Required information includes: (a) the strength of the energetic interactions at the ground state (obtained via the sublimation energy), (b) the bulk modulus, (c) equilibrium atomic volume from a reference crystal structure, (d) defect formation energies, and (e) elastic constants of some reference structures. The energetic description of binary systems can supposedly be obtained from the selection of any reference structure (i.e. regardless of the composition ratio of the two elements involved) as these interatomic potentials aimed at being universal functions. However, we found here that it is preferable to relate the reference structure to the one of a thermodynamically stable intermetallic compound observed in a measured phase diagram. In this case, the parameterization procedure is based on experimentally measured properties [174], which may not be self-consistent with DFT-based simulations. In some cases, the reference structure is related

to a metastable compound, such as the selection of the $\text{Al}_3\text{Li-L1}_2$ reference structure in the energetic description of the Al-Li system [175], or to a simple binary structure, such as the rock-salt NaCl structure (B1) in the Al-Cu parameterization with the 1NN-MEAM formalism [176, 177]. In the case of the MD study of the Al-Li system, the specific exploration of the energetic behavior of the L1_2 metastable phase justifies the selection of the reference structure [175]. In fact, any hypothetical reference structure can be used if first-principle calculations are available in the literature. One has to remember that the chosen reference structure modulates the various pair fractions to be accounted for in the evaluation of the internal energy of the system. This is a critical aspect to consider when tuning the strength of heterogeneous A-B energetic interactions. As an example, the fraction of A-B first nearest neighbor pairs in a hypothetical AB - B2 ordered structure is equal to one. In this case, only the A-B interactions influence the energetic behavior of the reference structure (in the 1NN approximation). The isotropy of the reference structure is another major aspect to consider when optimizing an interatomic potential. In principle, an isotropic reference structure is more suitable for describing liquid solutions, while most stable solid phases are not. In this context, DFT is a wonderful tool because it allows the access to the energetic behavior of isotropic structures of metastable phases and liquid solutions as well [52, 178, 179].

There is no strict methodology to judge the accuracy and transferability of a given interatomic potential. Nonetheless, it should be able to reproduce key equilibrium properties of specific solid structures, in particular, cohesive energy, lattice constants, elastic constants, surface energy, and energetics of defects, among others. This should be coupled with a satisfactory thermodynamic description of enthalpy of mixing, thermal conductivity, and other properties of liquids if reference data are available. In principle, a suitable force field is transferable from one structure to another as well as for the description of multicomponent solutions where many unary and binary interactions are simultaneously present. Most of the force field potentials are currently based on pairwise interactions [180]. Many-body interactions can partially be captured through a screening function in sophisticated formalisms, such as in the MEAM modeling. The three-body screening function in the 2NN-MEAM considers the effect of a third atom on the interaction between a pair of atoms [181]. Such approximations have limitations for multi-component systems as the chemical surrounding of a given atom (or pair) may vary. From continuum thermodynamics, it is well-established that ternary and quaternary energetic interaction corrections are needed to properly describe the enthalpy of mixing of multi-component systems when experimental data are available [182, 183]. This brings us to the following questions: a) How accurately can we describe the energetic behavior of multi-component metallic systems using the parameterization of two-body interactions from unary and binary systems only? and b) How is the choice of the reference structure

impacting the prediction of thermodynamic properties of multi-component systems?

Conventionally, the classical EAM formalism requires a significant number of empirical parameters to accurately describe a specific condensed phase. However, this large number of parameters does not necessarily ensure that the interatomic potential will be transferable to liquid and solid solutions. Srinivasan et al. [184] recently compared the predictive strength of two popular interatomic potentials used to perform MD simulations of metals. They found that for the binary Ni-Ti system, the 2NN-MEAM potential outperforms the EAM-FS potential. The 2NN-MEAM potential was able to estimate transformation strain, Young's modulus, lattice constants, and elastic constants with better accuracy than the EAM-FS [184]. Moreover, up to a thousand parameters are needed for some EAM interatomic potentials, whilst MEAM formalism is based on a simpler and more reliable parameterization which is believed to ensure a better transferability from one system to another.

Large-scale molecular dynamics simulations have become relevant to studying solidification in metals. Hou et al. [117] studied the effect of the cooling rate in pure aluminum. They worked with simulation boxes of 1 048 576 atoms and used an embedded atoms method (EAM) potential [118] to describe the Al-Al interactions. They worked with cooling rates between 0.1 and 10 K/ps. They found that the fastest cooling rate (10 K/ps) promoted the formation of metallic glasses with short-range icosahedral ordering. Simulation boxes solidified into the FCC and HCP phases for slower cooling rates (≤ 4 K/ps). Crystallization of the metastable HCP phase was associated with twinning. Zhang et al. [119] used cubic simulation boxes of 3 456 000 atoms to study the rapid solidification in pure iron melts. They used the embedded atoms method (EAM) potential [120] to describe the iron interatomic interactions and used cooling rates between 0.09 5K/ps and 9.5 K/ps. They concluded that the icosahedral ordering was promoted in undercooled melts by increasing the cooling rate. They reported a critical cooling value of 4 K/ps for glass transition. i.e., above this value, the icosahedral-like configurations were dominant and led to the formation of amorphous structures. Below the critical value, crystalline structures were obtained. These studies provided insights into the solidification mechanisms of pure systems. However, solidification simulations for multicomponent systems are required to design new alloy. Harvey & Asimow [185] pointed out some of the current limitations of MD simulations for the thermodynamic description of silicate melts, which are related to the time and length scales as well as the fundamental description of interatomic interactions. This study aims to evaluate the effect of such limitations on the solidification of Al-based alloys.

In this work, the transferability of a series of interatomic potentials has been evaluated for specific applications linked to the solidification of metallic systems. Firstly, the impact of

using two distinct reference allotropes (i.e. HCP and BCC) on the energetic description of pure liquid Zr is explored. Secondly, the effect of the selection of a given binary reference structure on the prediction of the phase stability in the Al-Cu system is analyzed using three different metastable compounds as reference structures (i.e. $\text{Al}_3\text{Cu-L1}_2$, $\text{Cu}_3\text{Al-L1}_2$ and AlCu-BCC with self-consistent data obtained from DFT calculations). Solidification of pure Al is studied using two of the most popular models in MD (i.e. the EAM.FS and 2NN-MEAM formalism). The transferability of classical pairwise interatomic potentials is evaluated for the icosahedral-enhanced nucleation of the FCC-phase [7] in Al-Cr alloys. Finally, an interatomic potential is tested for the solidification and energetic description of pseudobinary solid solutions within the Al-Zr-Ti system. Particular interest is given to the $\text{Al}_3\text{Ti-D0}_{22}$ and $\text{Al}_3\text{Zr-D0}_{23}$ intermetallics as they can act as nucleant particles for heterogeneous nucleation of the FCC-phase in aluminum alloys [45–48].

5.3 Force field development

The Second Nearest-Neighbor Modified Embedded-Atom-Method (2NN-MEAM) [53], commonly denoted only as MEAM, was used to describe the strength of the interatomic interactions in our work. This formalism is integrated as a package of the popular LAMMPS code [186] for Equilibrium Molecular Dynamic (EMD) simulations. The MEAM potential can accurately capture the directionality of metallic bonds due to the implicit angle-dependent terms [184]. Total energy with the MEAM formalism is defined by two contributions: an embedding function (F) and a pair potential function (ϕ_{ij}):

$$E = \sum_i \left\{ F(\bar{\rho}_i) + \frac{1}{2} \sum_{i \neq j} \phi_{ij}(R_{ij}) \right\} \quad (5.1)$$

Where $\bar{\rho}_i$ is the background electron density at the site of the i -th particle and R_{ij} is the distance between particles i and j . The embedded function is given by:

$$F(\bar{\rho}_i) = AE_c \frac{\bar{\rho}_i}{\rho^0} \ln\left(\frac{\bar{\rho}_i}{\rho^0}\right) \quad (5.2)$$

Where A is a specific parameter of the MEAM formalism. E_c is the cohesive energy and $\bar{\rho}^0$ is the background electron density of the reference structure. Background electron density is related to the angular dependent partial electron densities, $\rho_i^{(k)}$, and to the weighting parameters, $t(k)$, via equations 5.3 and 5.4. $t(1)$, $t(2)$, and $t(3)$ are respectively adjusted according to the relevance of the p, d and f orbitals [187].

$$\bar{\rho}_i = \rho_i^{(0)} \frac{2}{1 + e^{-\Gamma_i}} \quad (5.3)$$

$$\Gamma_i = \sum_{k=1}^3 t^{(k)} \left(\frac{\rho_i^{(k)}}{\rho_i^{(0)}} \right)^2 \quad (5.4)$$

The pair potential function is estimated using the following equation:

$$\phi_{ij}(R_{ij}) = \psi(R_{ij}) + \sum_{n=1} (-1)^n (Z_2 S / Z_1)^n \psi(a^n R_{ij}). \quad (5.5)$$

Where Z_1 and Z_2 are the number of first and second nearest-neighbor atoms, respectively. a is the ratio between the second and first nearest neighbor distances, S is a screening function on the second nearest-neighbor interactions and $\psi(R_{ij})$ is pair function obtained with the following equation :

$$\psi_{ij}(R_{ij}) = \frac{2}{Z_1} \{E^u(R_{ij}) - F[\bar{\rho}^0(R_{ij})]\} \quad (5.6)$$

The total energy per atom, $E^u(R_{ij})$, is obtained from the universal equation of state [188]:

$$E^u(R_{ij}) = -E_c \left(1 + a^* + da^{*3}\right) e^{-a^*} \quad (5.7)$$

With $a^* = \alpha(R_{ij}/r_e - 1)$ and $\alpha = \left(\frac{9B\Omega}{E_c}\right)^{1/2}$. Where d is an adjustable parameter. E_c is the cohesive energy, r_e is the equilibrium distance, B is the bulk modulus, and Ω is the equilibrium atomic volume of the reference structure.

The optimized parameters to describe the pure metal pairwise interactions via the 2NN-MEAM formalism are presented in Table 5.1. They were primarily taken from Kim and Lee studies [164–166], except for the BCC-based potential for Zr, which was parameterized in this work.

As previously stated, the parameterization of a binary interatomic potential using the 2NN-MEAM formalism relies on the selection of a binary reference structure. Popular Molecular Dynamics programs such as [186] and KISSMD [174] can support different reference structures, essentially, the rock-salt NaCl structure (B1), and the BCC-like CsCl structure (B2), the AuCu₃-prototype (L1₂), among others. In ideal conditions, it is preferable to associate the binary reference structure with a stable intermetallic compound as it ensures the most accurate description of a given binary interaction. However, this cannot always be achieved

Table 5.1 2NN-MEAM potential parameter sets for pure Al, Zr, Cu, Cr and Ti. The units of the cohesive energy E_c , equilibrium nearest-neighbor distance r_e , and bulk modulus B are eV, Å and 10^{12} dyne/ cm², respectively. The reference structure for Al and Cu is fcc, bcc for Cr, hcp for Ti and two references for Zr, i.e. bcc and hcp.

	E_c	r_e	B	A	$\beta^{(0)}$	$\beta^{(1)}$	$\beta^{(2)}$	$\beta^{(3)}$	$t^{(1)}$	$t^{(2)}$	$t^{(3)}$	C_{min}	C_{max}	d
Al [165]	3.36	2.860	0.794	1.16	3.20	2.6	6.0	2.6	3.05	0.51	7.75	0.49	2.80	0.05
Zr-BCC	6.29	3.100	0.900	0.95	3.30	1.0	1.0	1.0	5.80	-0.35	-1.30	0.25	2.80	0.00
Zr-HCP [166]	6.36	3.200	0.970	0.68	2.45	1.0	3.0	2.0	6.30	-3.30	-10.00	1.00	1.44	0.00
Cu [165]	3.54	2.555	1.420	0.94	3.83	2.2	6.0	2.2	2.72	3.04	1.95	1.21	2.80	0.05
Cr [164]	4.10	2.495	1.900	0.42	6.81	1.0	1.0	1.0	0.30	5.90	-10.40	0.78	2.80	0.00
Ti [166]	4.87	2.920	1.100	0.66	2.70	1.0	3.0	1.0	6.80	-2.00	-12.00	1.00	1.44	0.05

as the crystal structure of the stable intermetallic compound may not be supported by the classical MD package or simply because they may not be a stable binary compound for that particular binary system. A sound strategy to properly select the reference structure from first-principle calculations is to compare its enthalpy of formation with the one computed by classical thermodynamics packages such as FactSage which exploit CALPHAD-based thermodynamic databases (which are built using a collection of critically assessed experimental data found in the literature).

Figure 5.1 shows the enthalpy of formation (refs.: Al-FCC and Cu-FCC) for several reference structures coming from DFT calculations at 0 K (black spheres) [11] compared with the enthalpy of formation at 298.15 K of the solid system computed with the FTlite database [12] (black line). It can be observed that the enthalpy of formation calculated via DFT for Al₂Cu (I4/mcm), AlCu (C2/m), Al₄Cu₉, AlCu₃ (L1₂) and AlCu₃ (IA/mcm) structures are in excellent agreement with the thermodynamic calculations. From this list of compounds, only the AlCu₃ (L1₂) reference structure is supported by LAMMPS [186] and KISSMD [174] when using the 2NN-MEAM. Therefore, this reference structure was used for the construction of one force field model in this work (see table 5.2). AlCu₃ (L1₂) and AlCu (B2) DFT references were also considered to parametrize the Al-Cu interactions of two additional models (Table 5.2). It is to be noted that none of these compounds are reported as stable phases in the equilibrium Al-Cu phase diagram. Out of these three reference structures, the AlCu₃ (L1₂) has the closest enthalpy of formation to the CALPHAD curve (obtained from computational thermochemistry). The enthalpy of mixing in the liquid state (refs.: Al-liq. and Cu-liq.) calculated with the FTlite database is also presented in Figure 5.1. The minimum value on this enthalpy of mixing curve is shifted towards a Cu molar fraction of 0.6 (red curve in Figure 5.1), which represents a modelling challenge in both EMD and computational thermochemistry. This shift implies that a specific local ordering is established in the liquid

phase, which appears to be also present in the solid state.

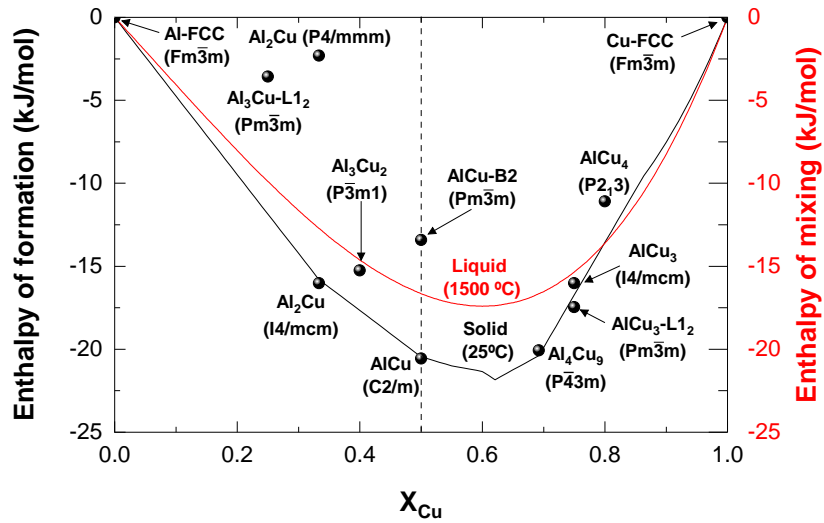


Figure 5.1 Enthalpy of formation of different compounds from DFT calculations (black spheres) [11] compared with the solid (25°C) and liquid (1500°C) enthalpies of formation computed to the critically assessed value [12].

The Cr-Al and Al-Zr energetic interactions were also tuned from equilibrium reference structures at 0K obtained via DFT calculations [11]. A hypothetical Zr_3Ti-L1_2 reference structure was selected for the parameterization of the Zr-Ti interaction via the 2NN-MEAM formalism (Table 5.2). The enthalpy of formation for the Zr_3Ti-L1_2 reference was set to a value of +0.04eV (i.e. close to zero), which was determined by fitting the liquid enthalpy of mixing with a ± 1 kJ/mol margin of error compared to the critically assessed value (Figure 5.8). This virtually zero enthalpy of formation leads to an ideal solution behavior for this system. This is consistent with the current phase diagram calculated from the FTlite database of FactSage [12]. This phase diagram presented in Figure 5.3 shows that Ti and Zr are completely miscible in all the stable solutions (i.e. HCP, BCC and liquid). The energetics of the selected reference structures (black triangle and spheres in Figure 5.2) for the Al-Cr, Al-Zr and Ti-Zr interactions were compared with the CALPHAD curves at 298.15 K (blue, green and red solid lines), which were computed with the FTlite database [12]. Overall, this comparison confirms that the selected reference structures are consistent with computational thermochemistry calculations.

Screening parameters, C_{min} and C_{max} , for the modeling of the ternary Al-Zr-Ti system using the MEAM formalism, are presented in Table 5.3. Finally, the MEAM interatomic potential developed by Kim et al. (2016) [189] was used to describe the Al-Ti interactions needed

within the Al-Zr-Ti system.

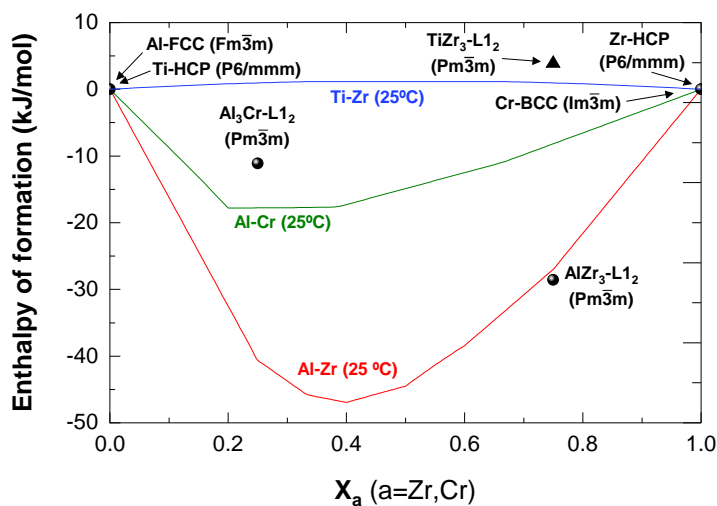


Figure 5.2 Enthalpy of formation of different compounds from DFT calculations (black spheres) [11], and the hypothetical $\text{Zr}_3\text{Ti-L}_{12}$ reference (black triangle) compared with the solid enthalpy of formation at 25°C computed to the critically assessed value [12].

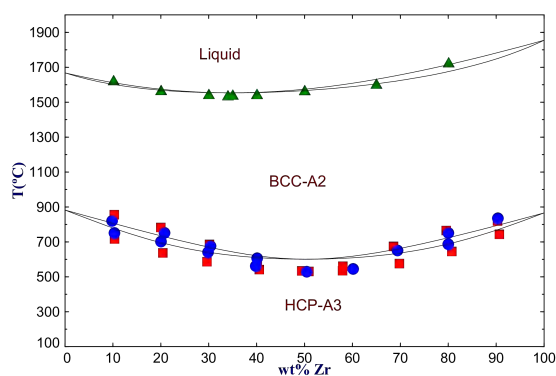


Figure 5.3 Ti-Zr phase diagram computed with Factsage [12]. Filled triangles, squares and circles are experimental data obtained from [13].

Table 5.2 Optimized 2NN-MEAM potential parameters for individual binary systems. The units of the cohesive energy E_c , equilibrium nearest-neighbor distance r_e , and bulk modulus B are eV, Å and 10^{12} dyne/cm², respectively.

	Cu-Al	Cu-Al	Cu-Al	Cr-Al	Al-Zr	Zr-Ti
Ref. structure	Cu ₃ Al - L1 ₂	CuAl - BCC_B2	CuAl ₃ - L1 ₂	CrAl ₃ - L1 ₂	Zr ₃ Al - L1 ₂	Zr ₃ Ti - L1 ₂
ΔE_c (eV)	-0.181	-0.140	-0.037	-0.115	-0.296	0.040
r_e	2.596	2.596	2.775	2.757	3.105	2.981
B	1.29	1.39	0.91	1.22	1.01	1.03
C_{min} (A-B-A)	0.09	1.21	1.21	0.25	1.00	1.00
C_{min} (B-A-B)	0.09	0.81	0.49	0.49	1.00	1.00
C_{min} (A-A-B)	0.09	0.81	0.81	0.25	0.81	1.00
C_{min} (A-B-B)	0.09	0.81	0.81	0.36	0.81	1.00
C_{max} (A-B-A)	1.44	2.80	2.80	2.80	1.44	2.80
C_{max} (B-A-B)	1.44	2.80	2.80	2.80	1.44	2.80
C_{max} (A-A-B)	1.44	2.80	2.80	2.80	2.80	2.80
C_{max} (A-B-B)	1.44	2.80	2.80	2.80	2.80	2.80
d	$0.75d^{Cu} + 0.25d^{Al}$	$0.50d^{Cu} + 0.50d^{Al}$	$0.25d^{Cu} + 0.75d^{Al}$	$0.25d^{Cr} + 0.75d^{Al}$	$0.75d^{Zr} + 0.25d^{Al}$	$0.75d^{Zr} + 0.25d^{Ti}$
ρ_0	$\rho_0^{Cu} = \rho_0^{Al} = 1$	$\rho_0^{Al} = \rho_0^{Cr} = 1$	$\rho_0^{Cu} = \rho_0^{Al} = 1$	$\rho_0^{Al} = \rho_0^{Cr} = 1$	$\rho_0^{Al} = \rho_0^{Zr} = 1$	$\rho_0^{Al} = \rho_0^{Ti} = 1$

Table 5.3 Default value for MEAM-2NN potential parameters of the Ti-Zr-Al ternary system.

Parameter	Selected value
$C_{min,max}^{Ti-Al-Zr}$	$\left(\frac{1}{2}\sqrt{C_{min,max}^{Ti-Al-Ti}} + \frac{1}{2}\sqrt{C_{min,max}^{Zr-Al-Zr}}\right)^2$
$C_{min,max}^{Ti-Zr-Al}$	$\left(\frac{1}{2}\sqrt{C_{min,max}^{Ti-Ti-Al}} + \frac{1}{2}\sqrt{C_{min,max}^{Zr-Zr-Al}}\right)^2$
$C_{min,max}^{Zr-Ti-Al}$	$\left(\frac{1}{2}\sqrt{C_{min,max}^{Zr-Zr-A}} + \frac{1}{2}\sqrt{C_{min,max}^{Ti-Ti-Al}}\right)^2$

5.4 Simulations details

Molecular Dynamics simulations were performed using the LAMMPS code [186]. Temperature and pressure were controlled by a Nose-Hoover thermostat and barostat [127–130]. Periodic boundary conditions were used for the three Cartesian directions. Newton’s equation of motion was solved by means of the velocity-Verlet method [131] using a time step of 1 fs. Structural analysis was carried out with OVITO software [133], using the Common Neighbor Analysis (CNA) [134] and the Polyhedral Template Matching (PTM) reported by Larsen et al. [8]. Quantification of the local structure was performed with the Radial Distribution Function (RDF). It describes the probability of finding atoms as a function of the distance from a reference particle compared to the probability of finding an atom at these same interdistances in an ideal gas. It is mathematically defined by the following equation [132]:

$$g_{ij}(r) = \frac{\left\langle \sum \delta_{ij}(r - r_{ij}) \right\rangle}{4r\pi^2\rho_0} \quad (5.8)$$

where r_{ij} is the distance between atoms i and j , ρ_0 is the mean number density. The total RDF is related to the partial RDF by the following expression:

$$g(r) = x_\alpha^2 g_{\alpha\alpha}(r) + 2x_\alpha x_\beta g_{\alpha\beta}(r) + x_\beta^2 g_{\beta\beta}(r) \quad (5.9)$$

Where x_α and x_β are the molar fractions of the the species α and β . $g_{\alpha\alpha}$, $g_{\alpha\beta}$ and $g_{\beta\beta}$ are the partial functions obtained with equation 5.8.

Bond-Angle Distribution Function or Angular Distribution Function (ADF), quantifies the probability of forming an angle θ from two nearest neighbours of a reference central atom. It is given by the following equation [190]:

$$g(\theta) = 16\pi^2 \int_0^{D_1} \int_0^{D_1} R_1^2 R_2^2 g(R_1) g(R_2) g_3(R_1, R_2, \theta) dR_1, dR_2 \quad (5.10)$$

Where D_1 is the maximum distance between a central atom and its first nearest neighbor atoms (first minimum on the RDF) and $g_3(R_1, R_2, \theta)$ is a triplet correlation function.

5.4.1 Thermodynamic property evaluation

The specific (molar) enthalpy of mixing (Δh_{mix}) of liquid solutions at a given temperature was calculated using the following equation:

$$\Delta h_{mix}^{liq.} = h_{liq.} - \sum x_i h_i \quad (5.11)$$

Where $h_{liq.}$ is the equilibrium enthalpy of the molten alloy, x_i and h_i are respectively the molar fraction and the molar enthalpy of the pure liquid of constituent "i" at the same temperature and pressure conditions.

The molar enthalpy of formation at 0 K (Δh_f^{0K}) of solid phases was computed by the following equation:

$$\Delta h_f^{0K} = h_{comp}^{0K} - \sum x_i h_i^{SER-0K} \quad (5.12)$$

In eq. 5.12, h_{comp}^{0K} is the molar enthalpy of the compound, and x_i is the molar fraction of the "i" component within the solid phase. In all our calculations, the enthalpy of the solid structure at 0 K was obtained at a null pressure via a volume minimization of the studied supercell. Finally, h_i^{SER-0K} refers to the enthalpy of pure element i evaluated at 0 K under its Standard Element Reference state (defined as SER-0K).

5.4.2 MD simulations of solidification and precipitation

The MD simulation for the solidification of pure aluminum and of the icosahedral-enhanced nucleation of the FCC-phase of Al-Cr alloys presented in section 5.5 were carried out with the following conditions. The Al-Cr compositions (at. %) that were investigated are $x_{Cr} = 0, 0.1, 0.5, 0.75, 1$ and 7 respectively. Simulations were performed using the MEAM potential developed in this work and were compared with a model from the Finnis and Sinclair (FS) formalism [20].

The exploration of the potential icosahedral ordering and eventual precipitation of Al_3Zr and Al_3Ti intermetallics from liquid aluminum melts was performed using the composition reported in Table 5.4.

Table 5.4 Crystallization of Al-Ti-Zr alloys

	wt. %		
	Al	Zr	Ti
Sample 1	Balance	0.11	0.18
Sample 2	Balance	0.23	1.20

5.4.3 Energetics of partially ordered $D0_{22}$ and $D0_{23}$ solid solutions

Our last series of MD simulations is related to the energetic description of partially ordered $Al_3(Zr,Ti)-D0_{23}$ and $Al_3(Ti,Zr)-D0_{22}$ solid solutions, which are of prime importance in aluminum alloys [45–48]. The modeling was first carried out with first-principle calculations. Results were after compared to MD predictions using the Al-Zr-Ti interatomic potential developed in this work.

The Vienna ab initio Simulation Package (VASP) [191–194] has been used to perform the plane wave density functional theory (DFT) simulations to determine the enthalpy of formation and the lattice constants of both $Al_3(Ti,Zr)$ in both $D0_{22}$ and $D0_{23}$ structures. Pseudopotentials constructed by the projector-augmented wave (PAW) method originally proposed by Blöchl [195, 196] were employed for Al, Ti and Zr. The generalized gradient approximation (GGA) of Perdew, Burke and Ernzerhof (PBE) [197, 198] has been considered to describe the exchange-correlation functionals. Convergence in the energy and cell volume was achieved by using a cut-off energy of 520 eV. The Monkhorst-Pack scheme was used to sample the Brillouin zone with a $3 \times 3 \times 1$ k-point mesh for both $D0_{22}$ and $D0_{23}$ structures. Zone with a Gaussian smearing parameter σ of 0.02 eV ensure that the accuracy in the energy of the system is more than 0.01 meV. The self-consistent field (SCF) convergence criterion was 1×10^{-5} eV for electronic iteration and 0.02 eV/Å for each ionic loop that was updated by the conjugate gradient approach. The total energy has been calculated in the NPT statistical ensemble, i.e the equilibrium lattice, the atomic positions, cell volume and cell shape, all were free to be relaxed. A total of 128 and 256 atoms have been considered for $D0_{22}$ and $D0_{23}$ structures respectively. Several configurations in which Ti and Zr were randomly substituted have been generated. Volume optimization for MD simulations was performed using the equilibrated supercells from DFT as initial configurations. The corresponding 0 K molar enthalpy of mixing (Δh_f^{soln}) have been determined as:

$$\Delta h_f^{soln} = h_{Al_3Y_{1-x}Z_x} - (1-x)h_{Al_3Y}^{Ref-0K} - xh_{Al_3Z}^{CSS-0K} \quad (5.13)$$

In this equation, $h_{Al_3Y_{1-x}Z_x}$ is the molar enthalpy of the minimized pseudo-binary solid solu-

tion at 0 K, computed by volume minimization (with $Y=Zr$ and $Z=Ti$ for the $D0_{23}$ phase and vice-versa for the $D0_{22}$ phase). The fraction of sub-lattice substitution of Z sites by Y atoms in the tetragonal phases is defined in this equation by x . The $h_{Al_3Y}^{Ref-0K}$ expression represents the molar enthalpy of the binary stable reference structure at 0K while $h_{Al_3Z}^{CSS-0K}$ refers to the molar enthalpy of the reference structure with complete sub-lattice substitution of Y atoms by Z atoms.

5.5 Results and discussion

5.5.1 Effect of the reference structure on the modeling of liquid Zr

Current interatomic potential models for elements are typically developed from their known reference structure at standard conditions of temperature and pressure (i.e. 10^5 Pa and 298.15 K). At high temperatures and pressure, some elements undergo solid allotropic transformations. This is the case for metallic elements such as Zr, Ti, Fe, and Mn. The allotropic transformation from α (HCP)-Zr to β (BCC)-Zr takes place at 1135 K [199], while its melting occurs at 2128.15 K [200]. In perfect (i.e. defect-free) solid structures, the atomic motion is highly limited by the long-range ordering and symmetry of the crystal. In this case, vibration is the principal type of atomic motion. For real/macroscopic solids, defects such as vacancies, grain boundaries, and dislocations allow more degree of freedom to the atoms which become more mobile (diffusion is possible). For liquids, the long-range order and symmetry are broken. This allows the atoms to move more freely in this condensed phase. Short-range ordering is still preserved in liquids and is a direct function of the strength of the different interactions in the melt. Moreover, it is known that only a small coordination shell (up to second or third nearest neighbors) typically impacts the cohesive energy of metallic condensed phases. In this context, how is this short-range ordering affected by the selection of the solid reference structure used for EMD? In other words, we need to identify which reference structure is more suitable for the description of liquid phases. This question was addressed in our work by simulating liquid Zr using an HCP-referenced pairwise interatomic potential available in the literature [166] and a BCC-referenced potential developed in this work (Table 5.1). Liquid simulation cells of 500 atoms were equilibrated at 2000 K during 50 ps in the NPT ensemble using KISSMD.

Figure 5.4a shows the effect of the solid reference structure of Zr on the radial distribution function (RDF) of liquid Zr at 2000 K. The Zr-BCC potential shows a better agreement with the experimental data of Schenk et al [15]. This figure also shows that the Zr-HCP potential is less accurate when compared to the experimental data. In fact, the predicted radial

distribution function curve with this reference structure was closer to the *Ab Initio* Molecular Dynamics data at 2000 K reported by Jakse & Pasturel [14]. For the case of the Angular Distribution Function (ADF) (Figure 5.4b), both BCC-based (blue line) and HCP-based (red line) results are slightly shifted to higher angles when compared to *Ab Initio* Molecular Dynamics calculations at 2000 K (Diamond symbols) from Jakse & Pasturel [14]. The BCC reference potential again outperforms the HCP reference potential. One explanation to justify why the BCC-based potential provides a much better agreement with the experimental data is that it is also the primary solidification structure upon the cooling of liquid Zr. The local ordering of this structure is also closer to the one experienced in the liquid. Moreover, the BCC structure is the stable Zr allotrope for a wide range of temperatures (i.e. from 1135 K to 2128.15 K). It is clear from these simulations that the reference solid structure has a direct impact on the local ordering of the liquid since the cohesive energy is tuned based on the local atomic environment (2NN approximation). These results also imply that the determination of physical properties of molten alloys including Zr in classical MD need to be performed using the BCC reference potential to ensure high accuracy. For low-temperature simulations (ex.: when calculating the energetics of partially ordered solid solutions), it is preferable to use the HCP reference as the BCC reference would lead to erroneous enthalpies (the contribution of the BCC-HCP allotropic transformation would not be accounted for in the simulations).

5.5.2 Potential transferability when evaluating the enthalpy of mixing of binary liquid solutions

The next case study to judge the transferability of classical interatomic potentials was the evaluation of the enthalpy of mixing of binary liquid solutions. To do so, liquid simulation cells of 500 atoms were equilibrated at specific compositions and temperatures during 30 ps by simulation steps of 1 fs. Enthalpy of mixing of Al-Cu at 1500 K using $\text{AlCu}_3\text{-L1}_2$, AlCu-BCC, and $\text{Al}_3\text{Cu-L1}_2$ as reference structures are presented in Figure 5.5. Modeling with the $\text{AlCu}_3\text{-L1}_2$ reference (green line and dots) exhibited the best description when compared with both experimental data and classical thermodynamic calculations. This metastable reference structure is isotropic. This Al-Cu interatomic potential version also leads to good agreement with the enthalpy of formation curve of solids computed with classical thermodynamics as presented in the force field development section of this work (Figure 5.1). Moreover, the AlCu_3 -based interatomic potential of this work was compared with a recent MEAM potential from Mahata et. al [42] (blue line and points in Figure 5.5) and with the Angular-Dependent interatomic Potential (ADP) proposed by Apostol & Mishin [43] (purple line and points in Figure 5.5). The MEAM potential developed in this work showed the best accuracy for

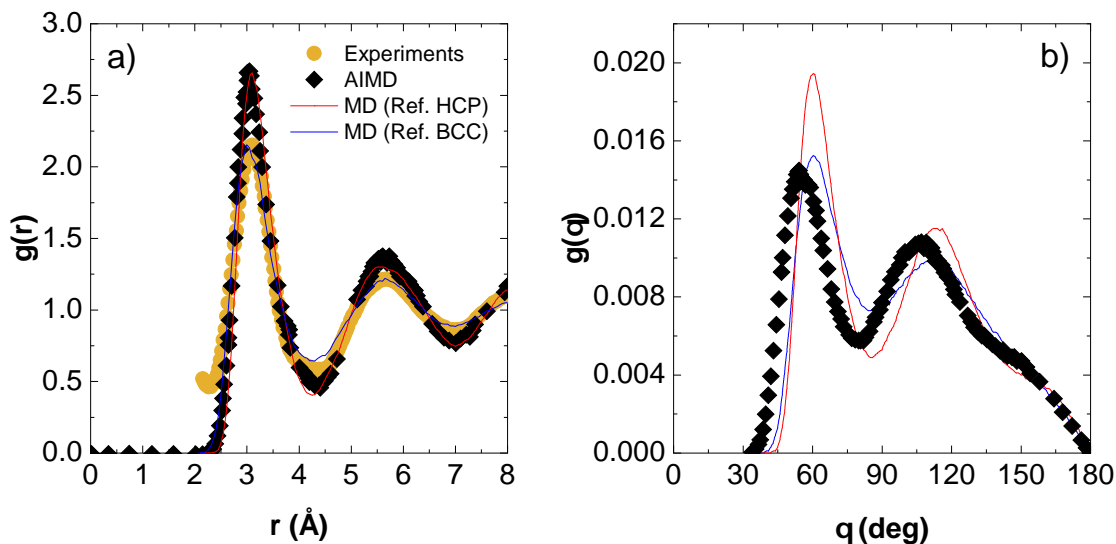


Figure 5.4 (a) Total Radial Distribution Function (RDF) for liquid Zr at 2000 K computed with MD for BCC (blue line) as reference structure and HCP (red line) as reference structure using the MEAM formalism. Diamond symbols are results from *Ab Initio* Molecular Dynamics at 2000 K from Jakse & Pasturel [14]. Dark yellow circles correspond to experimental data of Schenk et al [15]. The Angular Distribution Function (ADF) is presented in (b) for liquid Zr at 2000 K for BCC as reference structure (blue line) and HCP as reference structure (red line). Diamond symbols are results from *Ab Initio* Molecular Dynamics at 2000 K from Jakse & Pasturel [14].

describing the enthalpy of mixing for the Al-Cu system.

Enthalpy of mixing curves for Al-Cr, Al-Zr, and Zr-Ti liquid systems at 2000 K were computed using EMD (Figures 5.6, 5.7 and 5.8, respectively). The energetic description of the Al-Cr liquid phase using the MEAM potential of this work was in agreement with experimental data and thermodynamic calculations (Figure 5.6). On the other side, the FS potential drastically overestimated the strength of the Al-Cr interatomic interaction within the liquid phase. The authors have reported satisfactory description for specific FeCrAl ferrite-based alloys using this potential [20]. However, it appears from our simulations that this Al-Cr potential is not transferable to the exploration of Al-Cr liquid solution structures. The description of the Al-Zr liquid was also in good agreement with the enthalpy of mixing experimental data of Witusiewicz et al. [25] (Figure 5.7). Finally, the enthalpy of mixing for Ti-Zr the liquid solution evaluated with our MD simulations oscillated around zero, implying an ideal solution behavior which is consistent with the thermodynamic description of this liquid solution (Figure 5.8).

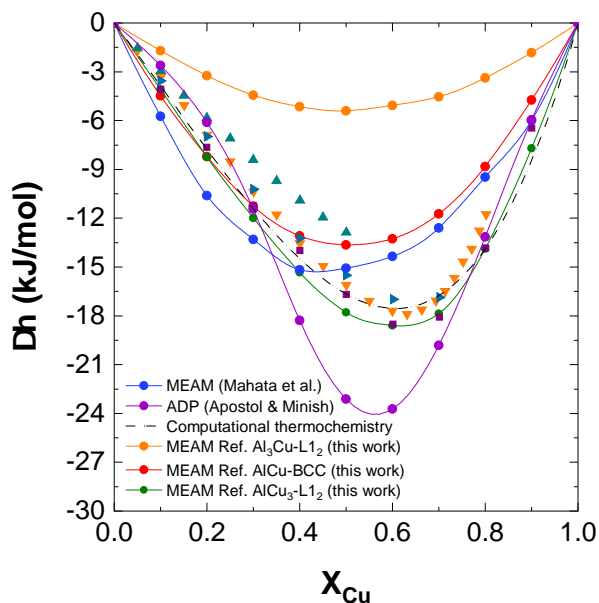


Figure 5.5 Molar enthalpy of mixing for liquid Al-Cu. Filled circles and line are the thermodynamic data calculated with MD at $T = 1500$ K. Experimental data from Stolz et al. [16] (orange triangles) at 1467 K, Kanibolotsky et al. [17] (blue triangles) at 1590 K, Gizenko et al. [18] (purple squares) at 1473 K, and Sandakov et al. [19] (cyan triangles) at 1773 K are presented as filled symbols. Dashed lines are results at 1500 K from classical thermodynamics performed with FactSage [12].

5.5.3 Potential transferability for describing the internal structure of the $\text{Al}_{80}\text{Cu}_{20}$ melt

The internal structure of liquid solutions is another essential information when studying the nucleation of solids during solidification. Therefore, the selected classical interatomic potential needs to capture the short-range ordering behavior of liquids if one wants to obtain useful insights from EMD. $\text{Al}_{80}\text{Cu}_{20}$ liquid simulation cells of 4 000 atoms were equilibrated at 1818 K during 0.5 ns by steps of 1 fs in the NPT ensemble. For the sake of comparison, EMD simulations were performed using the force field model based on the $\text{Al}_3\text{Cu-L1}_2$ reference developed in this work (table 5.2), the MEAM potential of Mahata et al. [42] and an Angular-Dependent interatomic Potential (ADP) from Apostol & Mishin [43]. Radial Distribution Function (RDF) and Angular Distribution Function (ADF) were averaged and extracted for the last 100 000 steps for each simulation. Structural properties were compared to AIMD of Wang et al. [44]. The total RDF computed by MD with these three different interatomic potentials present equivalent accuracy compared to AIMD (Figure 5.9a). The position of

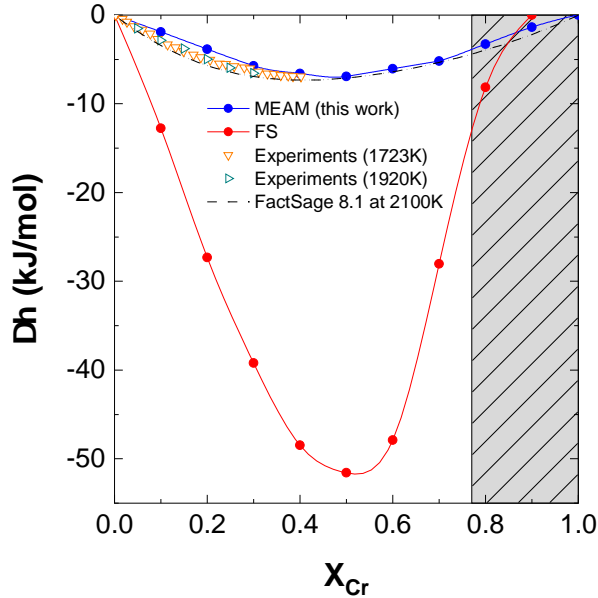


Figure 5.6 Enthalpy of mixing at 2000K calculated with MD using the MEAM potential (filled blue circles and line) and the FS potential (filled red circles and line) [20]. Experimental data from Saltykov et al. [21] (orange triangles) at 1723 and Sudavtsova et al. [22] (cyan triangles) at 1920 K are as open symbols. Dashed line are results at 2100 K from classical thermodynamics performed in FactSage [12]. Shaded grey zone correspond to the meta-stability zone of the liquid at 2000K.

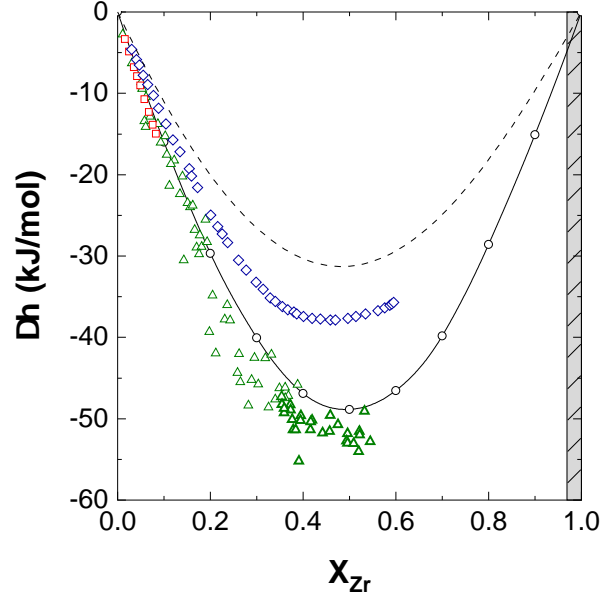


Figure 5.7 Molar enthalpy of mixing for liquid Al-Zr. Open circles and line are the thermodynamic data calculated with MD at $T=2000$ K. Experimental data from Esin et al. [23] (diamonds) at 1970 K, Sudavtsova et al. [24] (squares) at 1790 K, and Witusiewicz et al. [25] (triangles) at 2080 K are presented as open symbols. Dashed line are results at 2000 K from classical thermodynamics performed in FactSage [12]. The shaded grey zone corresponds to the meta-stability zone of the liquid at 2000K.

the first peak of the generalized RDF (Figure 5.9a) corresponds to the first nearest neighbor distance (r_{1NN}) [201]. Its length obtained from all the EMD simulations adequately matched the one obtained by AIMD. The first minimum of the RDF corresponds to the shell of first nearest neighbors (r_{1NN}^{shell}) [202]. This value is used as an integration limit to obtain the coordination number (Z). Atomistic simulations performed using the ADP interatomic potential provided a closer value of r_{1NN}^{shell} compared to AIMD. Both MEAM potentials models provide a slight shifting of the r_{1NN}^{shell} toward higher values. The coordination number with the MEAM potential of Mahata et al. was higher than the one in the closest packed FCC and HCP solids. Coordination numbers with the MEAM potential of this work and the

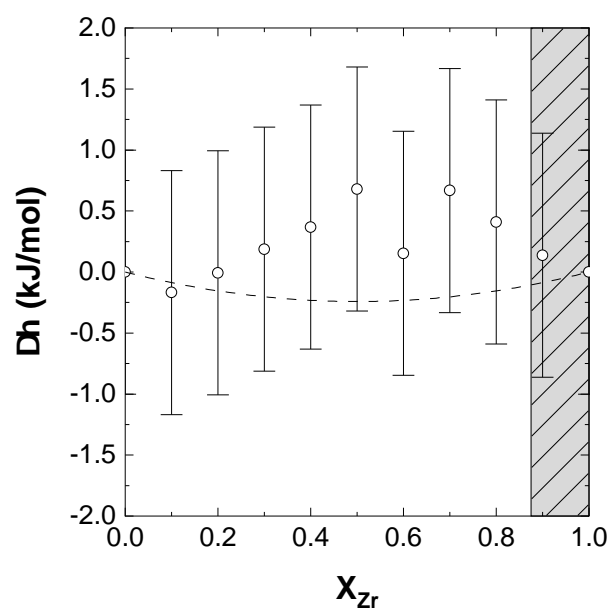


Figure 5.8 Molar enthalpy of mixing for liquid Ti-Zr. Open circles and line are the thermodynamic data calculated with MD at $T=2000$ K. Dashed line are results at 2000 K from classical thermodynamics performed in FactSage [12]. Shaded grey zone correspond to the meta-stability zone of the liquid at 2000K.

ADP model are lower than 12 but significantly higher than the AIMD prediction (i.e. 9.6). Wang et al. [44] reported that the coordination number of $\text{Al}_{80}\text{Cu}_{20}$ melts increased by decreasing temperature, up to 11 at 1000K. This behavior has also been experimentally observed in $\text{Al}_{60}\text{Cu}_{40}$ melts, with values of 11.26 and 11.50 at 1323K and 973K respectively [203]. Important deviations are observed in the partial RDF for the Al-Cu pair (Figure 5.9b) for most MD simulations compared to AIMD calculations; except for the one with the MEAM potential developed in this work (green line), which shows the best accuracy.

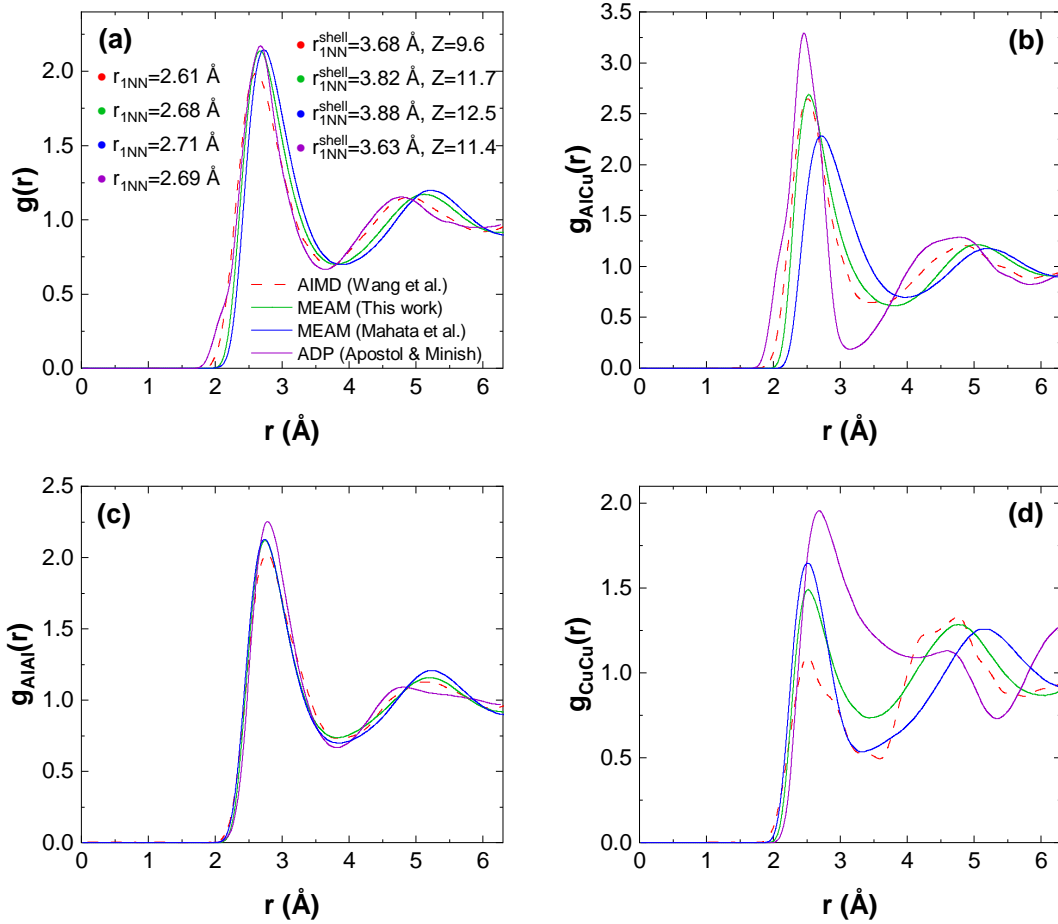


Figure 5.9 Calculated total (a), and partial Al-Cu (b), Al-Al (c) and Cu-Cu (d) radial distribution functions for liquid $\text{Al}_{80}\text{Cu}_{20}$ at 1818 K. Results from different classical MD models are compared to AIMD data. The first nearest neighbor distance (r_{1NN}), the shell of the first nearest neighbors (r_{1NN}^{shell}), and the total coordination number (Z) are indicated.

5.5.4 Potential transferability for the energetic description of isotropic and anisotropic solids

Al-Cu system

Solidification processes imply that solid particles will start to nucleate as the temperature is lowered below a specific value. Interatomic potentials should also be able to adequately describe solid solutions. Modeling of solid compounds within the Al-Cu system has been compared with three interatomic potentials, the AlCu₃-L1₂ MEAM potential of this work, the MEAM potential of Mahata et al. [42] and the ADP from Apostol & Mishin [43] (Table 5.5). Note that numerical data obtained from the MEAM potential developed by Mahata et al. [42] were directly taken from their published article. Unfortunately, we were not able to reproduce these values in our MD simulations using their provided interatomic potential file. For the isotropic Cu-rich L1₂ compound, the MEAM potential provided a better description than the ADP when compared to the DFT prediction. The opposite was observed for the Al-rich L1₂ structure. For the cubic AlCu-B2, both MEAM potentials overestimated the energetics of this phase, and the ADP showed the best accuracy. None of the three potentials is able to reproduce the entire set of phases, the predicting capability of EMD potentials is, therefore, dependent on the formalism employed during potential parametrization.

Table 5.5 Calculated enthalpy of formation (eV/atom) for Al-Cu metastable compounds. Results are compared to other MD models and first-principle calculations.

Formula	Structure	MEAM (this work)	MEAM [42]	ADP [43]	DFT
Al ₃ Cu	L1 ₂	-0.152	-0.180	0.100	-0.037 [11]
Al ₃ Cu ₂	D5 ₁₉	-0.182	-0.299	-0.342	-0.164 [204]
AlCu	B2	-0.317	-0.435	-0.635	-0.139 [11]
AlCu	B1	0.421	-0.205	-0.079	...
AlCu	“40” (NbP)	0.150	-0.016	-0.117	-0.191 [205]
AlCu	B32	-0.191	-0.009	-0.085	0.024 [205]
Al ₄ Cu ₉	D8 ₃	-0.139	-0.136	-0.331	-0.215 [43]
AlCu ₃	L1 ₂	-0.143	-0.179	-0.162	-0.181 [11]
AlCu ₃	A15	-0.070	-0.141	-0.196	...
AlCu ₃	D0 ₂₂	-0.142	-0.185	-0.226	-0.185 [206]

Al-Cr system

Enthalpy of formation at 0 K of Al-Cr solid compounds using the MEAM potential developed in this work are compared to DFT calculations available in the literature in Table 5.6. Energetic description of compounds was also compared to MD predictions using the FS po-

tential from Lui et al. [20]. The MEAM potential was able to provide a better energetic description of the AlCr_2 and Al_3Cr compounds. However, the crystal structure of $\text{Al}_{45}\text{Cr}_7$ and Al_8Cr_5 changed during the volume optimization (energy minimization) when using the MEAM formalism. FS potential considerably overestimates the formation energies of all solid compounds compared to DFT.

Table 5.6 Enthalpy of formation of different Al-Cr solid compounds at 0K compared with first-principle calculations and MD simulations. Formation energies are reported in eV/atom.

Formula	Space group	MEAM (this work)	FS [20]	DFT [11]
AlCr_2	I4/mmm	-0.120	-0.634	-0.122
Al_3Cr	I4/mmm	-0.097	-0.534	-0.140
$\text{Al}_{45}\text{Cr}_7$	C2/m	Crystal structure changes	-0.285	-0.117
Al_8Cr_5	R3m	Crystal structure changes	-0.435	-0.054

Al-Zr-Ti system

Modeling of different Al-Zr-Ti solid compounds using the ternary MEAM interatomic potential of this work (Table 5.3) is presented in Table 5.7. Overall, this potential shows a good predicting capability for binary and ternary compounds of this ternary system.

Table 5.7 Enthalpy of formation of different solid compounds within the Al-Zr-Ti system compared with first-principle calculations. Formation energies are reported in eV/atom.

Formula	Space group	MEAM (this work)	DFT [11]
TiAl	$\text{Pm}\bar{3}\text{m}$	-0.260	-0.265
Al_3Ti	I4/mmm	-0.273	-0.398
ZrTi_2	P6mmm	0.032	0.033
Zr_3Al	$\text{Pm}\bar{3}\text{m}$	-0.296	-0.302
Al_3Zr	I4/mmm	-0.340	-0.487
Zr_2TiAl	$\text{Fm}\bar{3}\text{m}$	-0.223	-0.160
ZrTi_2Al	Amm2	-0.333	-0.238

5.5.5 MD simulations of the crystallization of pure aluminum

The next step after validating the transferability of the interatomic potentials developed in this work was to apply them for the description of solidification processes. We started with the exploration of the solidification of a pure element which theoretically occurs at a specific temperature for some imposed pressure. The following thermal program was defined to melt, equilibrate and solidify the initially perfect Al-FCC supercell containing 200 000 atoms: equilibration into the NVT ensemble at 2.5 K for 0.5 ns, NPT heating at 1.66 K/s, NVT equilibration at 2000K during 0.5 ns followed by 0.5 ns of NPT modeling at the same temperature. Cooling was executed at -1K/ps. Finally, systems were equilibrated at 300K for 2ns. Crystallization results for pure aluminum are presented in Figure 5.10. The evolution of the temperature as a function of the simulation time is represented by the red line for the MD simulations performed using the Finnis and Sinclair (FS) potential [20] while the blue line provides the results with the MEAM potential developed in this work. Screenshots of the simulation supercells showing only FCC-oriented atoms are presented for specific simulation steps. This provides a visual appreciation of the melting and solidification mechanisms during the programmed thermal treatment. Melting of the pure and perfectly ordered FCC aluminum supercell using the FS potential occurred at around 700 K, which is 233 K less than the experimental value. Melting with the MEAM potential took place at around 1150 K. A higher melting temperature was expected because the initial configuration was a perfectly ordered FCC supercell without any defects. Since vacancies, dislocations, and grain boundaries are not considered, a higher amount of energy is required to overcome the perfect-lattice energy barrier for its mechanical melting. In other words, supplementary thermal energy is needed to induce the breaking of the long-range order symmetry of a crystal with no defects. Mechanical melting is related to elastic stability criteria for cubic systems, it occurs when the spinodal, shear or Born criteria are breached, i.e., $(C_{11} + 2C_{12} > 0)$, $(C_{44} > 0)$ and $(C_{11} - C_{12} > 0)$ respectively with C_{ij} being the elastic constant tensors [207]. In MD, there exist several methods to properly predict the fusion temperature, such as the Pseudo-Supercritical Path (PSCP) approach, interface-based techniques, and the voids method [208]. Even though the accurate melting description is out of the scope of this work, it can be observed that the FS potential is not suitable for this type of simulations since the melting point from a perfect FCC lattice is already lower than the experimental value.

The cooling process of the liquid system can be observed between 2.3 ns and 4 ns in Figure 5.10. Simulation results show that undercooled liquid modeled with the MEAM potential was able to crystallize into the α -FCC at around 3.95 ns. A deviation from the perfect linear

temperature profile which was programmed in the MD simulation is observed at around 4 ns. This temperature peak is associated with the release of latent energy caused by solidification. For the molten aluminum super-cell described by the FS-potential, an additional relaxation at 300 K after cooling (>4 ns) was needed in order to germinate the FCC-matrix (i.e. to form stable FCC-cluster within the liquid). Simulations cells at 6 ns correspond to the final configurations of the systems at 300 K. Empty spaces stand for atoms with a local ordering different from the FCC. The final crystal obtained with the FS potential accounted for 32.4% of FCC-oriented atoms and 59.5% of HCP. Conversely, the MEAM potential exhibited a more coherent crystallization with 82% of FCC and only 14.9% of HCP. The coexistence of both the FCC and the metastable HCP phases is commonly found in MD simulations for aluminum [117]. These structures actually share several characteristics: 1) they have the same atomic packing factor of 74%, they present similar interstitial sites, and 3) they both have 12 first nearest neighbors. Papanikolaou et al. [121] evaluated the effect of the cooling rate from 0.5 K/ps to 12 K/ps on the local structure of pure Al. They found that the proportions of FCC and HCP are dependent on the cooling rates. An FCC/HCP mixture is promoted at low cooling rates, and this ordering is less favored as the cooling rate is increased. Here, the cooling rate was 1K/ps for both samples; hence, the proportion of HCP ordering upon solidification is rather related to the impact of the potential parametrization. A detailed description of the local ordering during the simulations is presented in Figure 5.11. Independently from the potential used in each simulation, there is a clear relationship between the icosahedral ordering (yellow lines in Figure 5.11) and the FCC-oriented atoms (green lines) before and after crystallization. The icosahedral ordering consists of 12 atoms arranged around a central atom in the core of an icosahedron (Figure 5.12). It was proposed by Frank [140] to explain the energy minimization associated with local atomic arrangement during undercooling. As such, the maximum in the icosahedral fraction curve defines the maximum undercooling by icosahedral-related constraints. Nuclei for FCC germination may start forming at this stage. However, additional undercooling is required for appropriate nuclei conditions so that they do not dissolve into the liquid. In such a manner, they can act as germination sites of the α -phase. Nucleation of solid particles in metallic melts can be described by Arrhenius-type relationships [209]. Intrinsically, the frequency factor of the Arrhenius distribution is detrimentally affected in MD due to the small time scale, which explains why large undercooling is required in this type of atomistic simulation.

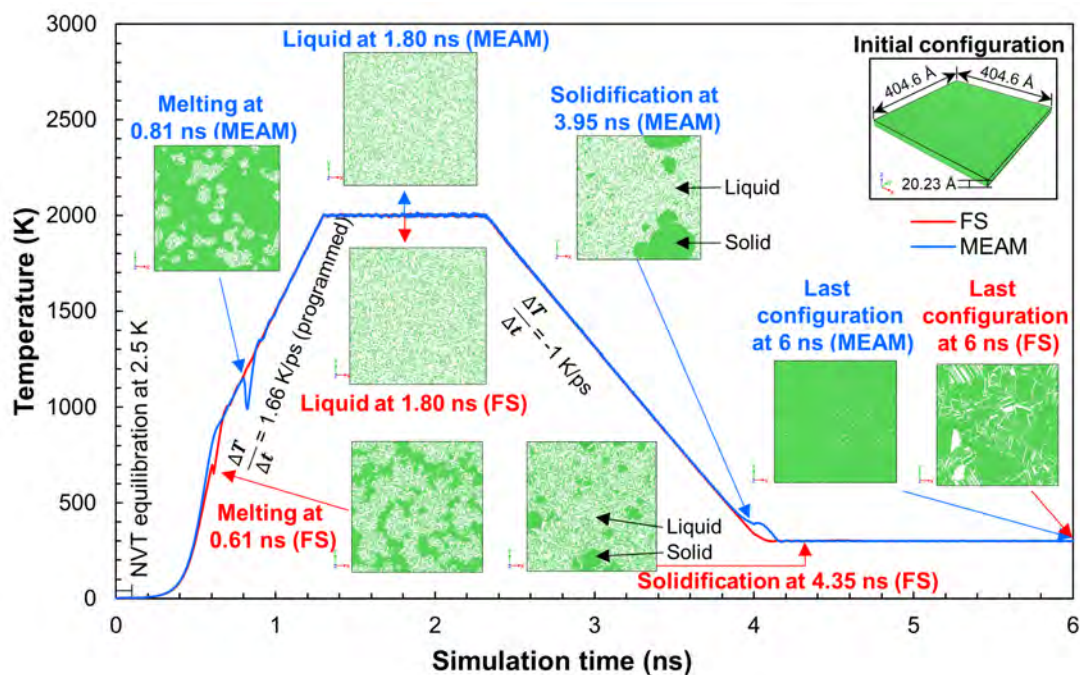


Figure 5.10 Scheme for time versus temperature during the classical MD simulation of melting/cooling of pure aluminum using the FS and MEAM potentials. Snapshots of simulated microstructures at specific simulation times are reported. Only FCC-oriented atoms are presented in the simulation boxes. Systems were first equilibrated into the NVT ensemble at 2.5 K for 0.5 ns. NPT heating at 1.66 K/s was subsequently imposed. Then, NVT equilibration was carried at 2000K during 0.5 ns followed by 0.5 ns of NPT modeling at the same temperature. Cooling was executed at -1K/ps. Finally, systems were equilibrated at 300K.

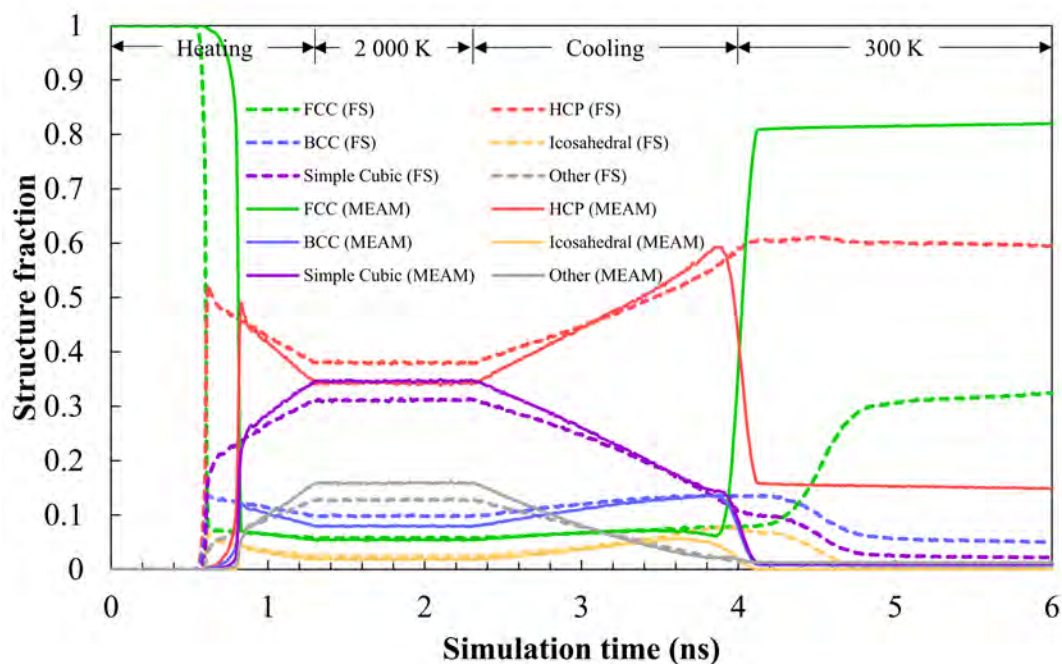


Figure 5.11 Time-temperature evolution of the local ordering in solid/liquid aluminum, calculated via the Polyhedral Template Matching method [8,26]. Calculated values with the MEAM potential (solid lines) in comparison with that obtained with the FS interatomic potential [20] (dashed lines).

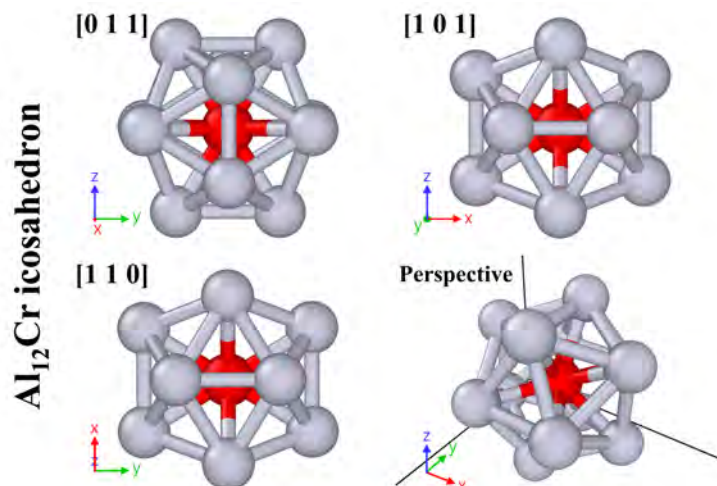


Figure 5.12 Different perspectives of an Al_{12}Cr icosahedral cluster equilibrated at 0K (Al is in grey, Cr is in red).

Figure 5.13 shows the graphical correlation between the icosahedral-oriented atoms (yellow) and FCC ordering (green) for the simulation of pure aluminum using the FS potential. Icosahedral orientation is rapidly rearranged into the FCC matrix of growing grains. By the end of solidification, only a minor icosahedral ordering of atoms is observed at the grain boundaries. Cassada & Poon [210] reported that the icosahedral ordering was promoted at the grain boundaries of Al-Mg-Zn, Al-Mg-Cu, Al-Li-Zn, and Al-Li-Cu alloys during annealing. Minimum in the icosahedral ordering curve (Figure 5.11) suggests the end of solidification.

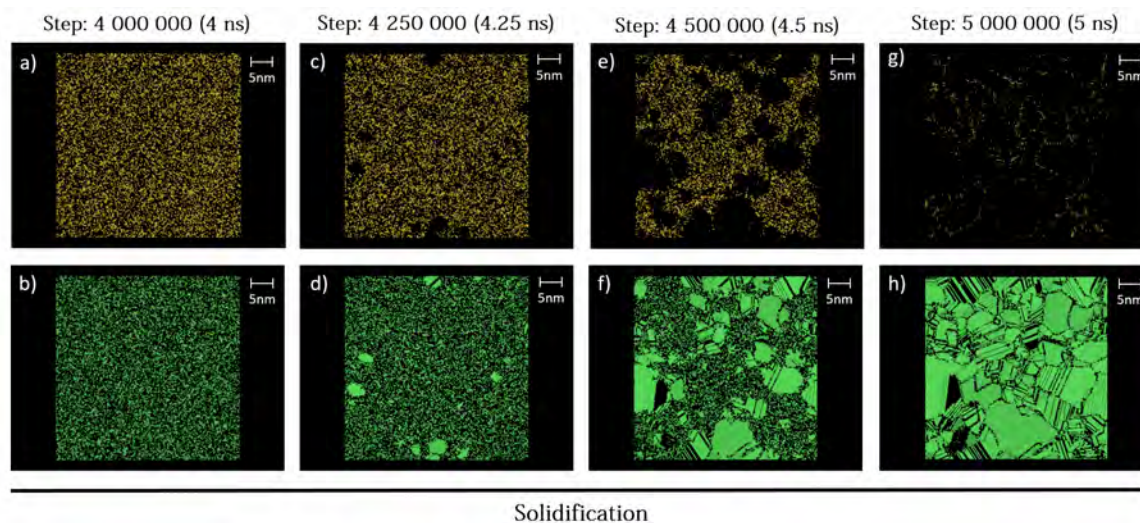


Figure 5.13 Simulated partial local ordering via FS potential at specific simulation steps. Icosahedral-oriented atoms are presented in yellow and FCC in green.

5.5.6 Crystallization of model Al-Cr alloys by icosahedral-enhanced nucleation

The addition of alloying elements to a pure metallic system will have a direct impact on its melting and solidification behavior. This section considers the effect of Cr on the nucleation of model Al-Cr alloys. It also shows the impact of the interatomic potential on the solidification behavior of this system. A similar heat program to the one used for the pure aluminum study was implemented here as it can be seen in Figure 5.10. The difference lies in the composition of the initial simulation supercells. Herein, Cr atoms were randomly distributed into the perfect-FCC lattice at different atomic concentrations of Cr (Figure 5.14). These initial configurations were inspired by the quasi-two-dimensional cells proposed in the literature [9, 10]. They are particularly convenient because they approximate a simulation sample at the center of a large-scale cubic cell but with a lower computational cost [10]. According to the Al-Cr equilibrium phase diagram calculated using the FTlite database of FactSage [12] which is presented in Figure 5.15, the α -matrix is the primary phase upon solidification of Al-

Cr alloys up to 0.15 at.% of Cr. Above this composition, $\text{Al}_{13}\text{Cr}_2$ is the first intermetallic to precipitate up to 0.95 at.%. Lastly, $\text{Al}_{11}\text{Cr}_2$ is the primary phase for Al-Cr alloys containing 7 at.% of Cr.

Local chemical ordering results for the last MD configuration of each model binary Al-Cr alloys are displayed in Figure 5.16. The local ordering presented in this figure was evaluated with the Common-Neighbor Analysis (CNA) and Polyhedral Template Matching (PTM) [8] of OVITO [26]. Firstly, it can be seen that the MEAM potential outperforms the FS potential for all the compositions as it leads to a much more coherent solidification of nano α -FCC grains and minor HCP ordering due to twinning. The FS potential exhibits considerable fraction of HCP-oriented nano-zones in equilibrium with the FCC-phase for 0, 0.1, 0.5, 0.75, and 1 at.%. A metallic glass was obtained for 7at.% of Cr with the FS modeling. As anticipated by the nature of the atomic scale MD simulations, the primary intermetallics (which should have formed as predicted from classical thermodynamics in Figure 5.15) were not able to nucleate. This is mainly caused by the high cooling rates which are typically imposed in MD simulations. As a result, the FCC was the primary phase during the solidification process of all our MD simulations using the MEAM potential, even with a high amount of Cr. This is a result of the out-of-equilibrium conditions imposed by the simulations. Strategies to overcome this problem when studying solidification include the interface method where a liquid supercell is coupled to a solid interface of the primary phase [123]. Aside from that, classical molecular dynamics performed in the NPT and NVT ensembles solely rely on enthalpy contributions to module the energetics and dynamics of the system. As such, entropy effects, which play an important energetic role, especially at high temperatures, are not integrated. Apart from this important limitation, the preference of atoms in a liquid to cluster/aggregate and eventually precipitate to form solid intermetallic nuclei is strongly dependent on the electronic structure of the individual atoms. This means that the electronic structure should be meticulously described in order to simulate the formation of intermetallic phases having specific crystallography. Current interatomic potential formalisms for MD are based on simplifications of the effect of the electronic structure of individual atoms on the energetics of metallic systems. This also restricts the exploration of the precipitation of solid phases different from the FCC matrix in classical MD simulations.

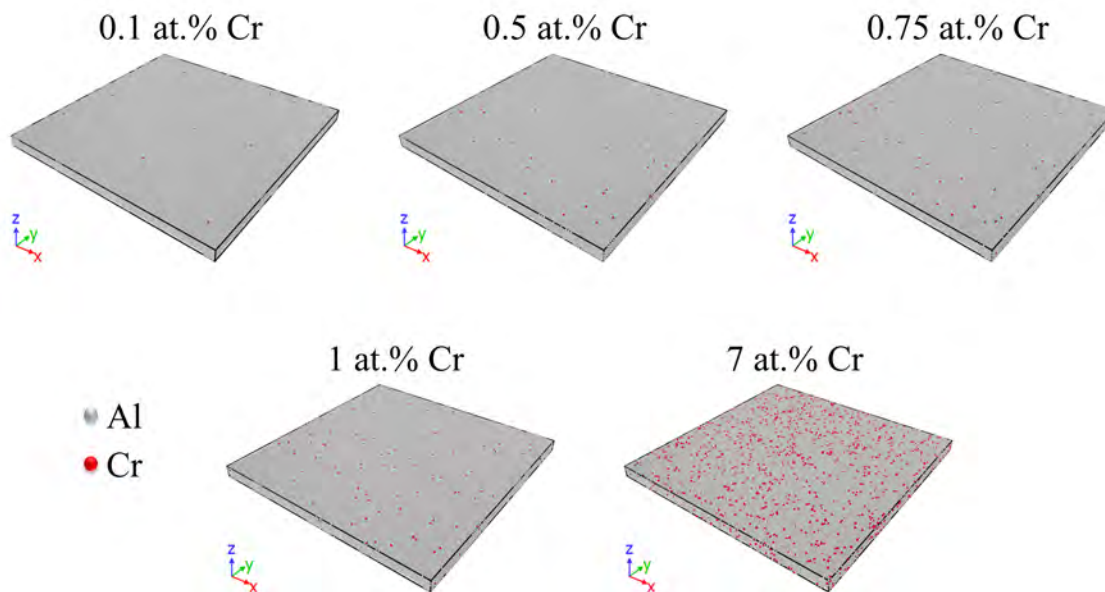


Figure 5.14 Representation of the initial configurations for the simulations of Al-Cr alloys (Al atoms are presented in grey, Cr atoms are in red). Cr atoms were randomly distributed across an FCC simulation box followed by a volume minimization.

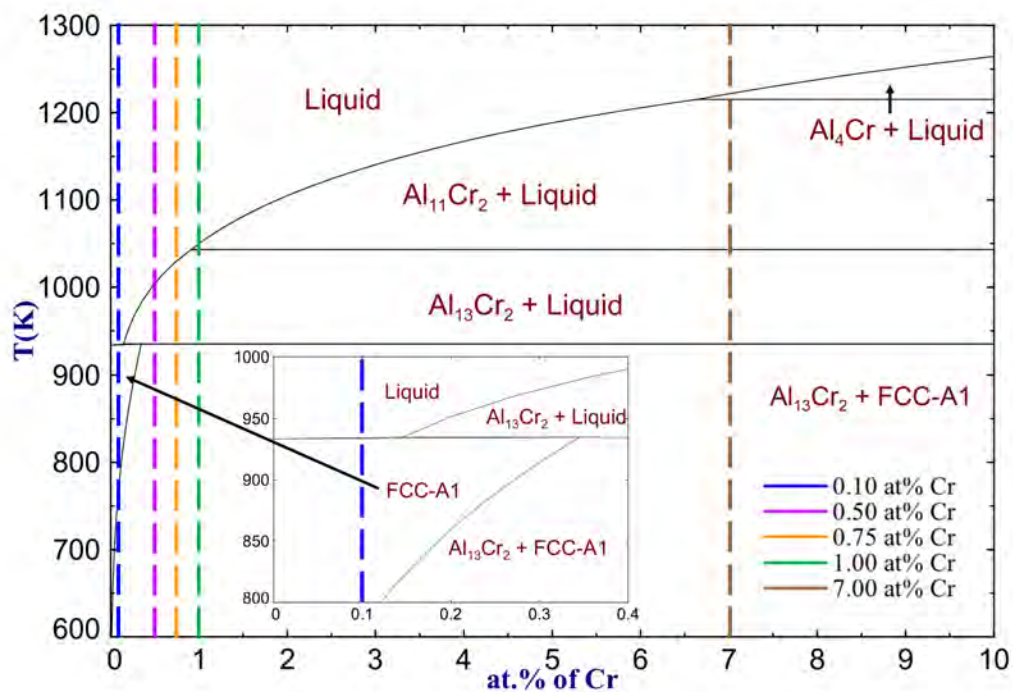


Figure 5.15 Computed Al-Cr phase diagram using the FTlite database. The different compositions studied in this work are indicated with dashed lines.

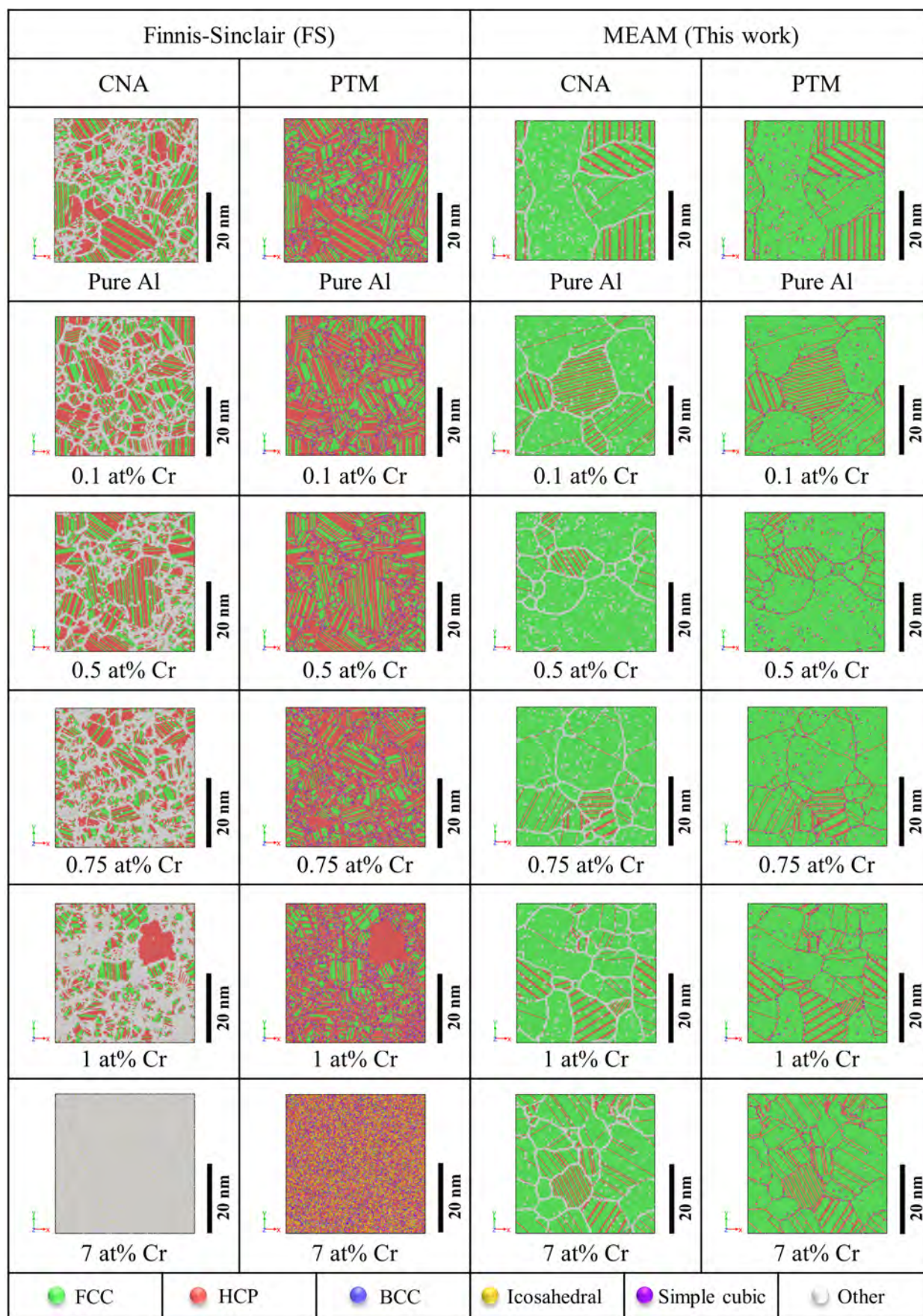


Figure 5.16 Simulated microstructures for Al-Cr alloys at different compositions. The local ordering was determined via Common-Neighbor Analysis (CNA) and Polyhedral Template Matching (PTM).

Curves of temperature versus time for the different Al-Cr alloys using the MEAM potential are reported in Figure 5.17. Peaks at the end of the cooling curve correspond to the effect of the latent energy released from crystallization. Each stationary point in these curves indicates the effective nucleation of the FCC-phase, and thus, the beginning of latent energy release. The local maximum temperature after the stationary point shows an increase in the overall temperature of the supercell due to the phase transformation. These solidification peaks appear earlier in the solidification process as the amount of Cr in the alloy is increased. This implies that the addition of Cr into aluminum melts promotes the germination of the FCC phase with less undercooling when compared to pure aluminum. This is in agreement with the Icosahedral quasicrystal-enhanced nucleation theory for the germination of the FCC phase [211]. Kurtuldu et al. [7] achieved grain refinement by this mechanism in an Al-Zn-Cr alloy with only 1000 ppm of Cr. The peaks at around 1 ns upon heating corresponds to the melting. More heating is needed as more Cr is present in the solid solution. This is a typical behavior of the peritectic Al-Cr system, in which the liquidus increases by increasing the amount of Cr in the alloy.

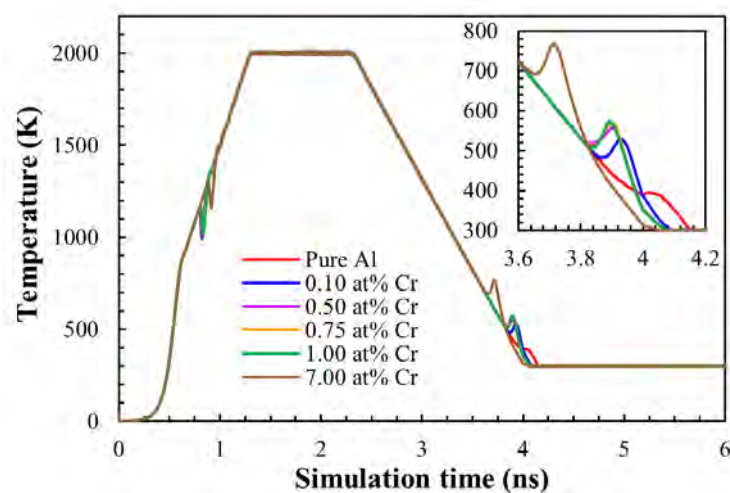


Figure 5.17 Simulated temperature vs time for the different Al-Cr alloys. The inside figure shows the zoom of temperature perturbations during the cooling, which corresponds to the latent energy release of solidification.

The evolution of the icosahedral fraction during the MD simulations performed with the MEAM potential is presented at the top of Figure 5.18. The slope between the maximal (>3.5 ns) and minimal (<4.1 ns) values in the icosahedral ordering provides information about the kinetics of solidification. Pure Al had the least pronounced slope compared to Al-Cr alloys. This implies that solidification (nucleation + grain growth) took longer to be completed for this non-Cr-doped system. A steeper slope is obtained by increasing the amount of Cr in the

Al-Cr alloys. This means that nuclei are more effective for the germination of the α -phase as more Cr is added into the Al-Cr melts. The MD simulation with the highest amount of Cr (7%at.) solidified faster than the rest of the molten alloys. Note that this behavior is exclusive of the Al-Cr potential developed with the MEAM formalism; such a trend is not observed for the MD simulations performed with the FS potential (bottom of Figure 5.18). Instead, solidification is slowed down when increasing the amount of Cr. Therefore, more time is required to achieve a critical amount of icosahedral fraction. Moreover, for the simulation supercell containing 7 at% of Cr, a metallic glass was obtained. This is a result of the largely overestimated strength of the Al-Cr interactions using the FS interatomic potential as presented in sections 5.5.2 and 5.5.4. This glass transition occurs somewhere between [1.5 : 7] at% of Cr according to our simulations. All these results clearly show that the energetic description of these Al-Cr supercells with the Al-Cr FS interatomic potential provides a completely different solidification behavior to the MD simulations performed with the MEAM potential. The use of the MEAM potential led to a consistent description of the solidification, i.e. where the icosahedral-enhanced germination of the FCC phase in Al-Cr melts occurs [7]. Therefore, an accurate description of the Al-Cr interatomic distance along with the prediction of its precise energetic strength are key ingredients to ensure a good transferability of the potential to describe complex phase transition phenomena such as bulk crystallization.

Figure 5.19 shows the maximal icosahedral fraction achieved by all the Al-Cr melts prior to solidification for the simulations performed with the Al-Cr MEAM potential. Each value is related to the undercooling caused by icosahedral-related constraints. Pure Al reached a higher undercooling compared to all the other Al-Cr melts. This figure shows that the binary liquid solution with the highest concentration of Cr (7 at.%) exhibited the lowest undercooling. These values are higher than the stationary points presented in the cooling curves (Figure 5.17) for all the compositions. In this case, an extra undercooling is required so that nuclei become effective for the precipitation of the FCC-phase.

Figure 5.20 shows the overall time from the formation of the first nuclei (red points) to the end of solidification (black points). Pure aluminum displayed the longest time with 0.48 ns and the fastest solidification took place for the binary melt containing 7 at.% of Cr ($\Delta t = 0.16$ ns). While the time from effective germination of the FCC-phase (blue points) to the end of solidification (black points) is more or less equivalent for all the melts, the time for effective germination of the α -phase (from red to blue points) considerably changes from one composition to another. Nuclei in Al-7.at%Cr were more efficient for germination. More time for effective germination was needed as less Cr was present in the Al-Cr melts. Nucleation sites in pure Al were the least powerful resulting in a higher solidification time.

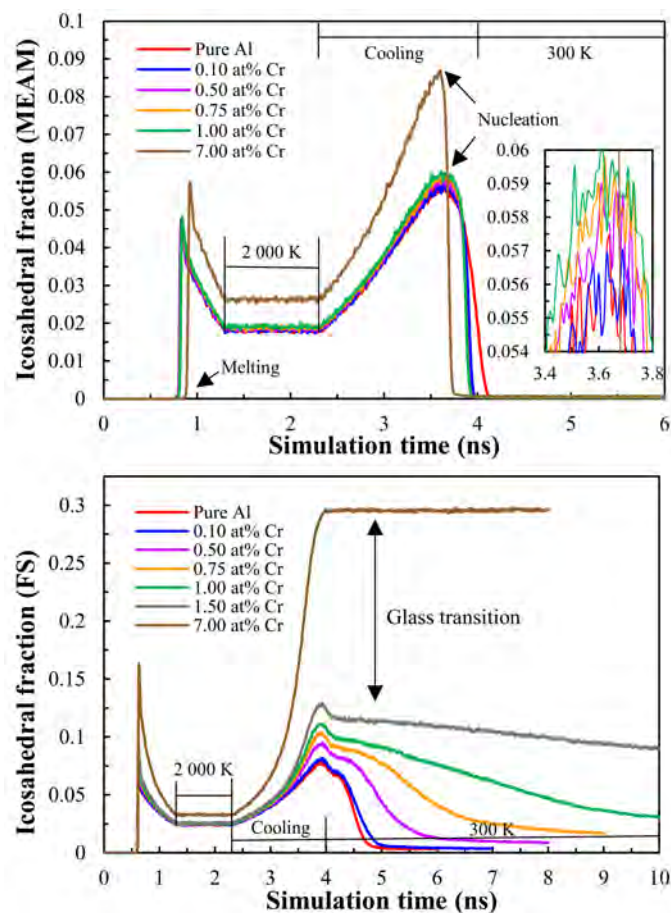


Figure 5.18 Evolution of the icosahedral fraction over simulation time for different Al-Cr alloys using the MEAM (top) and FS (bottom) potentials.

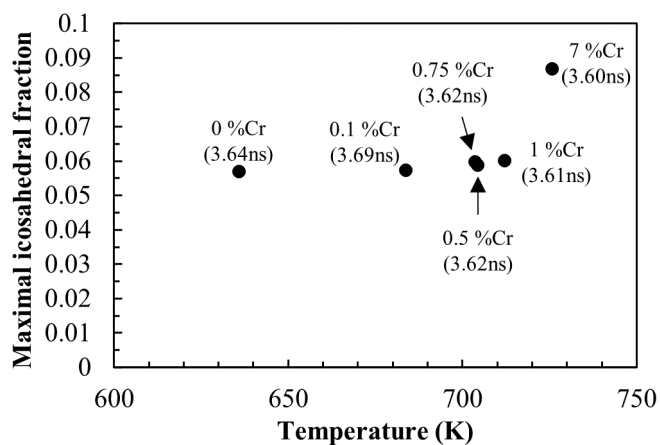


Figure 5.19 Maximum icosahedral-related undercooling in Al-Cr alloys.

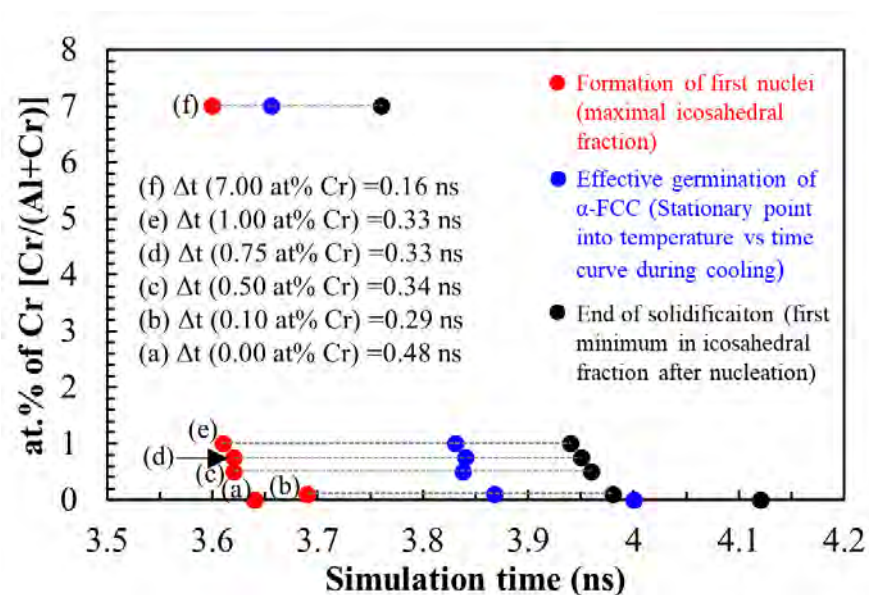


Figure 5.20 Solidification stages correlated with the icosahedral ordering and the stationary point in the cooling curves of Al-Cr alloys.

Total energy vs temperature for all the simulations performed with the MEAM potential is presented in Figure 5.21. For all the compositions, phase transformation was not isothermal. This deviation implies that energy release from solidification caused an increase in the temperature of the solid phase. The coexistence of solid and liquid phases occurred at lower temperatures for pure Al, because of the used undercooling for effective nucleation when compared to Al-Cr melts.

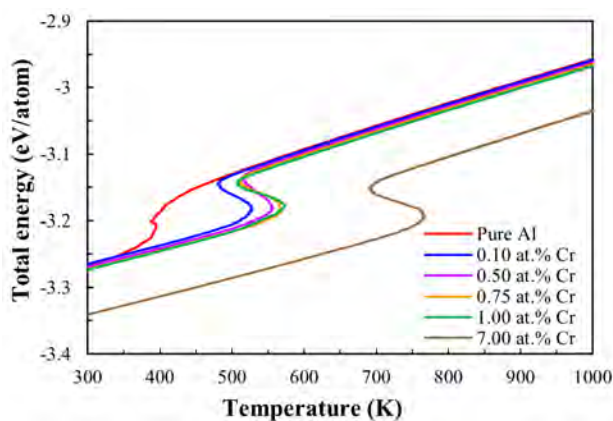


Figure 5.21 Total energy versus temperature of for the different Al-Cr simulations during cooling.

Lastly, a grain analysis for the last configuration (at 6 ns) of all MD simulation cells modeled with the MEAM potential (Figure 5.22) was computed using the grain segmentation algorithm reported by Vimal et al. [212]. Grain segmentation is compared to the Polyhedral Template Matching (PTM) results (shaded section in Figure 5.22). Explicitly, grain segmentation did not account for the twinning of coherent phases along the same grain. For this reason, a fourth column was added and corresponds to the twinning correction of coherent phases (FCC/HCP) belonging to the same grain. These were misleadingly identified as different grains by the grain segmentation algorithm. The third column of Figure 5.22 shows the number of grains as [corrected value accounting for twinning]/ [Total from grain segmentation algorithm]. Pure Al exhibited a smaller number of grains (4). Grain refinement was achieved for Al-Cr melts when compared to pure Al. Modeling of Al-Cr melts using the MEAM potentials was in agreement with the icosahedral-enhanced nucleation theory promoted by Cr, as experimentally reported by Kurtuldu et al. [7].

It is to be pointed out that all these equiaxed-like simulated nanostructures were obtained from extremely fast cooling rates. In industrial applications, solidification cooling rates are orders of magnitude smaller (even during powder atomization from melts or laser additive manufacturing) and would result in either dendritic or cellular structures at a much larger scale (typically the micron scale). Moreover, the heat extraction in our MD simulations was non-directional (pseudo-isothermal cooling) which is never the case in real applications. At best, such pseudo-isothermal cooling would apply locally. Nevertheless, these nanostructures are highly reminiscent of typical microstructures obtained from slowly solidified alloys. One potential explanation is the much smaller cooling power involved in our MD simulations compared to the one obtained in real solidification processes. In our simulations, we remove about $[1.4 \times 10^7 \text{ W}/(\text{m}^2\text{K}) - 3.31 \times 10^7 \text{ W}/(\text{m}^2\text{K})]$, which is significantly higher than the $[370 \text{ W}/(\text{m}^2\text{K}) - 1917 \text{ W}/(\text{m}^2\text{K})]$ interval in casting processes [213]. Equivalently, we can view this in terms of the number of atoms that are ordered per second upon solidification which is much greater in real-life applications than in our MD simulations. Further investigations are needed to determine the influence of these scaling factors from atomistic simulations to real-life conditions to understand how to transpose MD simulation results obtained with periodic boundary conditions to a larger scale.

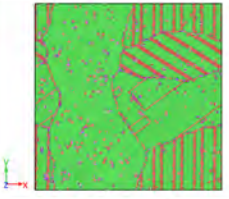


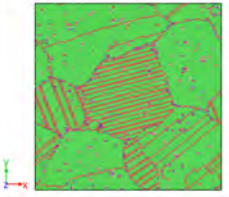
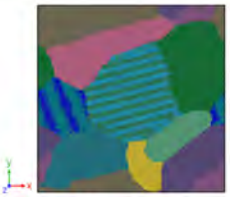
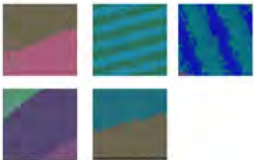
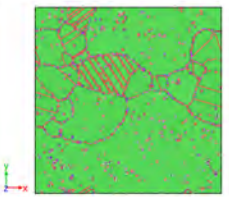
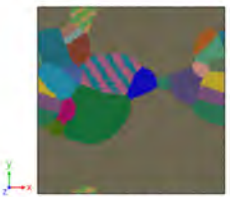
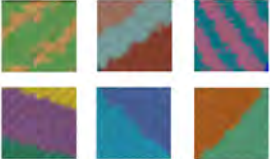
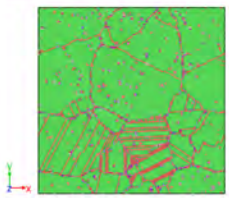

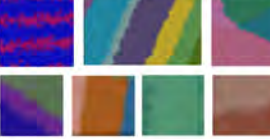
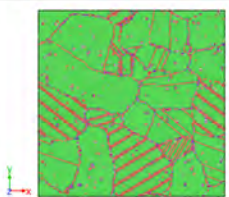

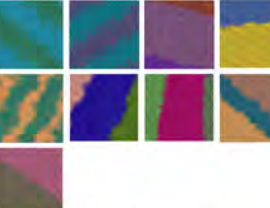
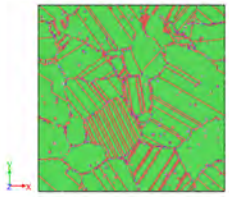
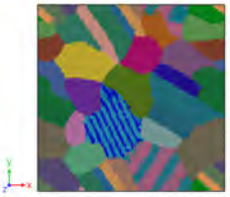
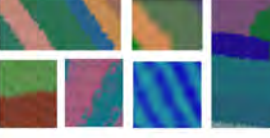






MEAM					
PTM	Grain segmentation	Count of grains	Twinning correction		
 Pure Al	 Pure Al	4/6 Pure Al	 Pure Al		
 0.1 at% Cr	 0.1 at% Cr	6/12 0.1 at% Cr	 0.1 at% Cr		
 0.5 at% Cr	 0.5 at% Cr	16/24 0.5 at% Cr	 0.5 at% Cr		
 0.75 at% Cr	 0.75 at% Cr	15/31 0.75 at% Cr	 0.75 at% Cr		
 1 at% Cr	 1 at% Cr	17/30 1 at% Cr	 1 at% Cr		
 7 at% Cr	 7 at% Cr	14/31 7 at% Cr	 7 at% Cr		
 FCC	 HCP	 BCC	 Icosahedral	 Simple cubic	 Other

Figure 5.22 Analysis of the local ordering via PTM analysis (first column) compared to the grain segmentation analysis for different Al-Cr alloys.

5.5.7 Crystallization of Al-Zr-Ti alloys

The last series of MD simulations we conducted in this work regarding solidification involved the presence of peritectic elements such as Zr and Ti in Al melts. Specific amounts of these two alloying elements are known to affect the nucleation of FCC grain during solidification via grain refiner mechanisms [45–48]. The objective of this section was to evaluate if classical MD simulations can provide useful insights about the effect of these elements on the solidification of aluminum. To do so, MD simulations for crystallization of Al-Zr-Ti alloys were performed as follows: a perfectly ordered Al-FCC simulation box of $100 \times 100 \times 5$ unit cells with 200 000 atoms was created (this corresponds to a volume of $404.6 \times 404.6 \times 20.23 \text{ \AA}^3$). Zr and Ti atoms were randomly distributed in this supercell structure to obtain two simulation boxes (Figure 5.23). A volume optimization (energy minimization) was then performed to equilibrate the initial structure prior to launching the thermal heating/cooling program. Sample 1 (S1) contains 0.11 wt% of Zr and 0.18 wt% of Ti. Sample 2 (S2) has 0.23 wt% of Zr and 1.2 wt% of Ti. According to the isoplethal section generated with the FTLite database of FactSage [12] (see Figure 5.24), these imposed compositions correspond to the precipitation of Al_3Zr as a primary phase in current phase diagrams for both alloys. Al_3Ti is a secondary phase for sample S2. Both MD simulation boxes were first heated at 1800°C . They were then equilibrated at 1800°C for 1 ns. After that, the cooling process took place at a rate of 1K/ps up to 800°C . A second equilibration at 800°C was performed during 1 ns. Additional cooling at 1K/ps took place until reaching 25°C . Finally, the systems were relaxed at 25°C .

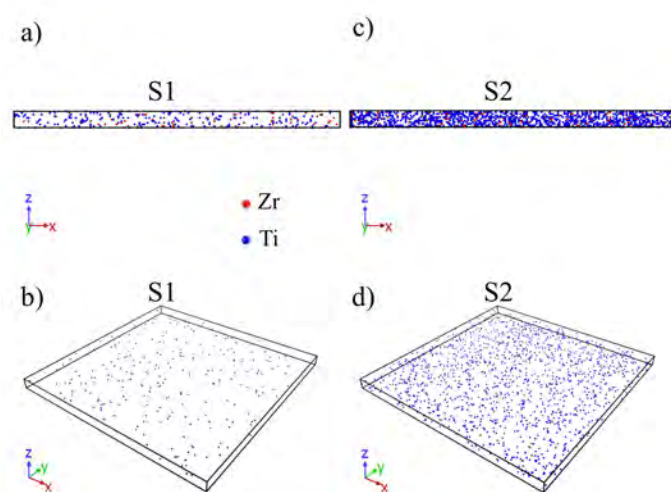


Figure 5.23 Initial configurations for two model aluminum alloys showing only Zr and Ti inside the Al-FCC. a) and b) correspond to Sample 1 (S1), which contains 0.11 wt% of Zr and 0.18 wt% of Ti. c) and d) stand for Sample 2 (S2), having 0.23 wt% of Zr and 1.2 wt% of Ti.

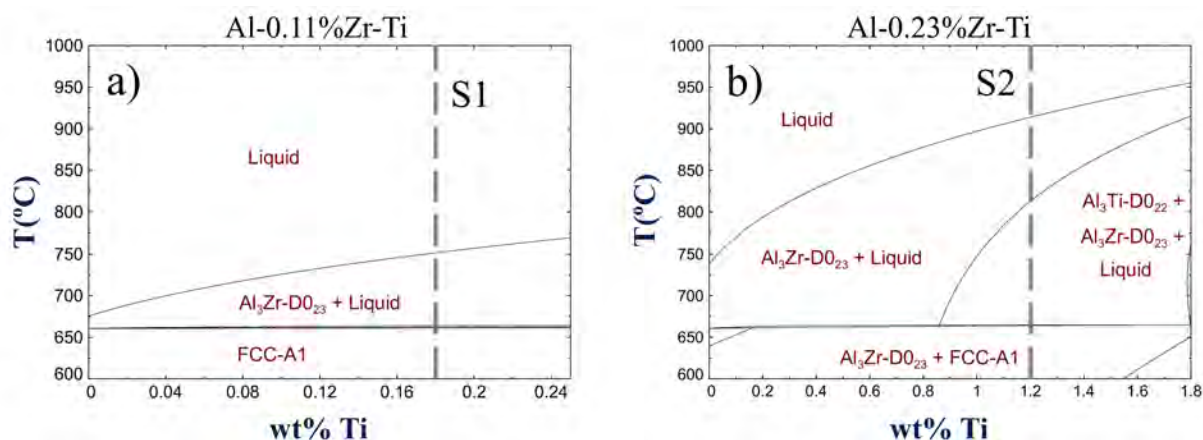


Figure 5.24 Phase diagrams generated with FactSage [12] showing the isoplethal section (gray dashed lines) for samples S1 (a) and S2 (b). Sample S1 contains 0.11 wt% of Zr and 0.18 wt% of Ti. Sample S2 has 0.23 wt% of Zr and 1.2 wt% of Ti.

The evolution of temperature over time for samples S1 and S2 is presented in Figure 5.25. The stationary point in the second cooling curves (from 800°C to 25°C) appeared earlier for sample S2. This implies that the effective nucleation occurred earlier for this composition. Nucleation sites in sample S1 were less efficient and an additional undercooling was required to solidify this molten alloy. The S2 supercell contains 6.7 times more Ti than S1. Germination of the α -phase enhanced by Ti is reported in the literature as the peritectic nucleation theory [45]. It states that the precipitation of Al_3Ti intermetallics occurred as the primary phase, followed by the germination of the FCC-phase through a peritectic reaction involving these Al_3Ti particles.

The evolution of the local atomic ordering for samples S1 and S2 is presented in Figure 5.26. It includes the analysis for FCC, HCP, and icosahedral ordering as they are the most representative ones during the solidification of these supercells. Germination of the FCC-phase (green) of simulation S2 occurred earlier than S1. Both ultimately resulted in an equivalent FCC/HCP crystal at the end of cooling. This structure did not significantly change during the final equilibration step at 25°C.

Supercell snapshots for both simulations showing the partial local ordering at 4.5ns, 4.6ns, and 6ns are displayed in Figure 5.27. For both MD simulations, there exists a spatial correlation between the FCC (green) and icosahedral (yellow) ordering. Icosahedral ordering disappears as the FCC phase solidifies. By the end of solidification, only a minor icosahedral ordering remains at the grain boundaries.

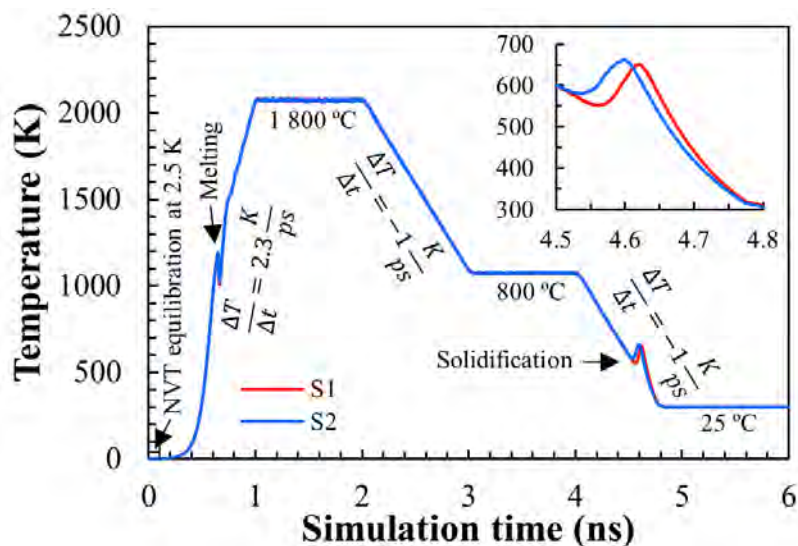


Figure 5.25 Simulation time vs temperature for samples S1 and S2 using the Al-Zr-Ti MEAM potential. Both simulations were first equilibrated into the NVT ensemble at 2.5 K for 0.1 ns. NPT heating at 2.3 K/s was subsequently imposed. Then, NPT equilibration was carried at 2073.15K during 1 ns. Cooling was executed at -1K/ps up to 1073.15 K. A second equilibration took place at 1073.15K during 1 ns follow by cooling at -1K/ps up to 298.15 K. Finally, systems were equilibrated at 298.15 K.

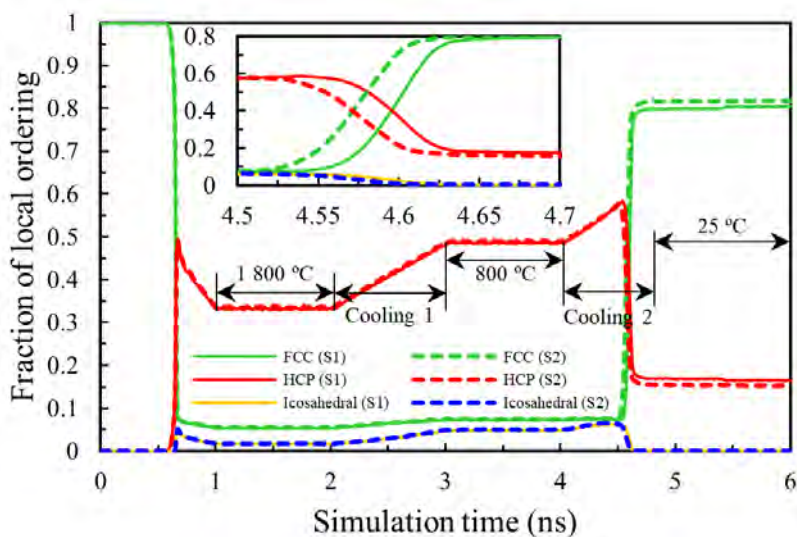


Figure 5.26 Simulation time versus partial local ordering in samples S1 and S2. FCC, HCP, and Icosahedral configurations were computed using the Polyhedral Template Matching (PTM) [8].

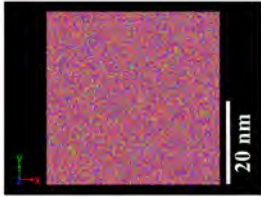
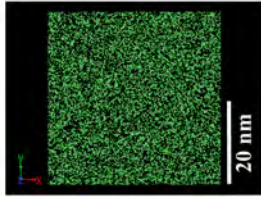
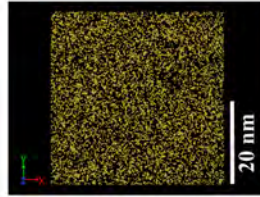
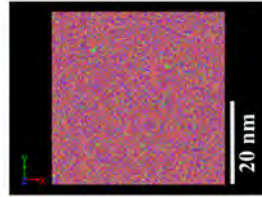
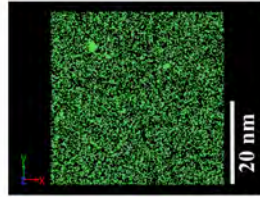
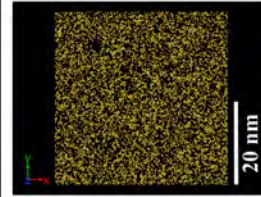
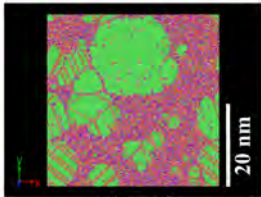
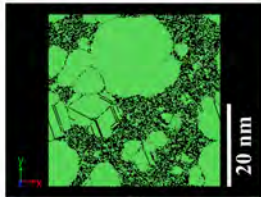
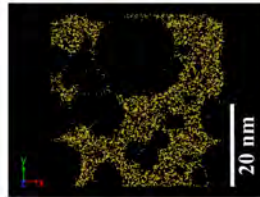
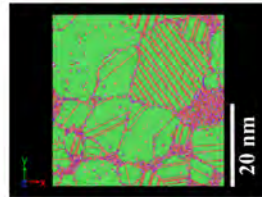
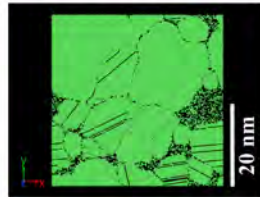

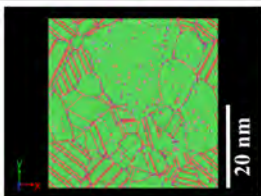
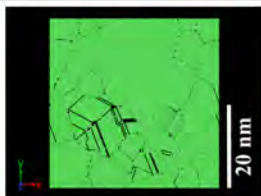

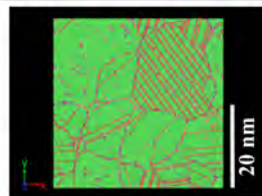
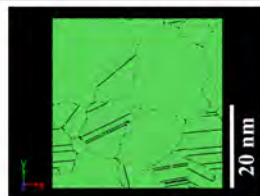
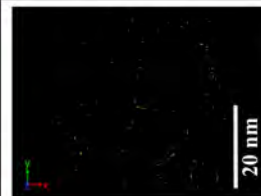
Simulation S1			Simulation S2		
All configurations	FCC	Icosahedral	All configurations	FCC	Icosahedral
 4.5 ns	 4.5 ns	 4.5 ns	 4.5 ns	 4.5 ns	 4.5 ns
 4.6 ns	 4.6 ns	 4.6 ns	 4.6 ns	 4.6 ns	 4.6 ns
 6 ns	 6 ns	 6 ns	 6 ns	 6 ns	 6 ns

Figure 5.27 Local ordering was computed with PTM for S1 and S2 simulation boxes at 4.5 ns, 4.6 ns, and 6 ns. FCC(green) and icosahedral (yellow) oriented atoms are presented independently. An additional picture showing the HCP (red) along with FCC and icosahedral ordering is provided.

The final orientation and distribution of Zr atoms for simulations S1 and S2 are shown in Figure 5.28a and Figure 5.28b respectively. It is observed that most Zr atoms have an FCC orientation which is confirmed by Figure 5.28e. Moreover, Zr atoms appear to be dispersed into the simulation cell. As such, the precipitation of Al_3Zr intermetallics is not observed in our MD simulations. In fact, the high cooling rates of our MD simulations trapped this peritectic element inside the α -matrix. Equivalent conclusions were obtained for Ti and the precipitation of Al_3Ti intermetallics. Both Zr and Ti supersaturated the α -Al phase due to the high cooling rates. A literature review on the possible heterogeneous nucleation in classical molecular dynamics shows that this mechanism has only been achieved by artificially seeding a liquid with solid embryos [122]. Fujinaga et al (2020) [123] successfully accomplished the germination of the α -FCC phase by artificial nucleation as well. In their study, they imposed $\text{Al}_3\text{Ti-D0}_{22}$ and $\text{Al}_3\text{Ti-L1}_2$ solids interfaces in contact with molten aluminum. Still, these methodologies are not useful for the prediction of primary phases.

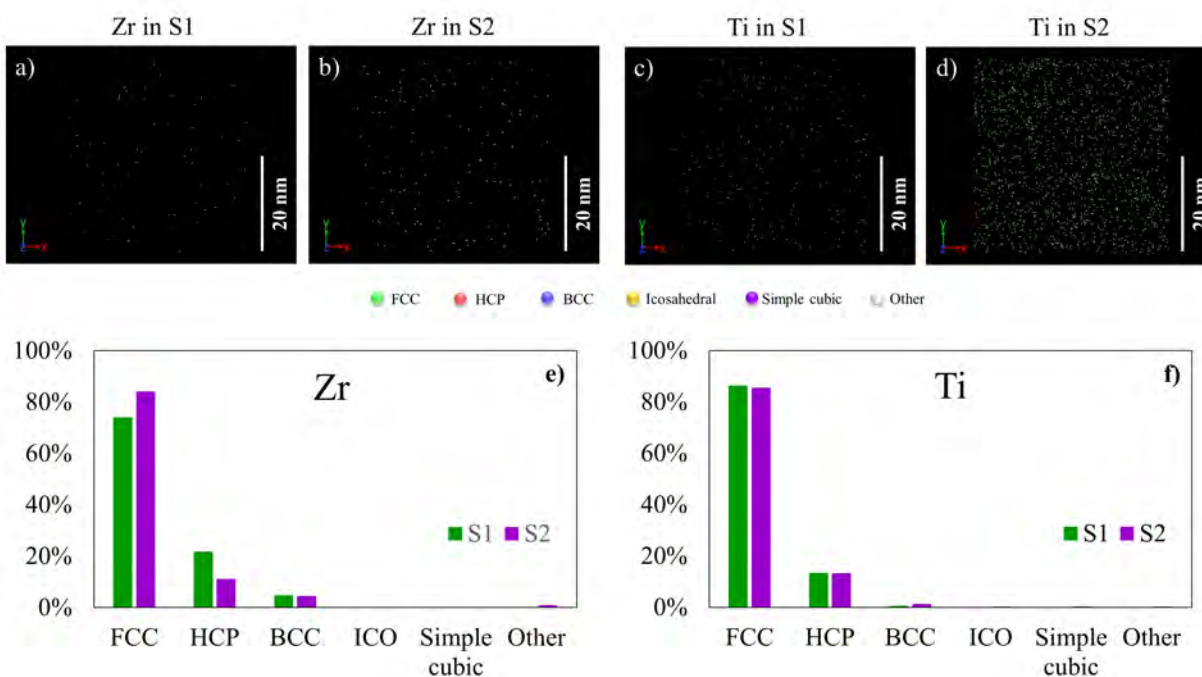


Figure 5.28 a), b) c) and d) show the final orientation of Zr and Ti atoms in the last simulation cells (6ns) for simulations S1 and S2. e) and f) show the percentage of the local ordering of Zr and Ti atoms respectively.

5.5.8 Modelling of pseudo-binary solid solutions: $\text{Al}_3(\text{Zr},\text{Ti})\text{-D0}_{23}$ and $\text{Al}_3(\text{Ti},\text{Zr})\text{-D0}_{22}$

Intermetallics are commonly found as partially ordered multicomponent solid solutions in typical solidified aluminum alloy microstructures. For example, Al_3Zr -based intermetallics have been identified as nucleant particles of the FCC-phase of aluminum alloys. More precisely, they have been found at the core of α -grains within the 6082 Aluminum Alloy [47]. Al_3Zr intermetallics reported in that study contained important amounts of Ti which substituted Zr in specific sub-lattices. This partially ordered structure is a result of atomic substitutions of specific elements of their perfectly ordered structure by either alloying elements or impurities. This substitution can be energetically described by thermodynamic models such as the compound energy formalism [214]. In the context of a solidification process, such partial substitutions in a given primary phase can lead to stabilization entropy effects [215] that may impact the nucleation process. This section explores the structural and energetic behavior of $\text{Al}_3\text{Zr-D0}_{23}$ and $\text{Al}_3\text{Ti-D0}_{22}$ intermetallics that experience atomic substitution within their crystal structure. These two intermetallic phases were specifically chosen as they are of critical importance when studying the solidification process and resulting mechanical behaviour of various aluminum alloys. More specifically, elastic properties and lattice parameters of both $\text{Al}_3\text{Zr-D0}_{22}$ and $\text{Al}_3\text{Ti-D0}_{23}$ tetragonal phases evaluated at 0K are presented in Table 5.8. The description of both perfect crystal structures obtained from the MEAM force field models used in this work are in reasonable agreement with the DFT calculations reported in the literature. Elastic constants and lattice parameters for the cubic the Zr_2TiAl (Fm3m) compound were also computed (Table 5.8). The interatomic potentials used in our work provide an adequate description of this isotropic ternary compound when compared to DFT results found in the literature [216]. Based on these results, it is assumed that the pseudo-binary solid solutions modeled with these MEAM force field models should provide precise energetic results.

Simulations supercells of 128 atoms were used for the exploration of the energetic behaviour of the $\text{Al}_3(\text{Zr}_x,\text{Ti}_{1-x})\text{-D0}_{23}$ solid solution while 256 atoms were used for the $\text{Al}_3(\text{Ti}_x,\text{Zr}_{1-x})\text{-D0}_{22}$ structure. The a and c lattice parameters, as well as the enthalpy of formation of both tetragonal solid solutions, were computed with EMD and DFT calculations via 0K volume minimization (Figure 5.29 and Figure 5.30). It is to be noted that the initial atomic configurations accounting for Ti and Zr substitution were exactly the same for both MD and DFT simulations. Lattice constants were compared to the one of pure Al FCC from DFT calculations at 0K [11] in all our figures. Figure 5.29a shows the evolution of the a parameter in the D0_{23} -phase as Zr is substituted by Ti. This cell parameter decreases as Zr

Table 5.8 Lattice parameters and elastic constant of $\text{Al}_3\text{Zr-D0}_{23}$, $\text{Al}_3\text{Ti-D0}_{22}$ and Zr_2TiAl compounds by MD simulations compared to DFT calculations.

	$\text{Al}_3\text{Zr-D0}_{23}$		$\text{Al}_3\text{Ti-D0}_{22}$		Zr_2TiAl	
	MEAM	DFT	MEAM	DFT	MEAM	DFT
	(this work)	[11, 217]	(this work)	[11, 217]	(this work)	[216]
Lattice parameter "a" (Å)	4.05	4.02	3.89	3.84	6.72	6.81
Lattice parameter "c" (Å)	17.46	17.24	8.71	8.60
B (GPa)	96.20	103	124	92	108.74	101.249
C_{11} (GPa)	145.01	209	145.81	196	145.81	119.414
C_{12} (GPa)	82.76	64	143.28	87	90.20	92.167
C_{13} (GPa)	71.16	45	80.67	45	90.20	...
C_{44} (GPa)	39.65	81	52.58	93	84.77	64.186
Poisson ratio	0.35	0.18	0.38	0.18	0.38	0.31

atoms are substituted. This is consistent with the different atomic radii of Zr and Ti. The same behavior is observed for the c lattice parameter (Figure 5.29b). Our results show that the a parameter of the perfectly ordered D0_{23} structure is virtually the same as the lattice parameter of the pure FCC aluminum matrix. This figure also shows that the c lattice parameter is more than 4 times bigger than the lattice parameter of pure FCC aluminum. This high lattice mismatch between the FCC and D0_{23} in the z -direction is slightly reduced as Zr sites are substituted by Ti. The opposite trend is observed for the a parameter of this D0_{23} structure. From an energetic perspective, the substitution of Zr by Ti is not energetically favored according to our DFT simulations (Figure 5.29c) while the classical MD simulations predicted an almost null enthalpy effect upon these atomic substitutions. The small energetic enthalpy barrier predicted by DFT can easily be overcome when increasing temperature due to configurational entropy effects. Therefore it is reasonable to assume that Zr substitutions by Ti (which is experimentally observed) stabilize this structure via configurational entropy effects [215]. At lower temperatures, there is a driving force for this structure to order.

Equivalent conclusions were obtained for the modeling of the pseudo-binary $\text{Al}_3(\text{Ti,Zr})\text{-D0}_{22}$ solid solution (Figure 5.30). For this system, it is found that the c parameter is more than two times the FCC aluminum lattice parameter (Figure 5.30b). Precipitation of the $\text{Al}_3\text{Ti-D0}_{22}$ tetragonal phase particularly is energetically favored by the electronic hybridization between Al p and Ti d electrons. This promotes the formation of this partially symmetrical D0_{22} structure over the cubic $\text{Al}_3\text{Ti-L1}_2$ phase [218]. As such, the parameterized MEAM potential is not able to account for this specific electronic phenomenon due to the simplifications regarding the description of the electronic structure representation. In this case, DFT simulations should provide a more realistic description of the $\text{Al}_3\text{Ti-D0}_{22}$ at 0K. Surprisingly, precise results are

obtained with our MD simulations when compared to DFT. Overall, the determination of other inter-planar distances should be assessed in future work to better understand the effect of these lattice mismatches on the energetic stability of this phase. Dilatation effects upon heating of the FCC and $D0_{23}$ phases should also be considered as they will also influence these results.

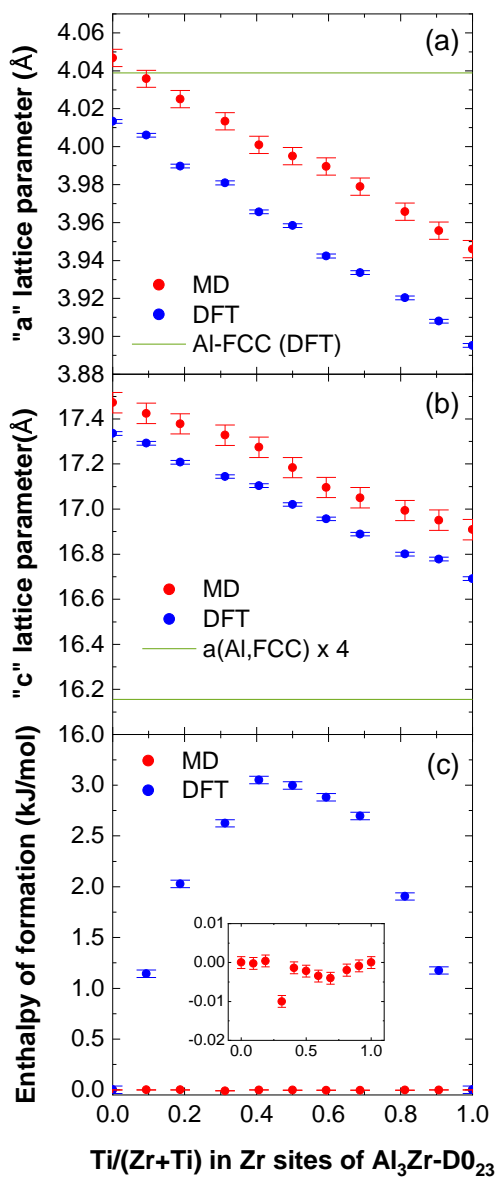


Figure 5.29 Pseudo-binary $Al_3(Zr,Ti)-D0_{23}$ solid solution

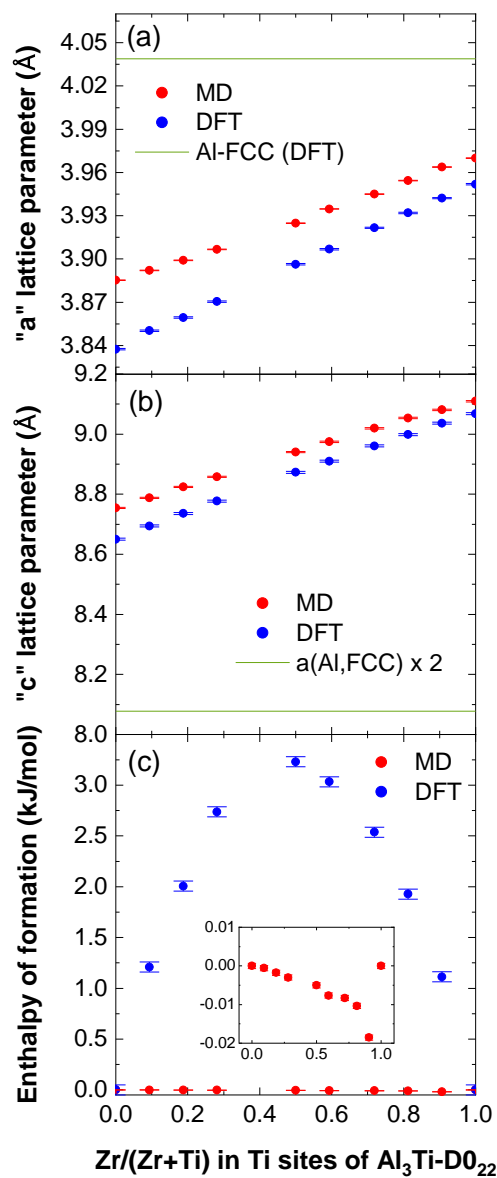


Figure 5.30 Pseudo-binary $Al_3(Ti,Zr)-D0_{22}$ solid solution.

5.6 Conclusions

To investigate the transferability of the classical pairwise additive atomistic force field to the description of unary and multi-component systems, nano/mesoscale MD simulations were performed. It has been found that current interatomic potentials are not entirely transferable for Equilibrium Molecular dynamics (EMD) simulations. This is mainly due to the structure dependence of their parameterization. For unary and binary systems, interatomic models for EMD calculations have a reasonable predicting capability. However, simultaneous descriptions of anisotropic solids and the liquid phase can not be achieved for the entire range of compositions. This is why current interatomic potential remains limited for specific applications. The universality of interatomic potentials and the simplification of interatomic potentials based on pairwise contributions, along with the short length and time scales used in MD, are dominant aspects that limit the proper modeling of multi-component systems. This work opens up the way for developing more extensive interatomic potential formalisms. The effect of the reference structure (BCC and HCP) on the modeling of pure liquid Zr has been assessed using the MEAM formalism. The BCC-based potential provided better agreement with the experimental as BCC is the stable phase at high temperature for this element. The importance of relying on classical thermodynamics during the parameterization of Al-Cu potentials was highlighted. The interatomic potential based on the AlCu₃-L1₂ metastable phase had the closest value of sublimation energy when compared to the solid enthalpy of formation curve of the Al-Cu system obtained by classical thermochemical calculations. This potential accomplished the best modeling of Al-Cu liquid compared to other models. Performance of the Finnis & Sinclair (FS) and the Modified Embedded-Atom Method (MEAM) interatomic potential formalisms has been compared during the crystallization of Pure Al and model Al-Cr alloys. While the simulations performed with the MEAM force field provided coherent solidification of the α -FCC matrix, the FS-based interatomic potential inaccurately promoted a significant solidification of the metastable HCP phase in equilibrium with the α -FCC matrix. The effect of Cr in Al melts was in agreement with the icosahedral nucleation of the α -Al phase by using the MEAM-based interatomic potential. Crystallization of two model alloys within the Al-Zr-Ti system targeting the precipitation of Al₃(Zr_{1-x},Ti_x)-D0₂₃ and Al₃(Ti_{1-y},Zr_y)-D0₂₂ intermetallics has been performed. Simulations resulted in the supersaturation of the α -Al phase due to the high cooling rates. Modelling of the Al₃(Zr_{1-x},Ti_x)-D0₂₃ and Al₃(Ti_{1-y},Zr_y)-D0₂₂ pseudo-binary solid solutions was performed by MD and compared with first-principles calculations. MD results did not achieve the accuracy of first-principles calculations due to the simplifications of the Al-Zr-Ti force field model during its parametrization.

5.7 Acknowledgements

This research was supported by funds from the Natural Sciences and Engineering Research Council of Canada (NSERC), Alcoa, Hydro Aluminum, Constellium, Rio Tinto Aluminum, Elysis and the CRITM. This research was enabled in part by support provided by Calcul-Québec (www.calculquebec.ca) and Compute Canada (www.computecanada.ca).

5.8 Acknowledgement of submission



Figure 5.31 Acknowledgment of receipt of submitted article to *Physical Chemistry Chemical Physics*.

CHAPTER 6 SYNTHESIS AND CHARACTERIZATION OF (AL,SI)₃(ZR,TI)-D0₂₃ AND (AL,SI)₃(TI,ZR)-D0₂₂ INTERMETALLICS: REVEALING SILICON SUBLATTICE SUBSTITUTION AND INTERMETALLIC ENHANCED NUCLEATION OF THE α -Al PHASE

6.1 Abstract

Aerospace and automotive aluminium alloys include peritectic elements such as Ti and Zr to control the as-cast grain size and also to prevent recrystallisation in downstream operations, such as rolling or extrusion. Al₃Ti intermetallics are commonly found at the interface of TiB₂ refiner particles and the α -Al phase. Al₃Zr intermetallics have also been identified as nucleant particles of α -FCC grains; they have been found at the core of α -grains of the 6082 Aluminum Alloy. Besides Ti and Zr, Si is usually present as an impurity or alloying element in aluminum alloys. While mutual substitution of Zr and Ti into the Al₃Zr-D0₂₃ and Al₃Ti-D0₂₂ phases has been extensively reported in the literature, the substitution of Si inside these phases is not clear. Here, *in situ* precipitation of Al₃Zr (D0₂₃) and Al₃Ti (D0₂₂) intermetallics was performed during the solidification of Al-Si-Zr-Ti model alloys. A combination of Scanning Electron Microscopy (SEM), Transmission Electron Microscopy (TEM) and Electron Microprobe (EMP) analysis revealed the presence of both intermetallics concentrated inside an α -FCC matrix. Energy Dispersive X-Ray Analysis (EDX) confirmed that Zr and Ti substitute each other in the D0₂₃ and D0₂₃ tetragonal phases, whereas Si substitutes mainly for Al sublattice sites of both phases. Acceptance of Si inside the Al₃Zr (D0₂₃) phase was not expected according to FactSage, which is a metallurgy-specialized thermochemical package. Based on particle size and growth sequence, experiments suggest that kinetics of precipitation were more favorable for Al₃Ti (D0₂₂) than that of Al₃Zr (D0₂₃), even though classical thermodynamics predicted Al₃Zr (D0₂₃) as first precipitate for all the compositions studied in this work, i.e. with (sample S6) and without (Sample S2) intentional addition of Si. Results suggest that Al₃Ti (D0₂₂) acted as a nucleant particle for Al₃Zr (D0₂₃) followed by nucleation of the α -Al phase in sample S6. While germination of the α -Al phase in sample S2 was achieved with Al₃Ti (D0₂₂) intermetallics.

6.2 Introduction

Primary Al₃Ti-D0₂₂ and Al₃Zr-D0₂₃ intermetallics are frequently encountered in aluminium alloys and master alloys [100]. Depending on the type of aluminum alloys being produced,

their formation/precipitation can either be promoted (such as for grain refinement purposes [219]) or avoided (when these primary phases are formed early in the synthesis process which allows them to grow and to form coarse particle within the aluminum matrix). As an example, Chen & Fortier [220] have recommended to use less than 0.10 wt.% of Ti in the 356/357 aluminium alloys, which is the solubility limit within these Al-Si-Mg-Ti-Fe systems. Their experimental work shows that, above this value, several blocky and flake-like TiAlSi intermetallics precipitate as primary phases during casting. Such intermetallics are problematical as they cause feeding blockage in the tubes of horizontal continuous casting units, wormhole defects in T-ingots, and overall, they are detrimental for cast parts because they compromise the ductility of the materials and can cause surface defects [220]. Grain refinement for ingots of aluminum alloys is employed to promote the formation of equiaxed grains [221]. Formation of large/elongated grains is undesired as they weaken the mechanical properties of cast alloys [222]. For instance, twinned columnar grains compromise the yield strength, tensile elongation to fracture, and fabricability of alloys. Also, coarse-grained structures induce surface defects. Hot cracking in cast ingots is better managed with an equiaxed structure [223]. For wrought aluminum alloys, grain refinement is required to obtain uniform microstructures and refined microporosity [224].

Grain refinement methods are divided into: chemical refining (by adding inoculants to the alloy) and physical refining (by applying external forces to the melt) strategies [109]. Guan & Tie [93] proposed a classification for current processing techniques in aluminium alloys. It includes four categories: the addition of grain refiners, rapid solidification, severe plastic deformation, and finally, grain refining by vibration and stirring during solidification. Grain refinement by inoculant particles has been widely studied for aluminum alloys [225–227]. The potency of Al_3Ti particles as grain refiners was first introduced by Crossley & Mondolfo and explained through the peritectic nucleation theory [45]. This theory correlates the nucleation mechanisms with the peritectic reaction of the Al-rich side of the Al-Ti phase diagram. Al_3Ti intermetallics also play an important role into the nucleation mechanisms established by the duplex nucleation theory in Al-Ti-B based grain refiners. This theory states that an Al_3Ti layer is formed around the TiB_2 grain refiners and remains stable when the grain refiner is added to a hypo-peritectic alloy acting as a nucleation site for the α -Al phase [93]. Mohanty & Gruzleski experimentally showed that the nucleation effectiveness of TiB_2 is dependent of Ti content in aluminum melts. These authors found that TiB_2 did not nucleate the α -Al phase when no excess Ti was added to the melt. At the opposite, the presence of excess Ti in aluminum melts promoted the formation of an Al_3Ti layer at the surface of the TiB_2 particles (even below the peritectic concentration), which subsequently nucleates the α -phase [94]. This is in agreement with the findings of Cornish [95], who concluded

that TiB_2 particles have a stronger nucleation strength when Ti is in excess compared to the TiB_2 stoichiometry. For the case of grain refinement using Al-Ti-C master alloys, Al_3Ti is also found at the TiC_x/Al interface when $x < 0.7$ [96]. Al_3Zr were also reported to act as heterogeneous nucleation sites for the α -Al phase [46]. Chen and Kang [48] studied the solidification of Al-Ti and Al-Zr alloys. They reported that both Al_3Ti and Al_3Zr particles act as heterogeneous nucleation sites for the α -Al phase. This is due to the small interplanar and interatomic mismatch between these phases [48]. Recently, Salloum-Abou-Jaoude et al. [47] reported that Si can be found inside Al_3Zr intermetallics. They also showed that an $\text{Al}_3(\text{Zr}_{1-x-y}, \text{Ti}_x, \text{Si}_y)$ primary intermetallic solid solution acted as a nucleation site for Al α -grains of AA6082 Direct Chill (DC)-cast billets. In their study, a thorough crystallographic analysis to explain the presence of Si within the crystal structure of this solid solution was not performed. The presence of Si in this intermetallic phase was wrongly associated with atomic substitution on Zr and Ti sites [47].

In other aluminum alloy elaboration processes, primary nucleation during solidification is not preferred because the primary particle size is difficult to control. Large faceted $\text{Al}_3\text{Ti-D0}_{22}$ and/or $\text{Al}_3\text{Zr-D0}_{23}$ intermetallics can act as stress concentration zones initiating cracking during downstream processing of wrought aluminium alloys [111, 228]. Because of the critical importance of the $\text{Al}_3\text{Ti-D0}_{22}$ and $\text{Al}_3\text{Zr-D0}_{23}$ intermetallics in the elaboration of aluminum alloys, a precise understanding of their thermodynamic behavior and of the effect of minor solution elements on their energetic stability, crystallography and dynamics of nucleation/growth is crucial for the alloy design of the next generation of advanced aluminum alloys.

The thermodynamic stability of an intermetallic can be greatly modified by the potential addition of alloying elements or impurities within its crystal structure. Silicon is one of such important elements. It is present in various amounts in the majority of aluminum alloys in the form of either an impurity or as an alloying element for both wrought and cast alloys (ex. 4xxx alloys [77], 6xxx alloys [229], A356 alloy [230], etc.). Therefore, understanding the effect of Si on the formation of Al_3Ti and Al_3Zr primary phases becomes a focal point in alloy design. Engineers and scientists could fine-tune its presence to either promote or suppress the formation of key primary intermetallics in aluminum alloys that participate to grain refinement and strengthening mechanisms. A reliable thermodynamic description of Si within the crystal structure of $\text{Al}_3\text{Zr-D0}_{23}$ and $\text{Al}_3\text{Ti-D0}_{22}$ solid solutions is therefore required for designing and fine-tuning the chemistry of the next-generation of aluminum alloys. Both parent-intermetallics are tetragonal and peritectically precipitate in the aluminum-rich side of their respective binary diagrams. These tetragonal phases have a good matching with respect to lattice parameter (a) of the α -Al phase, and have a great thermal stability [29].

CALPHAD-like thermodynamic databases such as the FTlite light alloy database available in the FactSage [12], currently account for Si substitution on Al sublattice sites for the thermodynamic description of the $\text{Al}_3\text{Ti-D0}_{22}$ solid solution via the Compound Energy Formalism (CEF) [214]. The potential substitution of Si on Al sublattices in the $\text{Al}_3\text{Zr-D0}_{23}$ structure is not accounted for. Aside from this energetic description limitation (which is based on experimental results presented in this work), the existing thermodynamic description of the partially ordered D0_{23} phase is able to describe and predict the substitution of peritectic elements such as Ti and V on Zr sublattices. Remarkably, thermodynamic calculations performed with FTlite show that Ti can occupy Zr sites at atomic ratios greater than 0.5 $\text{Ti}/(\text{Ti}+\text{Zr})$ under certain equilibrium conditions, i.e. when the amount of Zr in aluminium alloys is significantly smaller than Ti, but it is enough to stabilize the $\text{Al}_3\text{Zr-D0}_{23}$ over the $\text{Al}_3\text{Ti-D0}_{22}$ phase. The significant solubility of Ti inside the Al_3Zr phase has been already reported by Salloum-Abou-Jaoude et al. [47] in their work on the processing of commercial AA6082 DC-cast billets. Jo et al. (2020) [231] have recently suggested that Si can substitute Al sites in the $(\text{Al,Si})_3(\text{Zr,Ni,Fe})$ D0_{23} -like intermetallic of the Al-14Si-3Cu-4.5Ni casting alloy.

From a recycling point of view, it is advantageous to properly describe Si partitioning within the phase assemblage for scrap recycling processes. Apart from the effective and well-implemented recycling procedures for beverage cans [232], recycling strategies usually involve the mixing of wrought and cast scrap/parts from different sources. Such items comprise castings with considerable amounts of Si [233]. Si can participate on the formation of secondary or subsequent phases of interest for aluminum alloys, such as the α -AlMnSi [234], α -AlFeMnSi [234], α -AlFeSi [235], β -AlFeSi [236], δ - Al_3FeSi_2 [237], π -AlFeMgSi [238], and Mg_2Si [239]. However, precipitation $\alpha(\text{Al})$ as the primary phase can be altered if $(\text{Al,Si})_3(\text{Zr,Ti})$ -based intermetallics ($\text{D0}_{22}/\text{D0}_{23}$) are formed. These intermetallics have great thermal stability due to their peritectic nature [240, 241]. Control of other impurities in the scrap should also be monitored to avoid primary-intermetallic precipitation. That is the case of V, which is more and more found in primary aluminium as a result of the decline in coke quality for anode production [242]. Although substitution of V within $(\text{Al,Si})_3(\text{Zr,Ti})$ -based phases is out of the scope of this study, it has been experimentally proven that V can substitute Zr and Ti sites of both D0_{22} and D0_{23} trialumide intermetallics [29]. First-principle calculations have shown that the $\text{Al}_3(\text{Ti,V})\text{-D0}_{22}$ phase has a close-to-ideal solution behaviour [243], which guarantees stability of phases at high temperature by configurational entropic effects [215]. Analysis of important intermetallics for aluminum alloy manufacturing can be difficult to perform because of their relatively low proportions compared to α -grains or other secondary phases in commercial alloys. Moreover, direct chill casting of commercial aluminum alloys

is performed at relatively high cooling rates, which in the majority of cases prevents the formation of intermetallics, peritect elements (such as Ti and Zr) rather supersaturate the α -Al phase for those conditions. In order to create an environment close to thermodynamic equilibrium, a methodology for the synthesis of massive intermetallics is presented. A Porous Disk Filtration Analyzer (PoDFA) method, adapted with a heating system, is proposed for the synthesis of $\text{Al}_3\text{Zr-D0}_{23}$ and $\text{Al}_3\text{Ti-D0}_{22}$ intermetallics. Control of temperature along with filtration and low cooling rates allowed to obtain large intermetallics concentrated inside an α -matrix. Samples were later analyzed to understand Si site occupancy within the $\text{Al}_3\text{Ti-D0}_{22}$ and $\text{Al}_3\text{Zr-D0}_{23}$ intermetallics. The obtained information can be used at a later stage to refine thermodynamic databases, which are constructed according to the CALPHAD method. This considers crystallography, elemental sublattice substitution, and solubility of external elements inside phases.

6.3 Experimental procedures

1.8 kg of molten alloys were prepared in a furnace at 800°C using master alloys. A crucible containing a PoDFA filter (ABB Group) was preheated inside a chamber adapted with a thermocouple. The crucible is made up of an inner layer stainless steel, an outer shell of carbon steel, and it is insulated with a blanket of synthetic vitreous fiber (SVF). It has an outside diameter of 13.3 cm (5 1/4 in), a height of 20.3 cm (8 in) and a weight of 1.36 kg. The liquid was then transferred into the crucible (Figure 6.1a). Liquid gradually decreased its temperature until reaching the target temperature ($\pm 5^\circ\text{C}$) for the precipitation of intermetallics (Figure 6.1b). The system was equilibrated around the target temperature for 15 min. After that, gauge pressure was increased up to 0.65 bar to start filtration (Figure 6.1c). Finally, the heating source for the chamber was turned off and an α -matrix containing a high concentration of intermetallics was obtained at the bottom of the crucible (Figure 6.1d).

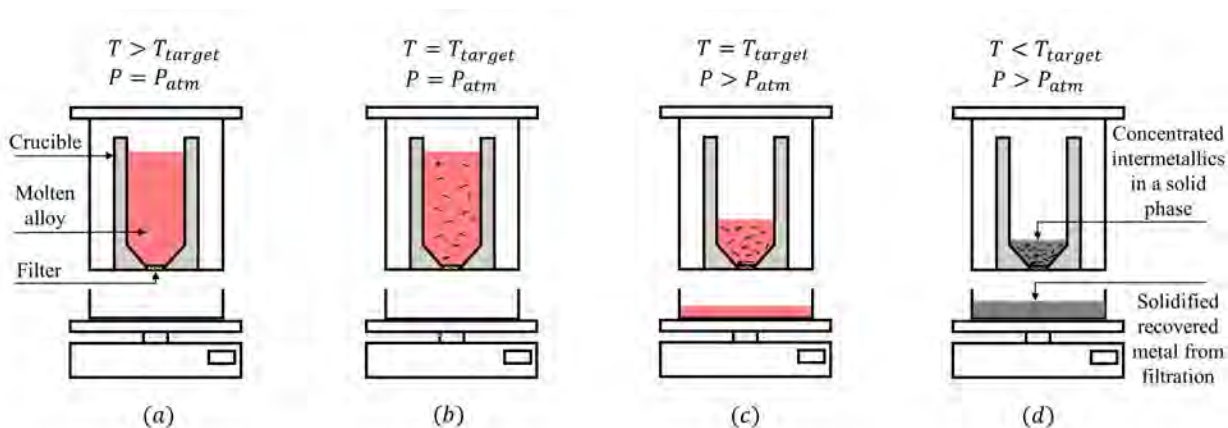


Figure 6.1 Diagram showing different steps during the synthesis of intermetallics in a PoDFA setup

The microstructure was evaluated by means of Electron Microprobe (EMP) and Energy-Dispersive X-ray Spectroscopy (EDS) at the Constellium Technology Center (C-TEC). Crystallography was estimated at the Centre de Caractérisation Microscopique des Matériaux (CM)² by Transmission Electron Microscopy (TEM) analyses. Focused Ion Beam (FIB) preparation was carried out to extract $4\mu\text{m} \times 20\mu\text{m}$ lamella for TEM analysis.

6.4 Results

6.4.1 Chemical composition of molten alloys and their equilibrium phase diagram

Two model alloy compositions were chosen for heated PoDFA experiments. Specimens of molten alloys were collected during alloy preparation at 800°C and solidified in small molds. The composition of specimens was inspected by spark Optical Emission Spectroscopy (Table 6.1). Sample S2 was prepared by adding Zr and Ti into molten aluminum; however, small contamination of Si accounting for 0.04 wt% was detected (Table 6.1). Sample S6 was fabricated with higher amounts of Zr and Ti compared to S2; moreover, it was intentionally doped with 0.92 wt% of Si. Figure 6.2 shows the equilibrium phase diagrams for sample S2 (a) and sample S6 (b), computed with the FTlite database of FactSage [12]. $\text{Al}_3\text{Zr-D0}_{23}$ is the primary precipitate for both compositions according to thermodynamic calculations. $\text{Al}_3\text{Zr-D0}_{23}$ is the equilibrium phase for the imposed equilibration temperature (dark square in Figure 6.2-a) in sample S2. For sample S6, an equilibrium of both $\text{Al}_3\text{Zr-D0}_{23}$ and $\text{Al}_3\text{Ti-D0}_{22}$ phases is predicted (dark square in Figure 6.2-b).

Table 6.1 Nominal composition of S2 and S6 molten alloys and their corresponding equilibration temperature.

Sample	Composition (wt.%)				Measured equilibration temperature
	Zr	Ti	Si	Al	
S2	0.11	0.18	0.04	Balance	703 °C
S6	0.23	0.30	0.92	Balance	716 °C

6.4.2 Microstructural analysis

Solidified samples were examined near the filter side (Figure 6.3a) under light microscope at x100 magnification. Both samples (S2 in Figure 6.3b and S6 in Figure 6.3c) present faceted intermetallics (dark particles) concentrated within the α -FCC matrix (bright area). S6 exhibits a considerable amount of noodle-like intermetallics around the big faceted intermetallic phases. Electron microscopy analysis is presented in further sections to identify the chemistry of the phases. Thermochemical calculations, performed with the FTlite database of FactSage [12], show that the amounts of intermetallics to be obtained are: 2.671 g of $\text{Al}_3\text{Zr-D0}_{23}$ /kg of alloy-S2 and (5.718 g of $\text{Al}_3\text{Zr-D0}_{23}$ + 1.183 g of $\text{Al}_3\text{Ti-D0}_{22}$)/kg of alloy-S6. Therefore, the methodology employed in this work is useful to precipitate and develop big intermetallic particles whose mass fraction is low compared to the α -Al phase. This is an

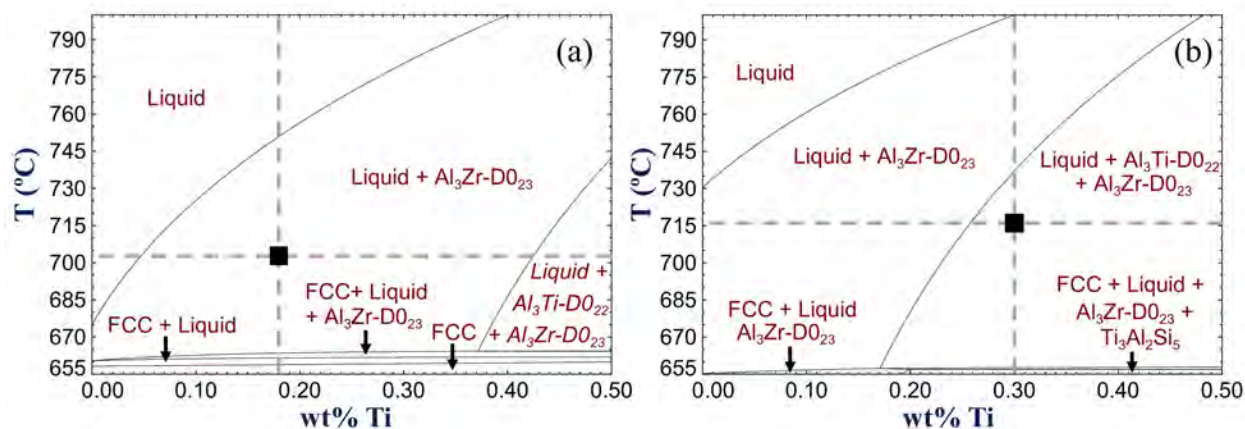


Figure 6.2 Equilibrium phase diagrams for samples S2(a) and S6(b) obtained with FTlite database of FactSage. Black squares correspond to the experimental equilibration temperature before filtration in PoDFA setup

issue frequently observed in the industry when the produced batch's chemistry differs from the specification due to the changes in the raw materials. This PoDFA-based technology helps to study the effect of traces of alloying elements (such as Ti, Zr, V, among others) to stabilize the intermetallic phases.

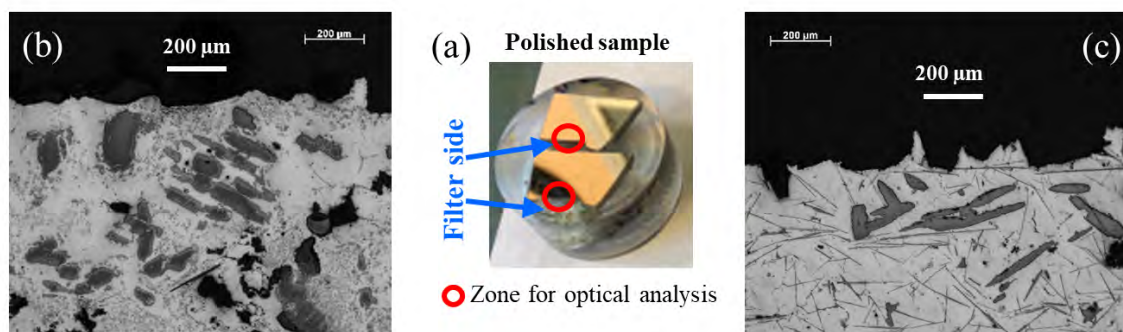


Figure 6.3 Light microscopy micrographs at x100 magnification for solidified samples: S2 (b) and S6 (c). An example of the zone of analysis for the polished samples is presented in (a).

6.4.3 Phase identification

Scanning electron microscope (SEM) micrographs were obtained at specific zones of sample S2 (Figure 6.4a) and sample S6 (Figure 6.4c). The observed phases were analyzed by Energy-dispersive X-ray spectroscopy (EDS) to determine their chemical composition (Table 6.2). Large particles ($> 50 \mu\text{m}$) made up of layers of different phases were identified. Al_3Ti in-

intermetallics have essentially the same chemistry in samples S2 (phase 2 in Figure 6.4b) and S6 (phase 6 in Figure 6.4d). This suggests that the Al_3Ti phase accepted a maximal sublattice substitution of $x = 0.006$ (Si atoms)/(Al sublattice sites), under the specific operational conditions of this work. Zhu et al [244] performed first-principles calculations to investigate Si sublattice substitution in $\text{Al}_3\text{Ti-D0}_{22}$. They found that Si has a highly energetically favourable preference on Al sublattice sites in the tetragonal structure. The same conclusion was obtained by Yang et al. [245] by both EDS analysis and first-principles calculations of the $(\text{Al,Si})_3\text{Ti-D0}_{22}$ phase. In accordance with the chemical analysis, substitution of Zr inside the Al_3Ti intermetallics only occurred in phase 3 (Table 6.2), which is segregated to phase 2 (Figure 6.4-b). Independent and smaller ($<30 \mu\text{m}$) Al_3Zr intermetallics admitting important amounts of Ti (phase 4 in Table 6.2) are also observed inside the $\alpha\text{-Al}$ phase of sample S2 (phase 4 in Figure 6.4-b). For sample S6, the Al_3Ti phase was surrounded by Al_3Zr layers with comparable Zr/Ti ratios (phases 7 and 8 in Figure 6.4-d). Contrary to sample S2, Al_3Zr phases in sample S6 accepted considerable amounts of Si, representing around 0.05 (Si atoms)/(Al sites). Which is 8 times larger than the substitution of Si in the Al_3Ti phase. Karpets et al. [41] evaluated the stability of the $\text{Al}_3(\text{Ti}_{1-x}\text{Zr}_x)$ solution at different Zr/(Zr+Ti) ratios between 0 and 1. When only Ti was present in the system, the $\text{Al}_3\text{Ti-D0}_{22}$ was the stable structure while $\text{Al}_3\text{Zr-D0}_{23}$ was the stable phase when Ti was not included. For the range [0.04:0.32] of Zr/(Zr+Ti) during alloy preparation, they found an equilibrium between the D0_{22} and D0_{23} phases. Peculiarly, the D0_{22} phase accepted a Zr sublattice substitution of only [0.035:0.08] (Zr atoms)/(Ti sites), while the D0_{23} phase was able to substitute Ti at [0.88:0.59] (Ti atoms) / (Zr sites). The above suggests that Al_3Ti intermetallics obtained in this work have a D0_{22} structure, while the Al_3Zr phase has a D0_{23} configuration. Al_3Zr intermetallics outside the big particle of sample S6 were also observed (Figure 6.4-e). Phase 9 has a chemical composition close to the Al_3Zr phase at the shell of the big particle of S6 (phase 8 in Figure 6.4-d), with a slightly higher ratio of Zr/Ti. However, Phase 10 contained considerably greater amounts of Zr and accepted more Si sublattice substitution compared to phase 9. The Further section includes a comparison between the equilibrium phases of this work, and computational thermochemistry predictions using FactSage [12].

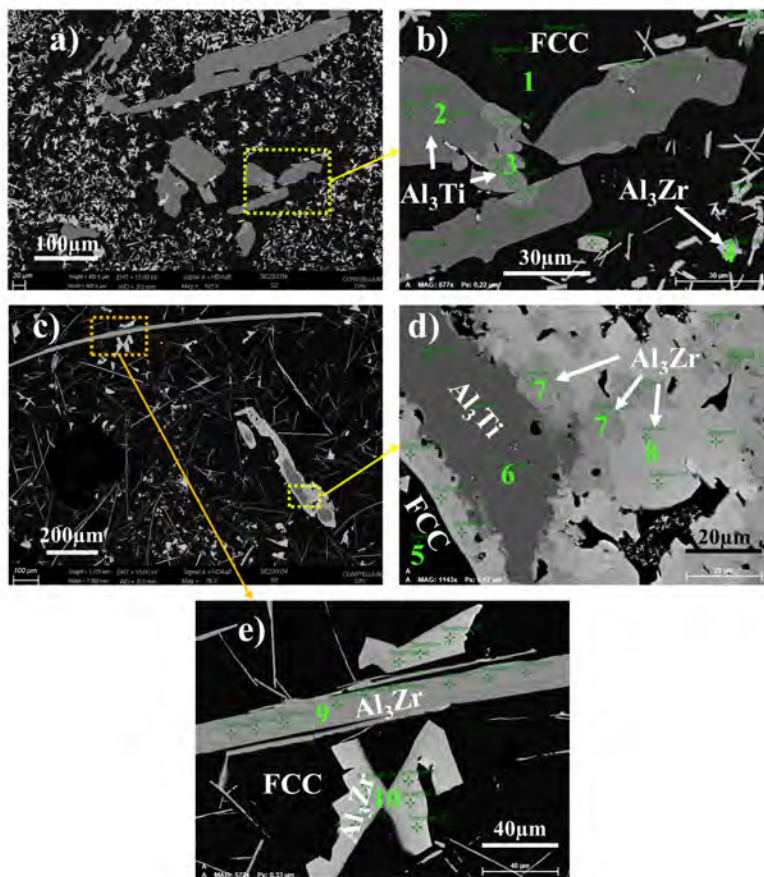


Figure 6.4 Scanning electron microscope (SEM) micrographs. (a) and (b) correspond to sample S2, (c), (d) and (e) stand for sample S6. Green letters highlight the different phases within each sample. The chemical composition of the phases is reported in Table 6.2.

Table 6.2 Chemical composition of phases reported in Figure 6.4

Sample	Label	Phase	at.%					Substitution ratio	
			Al	Si	Al+Si	Ti	Zr	Zr/(Zr+Ti)	Si/(Al+Si)
S2	1	FCC	99.28	0.37	...	0.22	0.13
	2	Al ₃ Ti	74.71	0.42	75.12	24.88	0.00	0.00	0.006
	3	Al ₃ Ti	75.11	0.15	75.26	23.02	1.71	0.07	0.002
	4	Al ₃ Zr	74.65	0.15	74.80	17.91	7.29	0.29	0.002
S6	5	FCC	98.44	1.38	...	0.09	0.10
	6	Al ₃ Ti	73.91	0.44	74.36	25.64	0.00	0.00	0.006
	7	Al ₃ Zr	70.56	3.91	74.47	22.02	3.51	0.14	0.053
	8	Al ₃ Zr	70.62	3.76	74.38	21.47	4.15	0.16	0.051
	9	Al ₃ Zr	71.13	3.35	74.48	21.18	4.34	0.17	0.045
	10	Al ₃ Zr	69.64	4.68	74.31	18.76	6.93	0.27	0.063

6.4.4 Thermodynamic calculations

In this section, thermodynamic calculations have been performed based on the experimentally measured mass balance of the molten samples (Table 6.1). Numerical simulations were carried out using the equilibrium mode of FactSage [12] at the experimental equilibration temperature in the PoDFA setup and with variations on the wt% of Zr (Figure 6.5). The evolution of the activity of the $D0_{22}$ and $D0_{23}$ solid solutions is presented in Figures 6.5a and 6.5b for sample S2 and S6, respectively. The maximal value in the x-axis of Figure 6.5a and Figure 6.5b corresponds to the actual concentration of Zr in the alloys as obtained by spark Optical Emission Spectroscopy (Table 6.1). The equivalent experimental composition is also presented by horizontal gray lines for samples S2 (0.11 wt% of Zr) in Figure 6.5c and Figure 6.5e, and for sample S6 (0.23 wt% of Zr) in Figure 6.5d and Figure 6.5f, which show the evolution of the molar fraction of Al, Si, Ti, Zr within the $D0_{22}$ (solid lines) and $D0_{23}$ (dashed lines) phases as function of the wt% of Zr. Superposed symbols to the gray lines stand for the molar fraction of the phase' constituents measured by EDX analysis (as previously shown in Figure 6.4 and Table 6.2).

Activities of $D0_{22}$ and $D0_{23}$ phases in sample S6 were equal to 1 (Figure 6.5b) for the measured experimental concentration (at 0.23 wt% of Zr), implying that both phases are thermodynamically stable under the imposed temperature. This is in agreement with the experimental observations. Nevertheless, the $D0_{23}$ was the only equilibrium phase to be expected for sample S2 (Figure 6.5a at 0.11 wt% of Zr). Contrary to thermodynamic predictions, experiments show that the $D0_{22}$ phase also formed in equilibrium with the $D0_{23}$ phase even for sample S2. Srinivasan & Chattopadhyay mentioned that the Al_3Zr-D0_{23} phase has sluggish growth kinetics [246]. It appears that the Al_3Ti phase is kinetically privileged when compared to the Al_3Zr-D0_{23} phase despite of having an activity < 1 (sample S2). It is to be noted that the activity of Al_3Ti-D0_{22} is not negligible and quite similar to that of the $D0_{23}$ phase for the studied conditions (Figure 6.5a), this means that both phases have an equivalent thermodynamic driving force to precipitate. However, the kinetics of precipitation are more favourable for the Al_3Ti-D0_{22} phase than for the Al_3Zr-D0_{23} .

Equilibrium thermodynamic calculations show that the Al_3Ti-D0_{22} phase only accepts a limited amount of Zr (solid purple line in Figure 6.5c and in Figure 6.5d). Conversely, the Al_3Zr-D0_{23} phase is able to substitute high amounts of Ti in Zr sublattice sites (dashed orange line in Figure 6.5e and in Figure 6.5f). This confirms that the Al_3Zr-D0_{23} phase can stabilize even if most of Zr sites are occupied by Ti atoms. Karpets et al. [41] experimentally found that Zr fractions $[Zr/(Zr+Ti)]$ of only 0.1 are enough to stabilize the $D0_{23}$. This is attributed to the configurational effects induced by the disposition of atoms in the $D0_{23}$

phase. Indeed, both tetragonal phases share the same space group ($I4/mmm$), but more atoms are required to describe the primitive cell of the complex $D0_{23}$ phase when compared to the $D0_{22}$ structure. It can be observed that thermodynamic calculations already consider Si sublattice substitution in Al sites in the Al_3Ti-D0_{22} phase (green solid line in Figure 6.5d). However, the amount of Si substitution in the intentionally Si-doped sample (Figure 6.5d) was overestimated compared to the almost negligible Si substitution in phase 6. On the other side, numerical simulations indicate that Si substitution within the $D0_{23}$ was not permitted (green dashed line in Figure 6.5f). By analyzing the current thermodynamic modelling of Al_3Zr-D0_{23} inside the FTlite database of FactSage, it was noticed that Si sublattice substitution has not been integrated yet. As such, an end-member accounting for Si substitution should be incorporated within the $D0_{23}$ solid solution. It is to be noted that the model showed an appropriate prediction for the $D0_{23}$ (phase 4 in Figure 6.5e) of the non-Si-doped sample (S2).

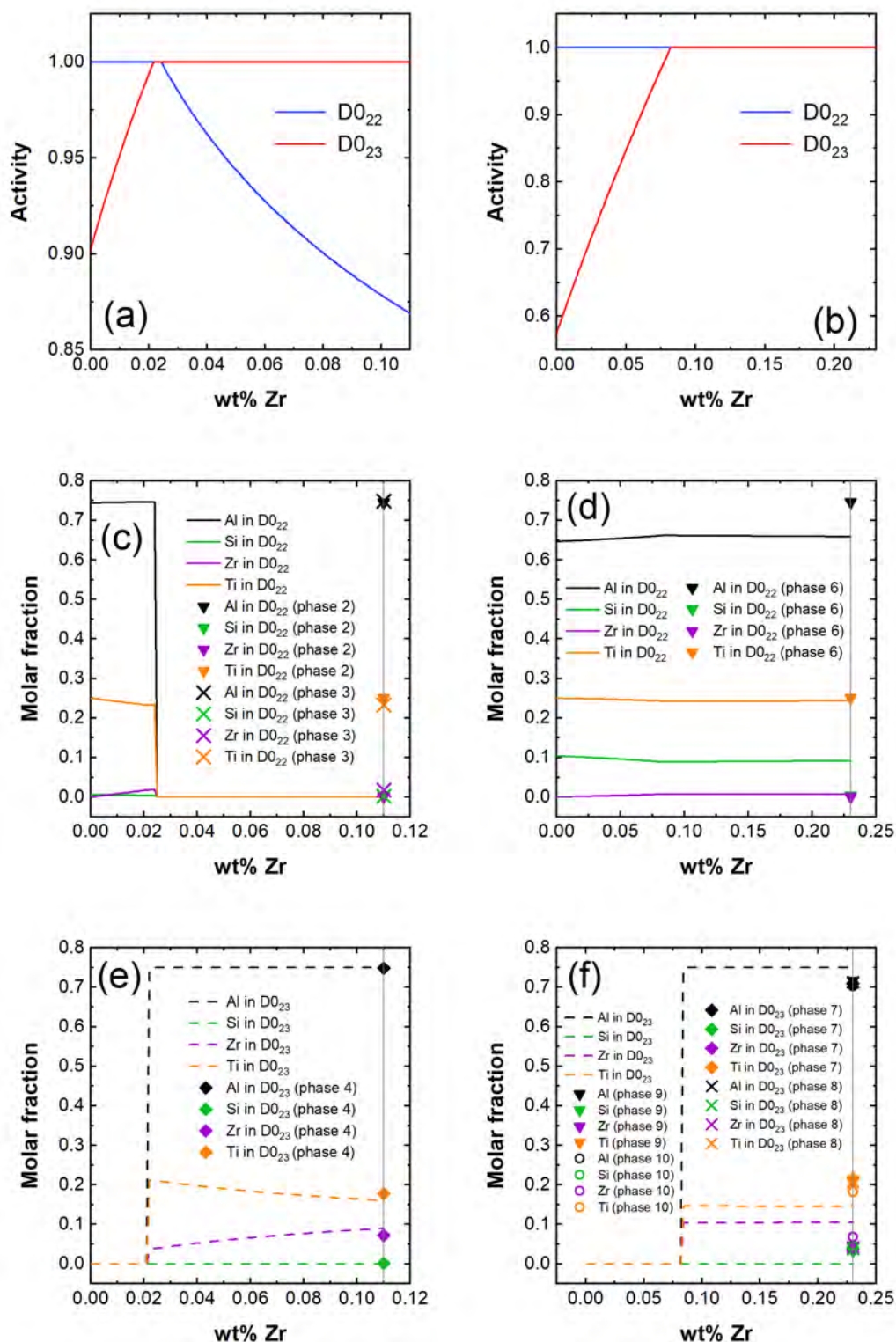


Figure 6.5 Activities of D0₂₂ and D0₂₃ phases in samples S2 (a) and S6(b) considering variations on the concentration of Zr, the maximum in the x-axis corresponds to the actual amount of Zr in the studied alloys. Evolution of elements inside D0₂₂ and D0₂₃ phases (contemplating Zr variations) for samples S2 (c and e) and S6 (d and f) are also reported.

Thermodynamic calculations were computed at the target equilibrium temperature in PoDFA setup, i.e. at 703°C for sample S2 and 716°C for S6; and by keeping constant the concentrations of Ti and Si as reported in Table 6.1. Symbols are the experimental molar fractions of phases reported in Table 6.2.

6.4.5 Crystallographic analysis

Selected Area Electron Diffraction (SAED) patterns were acquired for three different zone axes of the α -Al and $\text{Al}_3\text{Ti-D0}_{22}$ phases in a specific region of sample S2 (Figure 6.6). Zone axes for α -Al phase correspond to the [011], [112] and [013] families of directions. SAED patterns were obtained for almost identical tilts of the goniometer for the three phases, which demonstrates coherency between crystals. This allowed to characterize the $\text{Al}_3\text{Ti-D0}_{22}$ phases by following analogous [001], $[\bar{1}21]$ and [031] zone axes of the α -Al phase. Nucleation of coherent phases appeared to follow the sequence: $\text{Al}_{2.98}\text{Si}_{0.02}\text{Ti-D0}_{22} \rightarrow \text{Al}_{2.99}\text{Si}_{0.01}\text{Ti}_{0.93}\text{Zr}_{0.07}\text{-D0}_{22} \rightarrow \alpha\text{-Al}$ phase. Lattice parameters for three phases are presented in Figure 6.6. Wang et al [247] reported an experimental value of $a = 3.857 \text{ \AA}$ and $c = 8.584 \text{ \AA}$ for $\text{Al}_3\text{Ti-D0}_{22}$, Karpets et al. [41] reported $a = 3.853 \text{ \AA}$ and $c = 8.587 \text{ \AA}$. Also, Norby & Christensen [248] indicated $a = 3.8537 \text{ \AA}$ and $c = 8.5839 \text{ \AA}$. Lattice parameters of the $\text{Al}_3\text{Ti-D0}_{22}$ intermetallics of this work were $a = 3.90 \text{ \AA}$ and $c = 8.65 \text{ \AA}$ for $\text{Al}_{2.98}\text{Si}_{0.02}\text{Ti-D0}_{22}$ and $a = 3.92 \text{ \AA}$ for and $c = 8.65 \text{ \AA}$ $\text{Al}_{2.99}\text{Si}_{0.01}\text{Ti}_{0.93}\text{Zr}_{0.07}\text{-D0}_{22}$. The "a" parameter increased due to Zr sublattice substitution in Ti sites of the D0_{22} . This phenomenon is discussed in further sections of this work regarding the comparison of TEM analysis values with atomistic simulations.

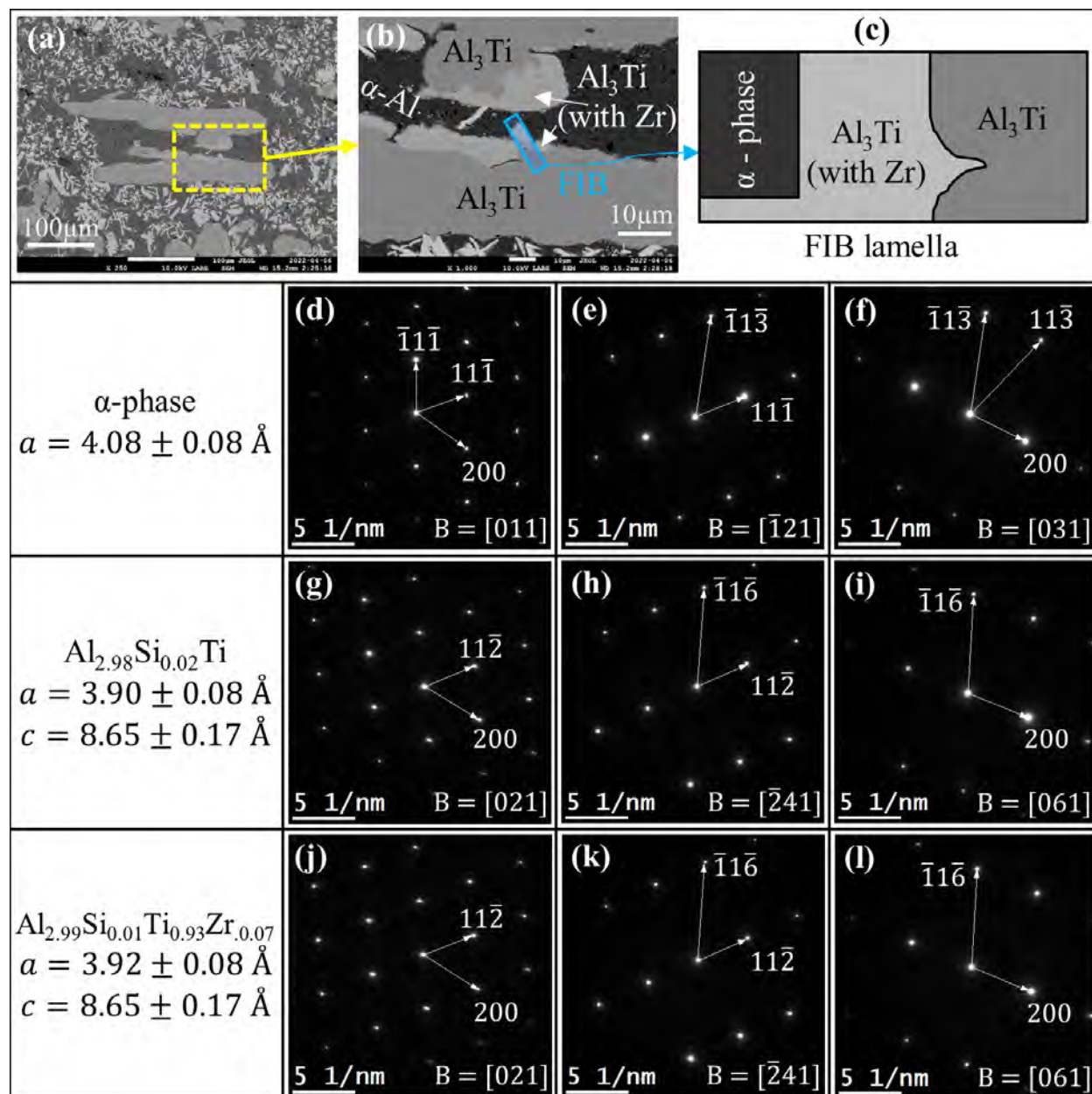


Figure 6.6 Summary of the TEM analysis performed for sample S2. (a) and (b) are micrographs showing the target zone for FIB sectioning (blue rectangle) to obtain a FIB lamella (c). Selected area electron diffraction patterns are presented in (d), (e) and (f) for the α -phase; (g), (h) and (i) for the $\text{Al}_{2.98}\text{Si}_{0.02}\text{Ti}$ -D0₂₂ phase; and (j), (k) and (l) for the $\text{Al}_{2.99}\text{Si}_{0.01}\text{Ti}_{0.93}\text{Zr}_{0.07}$ -D0₂₂ phase.

For sample S6, SAED patterns were obtained for three different zone axes for the $\text{Al}_3\text{Ti-D0}_{22}$ phase and for two grains of the $\text{Al}_3\text{Zr-D0}_{23}$ phase, as illustrated in Figure 6.7c. Additional SAED patterns were collected at the interface of α -FCC and $\text{Al}_3\text{Ti-D0}_{22}$ phases (Figure 6.7m), and at the interface of the α -FCC and $\text{Al}_3\text{Zr-D0}_{23}$ phases (Figure 6.7n). This revealed crystallographic coherence between phases. Lattice parameters of Al_3Ti intermetallics of sample S6 are comparable to those in Al_3Ti in sample S2 as they have equivalent chemistry.

The $\text{Al}_{2.84}\text{Al}_{0.16}\text{Zr}_{0.14}\text{Ti}_{0.86}\text{-D0}_{23}$ phase (G2 in Figure 6.7-c) have lattice parameters of $a = 3.90 \text{ \AA}$ and $c = 17.52 \text{ \AA}$. The $\text{Al}_{2.85}\text{Al}_{0.15}\text{Zr}_{0.17}\text{Ti}_{0.83}\text{-D0}_{23}$ (G1 in Figure 6.7-c) exhibited lattice constants of $a = 3.88 \text{ \AA}$ and $c = 17.52 \text{ \AA}$ (G1 in Figure 6.7-c). Karpets et al. [41] reported $a = 3.998 \text{ \AA}$ and $c = 17.276 \text{ \AA}$ for the stoichiometric $\text{Al}_3\text{Zr-D0}_{23}$, they also stated that lattice parameters of this phase decrease as Ti atoms substitute Zr sites. e.g., for $\text{Al}_3\text{Zr}_{0.12}\text{Ti}_{0.88}\text{-D0}_{23}$ and $\text{Al}_3\text{Zr}_{0.17}\text{Ti}_{0.83}\text{-D0}_{23}$ phases. They found $a = 3.927 \text{ \AA}$ and $c = 16.684 \text{ \AA}$; and $a = 3.932 \text{ \AA}$ and $c = 16.707 \text{ \AA}$, respectively. The values of the lattice parameters found in this work not only are affected by the acceptance of Ti in Zr sites, but also by Si sublattice substitution of Al sites. Which explains the discrepancies between the lattice parameters of this work and those reported in the literature.

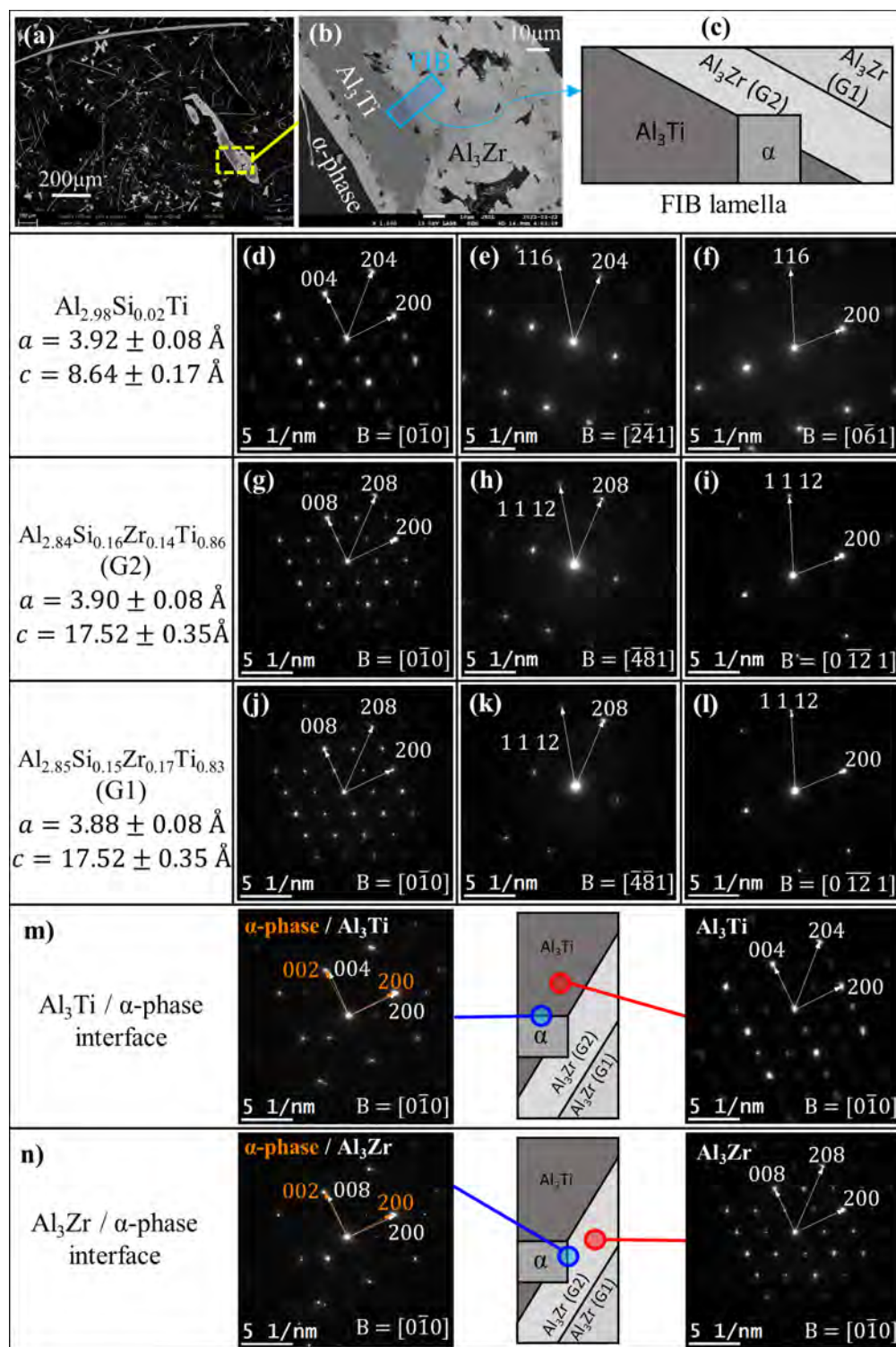


Figure 6.7 Summary of the TEM analysis performed for sample S6. (a) and (b) are micrographs showing the target zone for FIB sectioning (blue rectangle) to obtain a FIB lamella (c). Selected area electron diffraction patterns are presented in (d), (e) and (f) for the Al_3Ti -D0₂₂ phase; (g), (h) and (i) for the grain “G2” of the Al_3Zr -D0₂₃ phase; (j), (k) and (l) for grain “G1” of the Al_3Zr -D0₂₃ phase. m) and n) show the crystallographic coherence between α -phase/ Al_3Ti -D0₂₂ and α -phase/ Al_3Zr -D0₂₃, respectively.

A summary of the lattice parameters of the analyzed phases of this work is presented in Table 6.3. Lattice mismatch of intermetallics was compared the “a” parameter of the α -Al phase. For the three directions of the fundamental unitary cells, the lattice difference of intermetallics with respect to the α -Al phase is small. The small lattice misfit ratio suggests that (Al,Si)₃(Zr,Ti)-based intermetallics acted nucleation sites for the α -Al phase and resulted in crystallographic coherency of these phases as shown in the SAED patterns.

Table 6.3 Summary of lattice parameters for the different phases synthesized in this work compared to values from the literature. Lattice misfit between the intermetallics and the α -Al phase are also presented.

	Phase	Lattice parameter		Lattice misfit		
		a (\AA)	c (\AA)	$\frac{a}{a(FCC)}$	$\frac{c(D0_{22})}{2a(FCC)}$	$\frac{c(D0_{23})}{4a(FCC)}$
Sample S2	FCC	4.08
	Al _{2.98} Si _{0.02} Ti	3.90	8.65	0.96	1.06	...
	Al _{2.99} Si _{0.01} Ti _{0.93} Zr _{0.07}	3.92	8.65	0.96	1.06	...
Sample S6	FCC	4.08
	Al _{2.98} Si _{0.02} Ti	3.92	8.64	0.96	1.06	...
	Al _{2.84} Si _{0.16} Zr _{0.14} Ti _{0.86} (G2)	3.90	17.52	0.96	...	1.07
	Al _{2.85} Si _{0.15} Zr _{0.16} Ti _{0.84} (G1)	3.88	17.52	0.95	...	1.07
Literature	FCC	4.05 [29, 249]
	Al ₃ Ti-D0 ₂₂	3.857 [247]	8.584 [247]
		3.853 [41]	8.587 [41]
		3.8537 [248]	8.5839 [248]
	Al ₃ Ti _{0.965} Zr _{0.035} -D0 ₂₂	3.855 [41]	8.612 [41]
	Al ₃ Ti _{0.93} Zr _{0.07} -D0 ₂₂	3.862 [41]	8.650 [41]
	Al ₃ Zr-D0 ₂₃	3.998 [41]	17.276 [41]
	Al ₃ Zr _{0.12} Ti _{0.88} -D0 ₂₃	3.927 [41]	16.684 [41]
	Al ₃ Zr _{0.17} Ti _{0.83} -D0 ₂₃	3.932 [41]	16.707 [41]

Finally, the lattice parameters of the different phases obtained by TEM analysis were compared to Molecular dynamics (MD) data [27], Density Functional Theory (DFT) calculations [27, 28] and to a fitting from experimental measurements through the Vegard’s rule obtained by Han et al. [29] (Figure 6.8). All these values are also compared to the lattice parameter of the Al-FCC at 0 K (Green horizontal line in Figure 6.8) from DFT calculations [11]. This shows that the lattice parameter of both phases is increased by increasing the amount of Zr within the Zr/Ti sublattice sites. This behaviour is favourable to reduce the lattice misfit of the "a" parameter of both tetragonal phases with respect to the Al-FCC. However, the misfit of the "c" parameter of the D0₂₂ phase with respect to two times the "a" parameter of the Al-FCC is increased. The same trend is observed with the "c" parameter of the D0₂₃ with respect to 4x"a" from the Al-FCC.

"a" and "b" parameters of the $\text{Al}_3\text{Ti-D0}_{22}$ phase (Figure 6.8a and Figure 6.8b, respectively) are in reasonable agreement with the data found in the literature. This is because only minor acceptance of Si was observed experimentally, which allows to compare the data of the pseudo-binary solid solution that does not include Si in the numerical simulations. Although the "a" (Figure 6.8c) parameter of the D0_{23} phase seems to be in good agreement with the reported data, the "c" parameter (Figure 6.8d) significantly differs from the reported references. These deviations are due to the Si acceptance within the D0_{23} , which are not considered in the compared data.

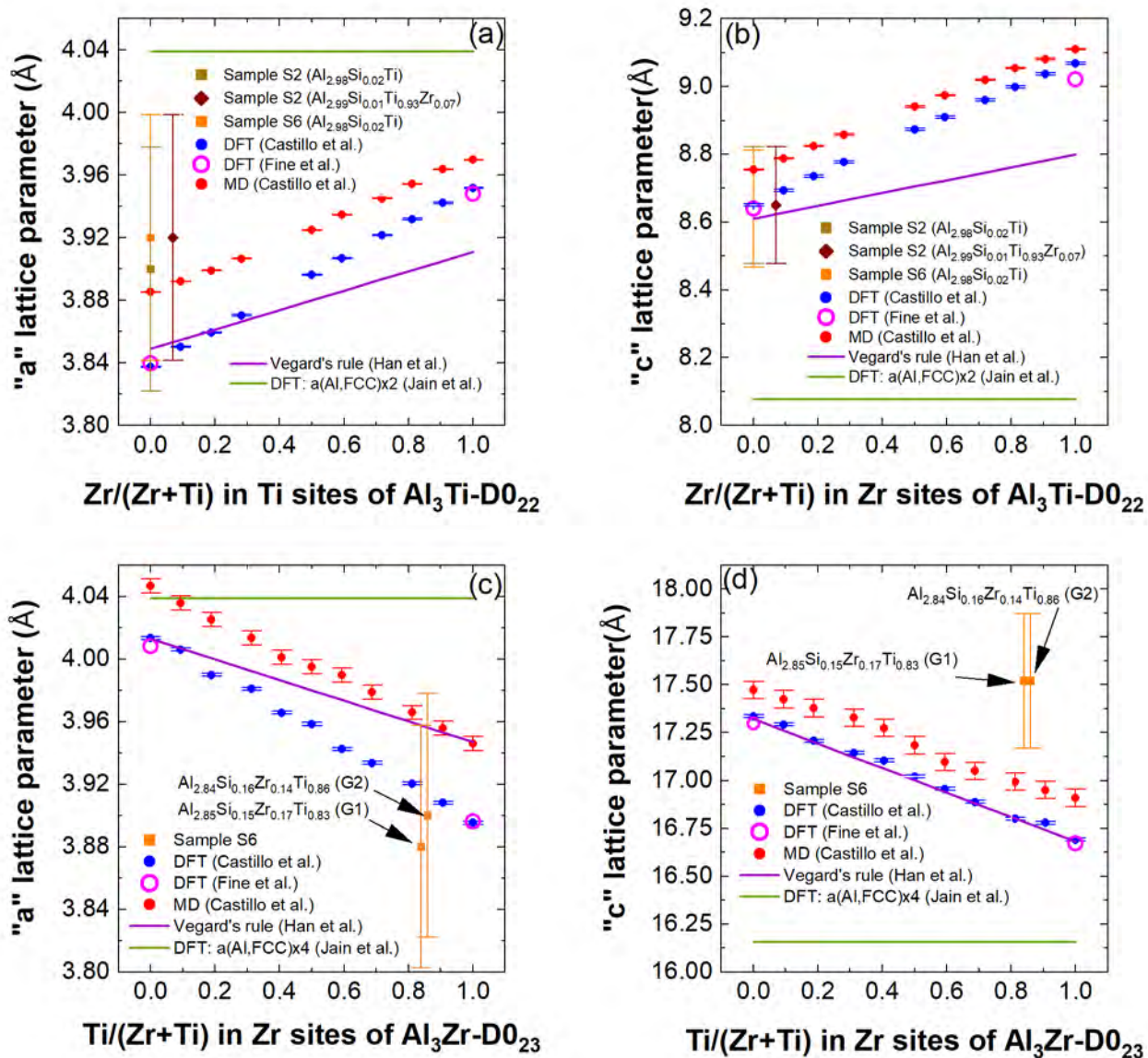


Figure 6.8 Lattice parameters for some intermetallic phases found in sample S2 (brown squares and dark red diamond) and sample S6 (orange squares). Compared to MD (red circles) and DFT (blue circles) calculations from [27], DFT (magenta open circles) from [28], a fitting with the Vegard's rule (purple line) of [29] and the "a" parameter of Al-FCC from DFT calculations from [11].

6.4.6 Elemental mapping analysis

Electron microprobe (EMP) analysis for samples S2 and S6 are respectively presented in Figure 6.9 and Figure 6.10. Big particles at the center of mapping for sample S2 (Figure 6.9) are mainly made up of $\text{Al}_3\text{Ti-D0}_{22}$ with minor segregation of $\text{Al}_3(\text{Ti,Zr})\text{-D0}_{22}$ at the shell. Smaller Al_3Zr intermetallics were also observed around the big particles. It appears that Al_3Ti was the first precipitate and developed as big particles within the liquid during equilibration in the PoDFA setup. Even though classical thermodynamics only predicted the presence of $\text{Al}_3\text{Zr-D0}_{23}$ for mass balance and equilibration conditions of this sample.

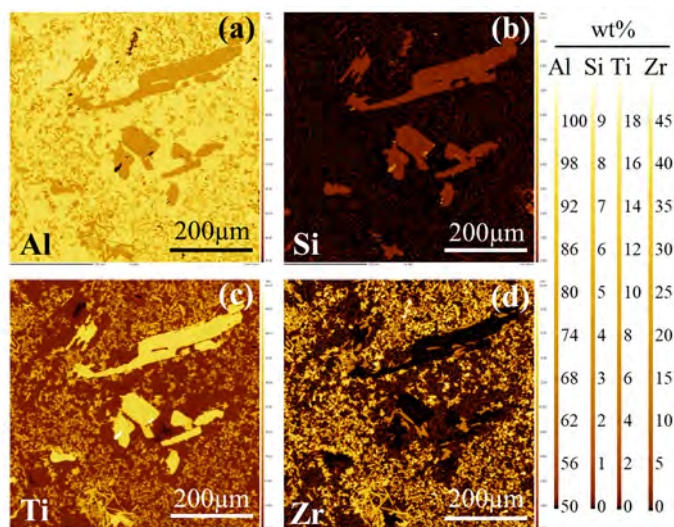


Figure 6.9 Electron microprobe elemental maps for sample S2. (a) Al map, (b) Si map, (c) Ti map and (d) Zr map.

For sample S6, the big particle corresponds to $\text{Al}_3\text{Ti-D0}_{22}$ at the core and $\text{Al}_3\text{Zr-D0}_{23}$ on the shell (Figure 6.10). This suggests that $\text{Al}_3\text{Ti-D0}_{22}$ was the first precipitate and acted as a nucleant for the precipitation of $\text{Al}_3\text{Zr-D0}_{23}$. Figure 7b shows that Si is accepted in bigger proportions in $\text{Al}_3\text{Zr-D0}_{23}$ than it does in $\text{Al}_3\text{Ti-D0}_{22}$.

6.5 Conclusions

The present work discussed the process to precipitate and concentrate $\text{Al}_3(\text{Zr,Ti})$ -based intermetallics using the PoDFA technology. The main conclusions are:

1. Synthesis of low mass fraction ($<10\text{g/kg}$ of alloy) $\text{Al}_3(\text{Zr,Ti})$ intermetallics within Al-Si-Zr-Ti alloys was accomplished.

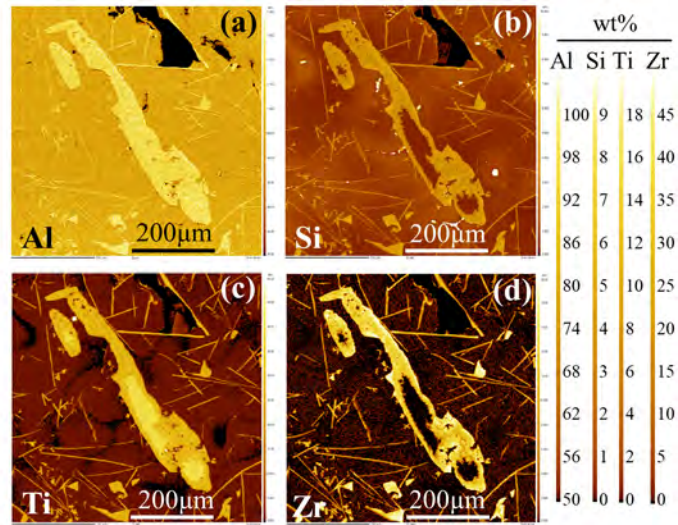


Figure 6.10 Electron microprobe elemental maps for sample S6. (a) Al map, (b) Si map, (c) Ti map and (d) Zr map.

2. Sublattice substitution of Si within Al sites of the $\text{Al}_3\text{Zr-D0}_{23}$ and $\text{Al}_3\text{Ti-D0}_{22}$ phases was confirmed.
3. Crystallographic analysis corroborated the effective germination of the alpha-FCC phase with $\text{Al}_3(\text{Zr,Ti})$ intermetallics. This will be highly valuable for new alloy design, whether to control grain size of the α -Al phase by primary peritectic phases or to suppress tetragonal phases by chemically stabilizing others.
4. Kinetics of precipitation appeared to be more favorable for $\text{Al}_3\text{Ti-D0}_{22}$ intermetallics than for $\text{Al}_3\text{Zr-D0}_{23}$.
5. Reported data in this work will serve as benchmark data for refining thermodynamic databases to better describe the $\text{Al}_3\text{Zr-D0}_{23}$ and $\text{Al}_3\text{Ti-D0}_{22}$ phases.

CHAPTER 7 GENERAL DISCUSSION

Exploration of large-scale Molecular Dynamics (MD) simulations and experimental work have been carried out to determine primary phases in aluminum alloys. The transferability of interatomic potential models for MD to describe different solid and liquid solutions was compared to reliable data found in the literature (i.e., experiments, first principle-calculations, and computational thermochemistry). By accomplishing objectives **O1-O4**, it is concluded that current force field models are not completely transferable for solution modeling and complex solidification studies. The accuracy of these models for unary and binary systems is acceptable; however, it is compromised as more elements are included in a complex system. We also highlight the importance of the reference structure during the parametrization of Zr, Al-Cu, Al-Cr, and Al-Zr-Ti systems using robust force field models. As well as the need to verify the consistency of first-principles calculations and computational thermochemistry previous to the parametrization of interatomic potentials.

An important finding of this work is the effect of Cr on the local ordering of Al-Cr melts. Indeed, Icosahedral short-range ordering (ISRO) was promoted in Al-Cr melts by increasing the amount of Cr. This was found through objective **O5**. We have found that Cr prevents undercooling in Al-Cr melts through icosahedral quasicrystal-enhanced nucleation of the Al-FCC phase, which is a recently reported theory explaining the grain refinement mechanisms in Al-Zn-Cr alloys. These results are obtained using the modified embedded atom method (MEAM) potential. But they were not reproducible when using a force field model based on the Finnis and Sinclair (FS) formalisms. This shows the robustness of the MEAM potential over the FS to describe solidification on the Al-Cr systems.

Objective **O6** was to predict intermetallic primary phases within Al-Zr-Ti. Target phases were Al_3Ti and Al_3Zr intermetallic; however, MD simulations showed that Ti and Zr rather supersaturate the α -Al phase due to the high cooling rates. Solidification simulations for Al-Cr hyper-peritectic alloys was also tested through objective **O6**. Simulations also resulted in the supersaturation of the Al-FCC phase, which is an imminent result of the current timescales allowed in MD using super-computers. Precipitation of the meta-stable HCP phase was also observed in pure Al and Al-alloys; the solidified HCP/FCC ratio was found to be highly dependent on the force field formalism. Where the MEAM exhibiting more coherent Al-FCC solidification than the FS-based models.

Objective **O7** was achieved by synthesizing $\text{Al}_3\text{Ti-D0}_{22}$ and $\text{Al}_3\text{Zr-D0}_{22}$ intermetallics using a PoDFA setup. Presence of this intermetallics within an FCC-matrix was firstly observed with

light microscopy analysis. After that, characterization of intermetallics (Objective **O8**) was carried out by means of Electron Microprobe (EMP), Energy-Dispersive X-ray Spectroscopy (EDS), and Transmission Electron Microscopy (TEM) analysis. Substitution of Si within Al sublattice sites was confirmed in both tetragonal phases. This information is useful to refine the FTLite database of Factsage, which do not considered this phenomemon in the $\text{Al}_3\text{Zr-D0}_{23}$ phase. Selected Area Electron Diffraction (SAED) patterns showed that $\text{Al}_3\text{Ti-D0}_{22}$ and $\text{Al}_3\text{Zr-D0}_{23}$ intermetallics can act as nucleant particles for the α -Al phase (Objective **O8**). This second part reflects the importance of relying on experiments to fit thermodynamic models used in classical thermochemistry. We have also investigated the transferability of the Al-Zr-Ti force field for the complex modeling of these $\text{Al}_3(\text{Ti,Zr})$ -based pseudo-binary solid solutions (Objective **O3**). The performance of MD simulations for such a task was judged by comparing them to Density functional theory (DFT) calculations. Although energetic predictions from MD were not as precise as DFT, they provided an appropriate trend about the effect of Si/Ti sublattice substitution on the lattice parameters of the solution. This information was useful to study the lattice misfit between the Al-FCC phase and $\text{Al}_3(\text{Ti,Zr})$ -based intermetallics as reported in Chapter 6.

CHAPTER 8 CONCLUSION

Large-scale Molecular Dynamic (MD) simulations were performed to study the solidification of Al-based alloys. Additionally, experimental work was carried out to identify primary intermetallics during the solidification of Al-Si-Zr-Ti-based alloys. Our solidification simulations for hyper-peritectic Al-alloys bring awareness of the rapid solidification effects in large-scale systems. Such as supersaturation of the Al-FCC phase. Another important finding of this work is the effect of Cr on the local ordering of Al-Cr melts and their solidification, which is in agreement with the icosahedral quasicrystal-enhanced nucleation of the Al-FCC phase reported in the literature. We also highlight the importance of the reference structure during the parametrization of Zr, Al-Cu, Al-Cr, and Al-Zr-Ti systems using robust force field models. The exploration of these systems was encouraged by the industrial partners of this research project (some major aluminum alloy producers).

The submitted manuscript to *Physical Chemistry Chemical Physics* is complementary to their recent published studies regarding the solidification of pure metals using MD simulations (see for example *Cooling rate dependence of solidification for liquid aluminium: a large-scale molecular dynamics simulation study*, and *Molecular dynamics investigation of the local structure in iron melts and its role in crystal nucleation during rapid solidification*), where a fundamental understanding of the MD predicting capabilities for multi-component systems is a major asset to numerically explore new alloys. Finally, our experimental work shows that Si can be accepted into the tetragonal $\text{Al}_3(\text{Zr},\text{Ti})$ -based intermetallics. This opens up an opportunity to improve the model of this solid solution of FactSage in further research.

8.1 Summary of works

- Parametrization of Zr, Al-Cu, Al-Cr, and Al-Ti-Zr interatomic potentials using the modified embedded atom method (MEAM) potential formalism.
- Exploration of force field models based on pairwise interactions to metallic solution modeling.
- Solidification studies for Al, Al-Cr, and Al-Zr-Ti systems.
- Synthesis and characterization of $\text{Al}_3\text{Ti-D0}_{22}$ and $\text{Al}_3\text{Zr-D0}_{23}$ intermetallics using a PoDFA-based technology.

8.2 Limitations

Current time and length scales made it difficult for using MD for the prediction of intermetallic primary phases in metallic systems. For the experimentally explored alloys (Al-Si-Zr-Ti), it was difficult to obtain information about the liquidus temperature through Differential Scanning Calorimetry (DSC) measurements. This is because of the low concentration of intermetallics (<10 g intermetallics/ kg of alloy) within the non-filtered specimens.

8.3 Future Research

It is suggested to refine the $\text{Al}_3\text{Zr-D0}_{23}$ $\text{Al}_3\text{Ti-D0}_{22}$ solid solution models in the FTlite database of FactSage considering the data obtained in this work.

REFERENCES

- [1] T. Yen, C. Soong, and P. Tzeng, “Hybrid molecular dynamics-continuum simulation for nano/mesoscale channel flows,” *Microfluidics and Nanofluidics*, vol. 3, no. 6, pp. 665–675, 2007.
- [2] J. Wu, Q. Ruan, S. Chen, C. Meng, Z. Xu, C. Wei, H. Tang, and J. Wang, “Insights into Poisoning Mechanism of Zr by First Principle Calculation on Adhesion Work and Adsorption Energy between TiB_2 , Al_3Ti , and Al_3Zr ,” *Metals*, vol. 12, no. 2, p. 286, 2022.
- [3] W. Ding, X. Liu, X. Zhao, T. Chen, H. Zhang, Y. Cheng, and H. Shi, “Hot Deformation Behavior and Microstructure Evolution of 6063 Aluminum Alloy Modified by Rare Earth Y and Al-Ti-B Master Alloy,” *Materials*, vol. 13, no. 19, p. 4244, 2020.
- [4] M. Rappaz and G. Kurtuldu, “Thermodynamic aspects of homogeneous nucleation enhanced by icosahedral short range order in liquid fcc-type alloys,” *Jom*, vol. 67, no. 8, pp. 1812–1820, 2015.
- [5] G. C. Sosso, J. Chen, S. J. Cox, M. Fitzner, P. Pedevilla, A. Zen, and A. Michaelides, “Crystal nucleation in liquids: Open questions and future challenges in molecular dynamics simulations,” *Chemical reviews*, vol. 116, no. 12, pp. 7078–7116, 2016.
- [6] P. G. Vekilov, “The two-step mechanism of nucleation of crystals in solution,” *Nanoscale*, vol. 2, no. 11, pp. 2346–2357, 2010.
- [7] G. Kurtuldu, P. Jarry, and M. Rappaz, “Influence of Cr on the nucleation of primary Al and formation of twinned dendrites in Al–Zn–Cr alloys: Can icosahedral solid clusters play a role?” *Acta Materialia*, vol. 61, no. 19, pp. 7098–7108, 2013.
- [8] P. M. Larsen, S. Schmidt, and J. Schiøtz, “Robust structural identification via polyhedral template matching,” *Modelling and Simulation in Materials Science and Engineering*, vol. 24, no. 5, p. 055007, may 2016.
- [9] Y. Shibuta, K. Oguchi, T. Takaki, and M. Ohno, “Homogeneous nucleation and microstructure evolution in million-atom molecular dynamics simulation,” *Scientific reports*, vol. 5, no. 1, pp. 1–9, 2015.

- [10] L. Zhan, M. Wu, and X. Qin, "Research on homogeneous nucleation and microstructure evolution of aluminium alloy melt," *Royal Society open science*, vol. 8, no. 8, p. 210501, 2021.
- [11] A. Jain, S. P. Ong, G. Hautier, W. Chen, W. D. Richards, S. Dacek, S. Cholia, D. Gunter, D. Skinner, G. Ceder *et al.*, "Commentary: The Materials Project: A materials genome approach to accelerating materials innovation," *APL materials*, vol. 1, no. 1, p. 011002, 2013.
- [12] C. W. Bale, P. Chartrand, S. Degterov, G. Eriksson, K. Hack, R. B. Mahfoud, J. Melançon, A. Pelton, and S. Petersen, "Factsage thermochemical software and databases," *Calphad*, vol. 26, no. 2, pp. 189–228, 2002.
- [13] J. Murray, "The Ti- Zr (Titanium-Zirconium) system," *Bulletin of Alloy Phase Diagrams*, vol. 2, no. 2, pp. 197–201, 1981.
- [14] N. Jakse and A. Pasturel, "Local order of liquid and supercooled zirconium by Ab Initio Molecular Dynamics," *Physical review letters*, vol. 91, no. 19, p. 195501, 2003.
- [15] T. Schenk, D. Holland-Moritz, V. Simonet, R. Bellissent, and D. Herlach, "Icosahedral short-range order in deeply undercooled metallic melts," *Physical review letters*, vol. 89, no. 7, p. 075507, 2002.
- [16] U. Stolz, I. Arpshofen, F. Sommer, and B. Predel, "Determination of the enthalpy of mixing of liquid alloys using a high-temperature mixing calorimeter," *Journal of phase equilibria*, vol. 14, no. 4, pp. 473–478, 1993.
- [17] D. Kanibolotsky, O. Bieloborodova, N. Kotova, and V. Lisnyak, "Thermodynamic properties of liquid Al-Si and Al-Cu alloys," *Journal of thermal analysis and calorimetry*, vol. 70, no. 3, pp. 975–983, 2002.
- [18] I. Gizenko, S. Kileso, B. Yemlin, and A. Zavyalov, "Partial and Integral Enthalpies of the Formation of Molten Copper Alloys with Silicon and Aluminum," *Izv. V. U. Z. Tsvetn. Metall.*, no. 3, pp. 39–41, 1983.
- [19] V. Sandakov, Y. O. Esin, P. Gel'd, and V. Shantarin, "Heat of Formation of Liquid Copper-Aluminum Alloy," *Zhurnal Fizicheskoi Khimii*, vol. 45, no. 8, pp. 2030–2032, 1971.
- [20] Z. Liu, Q. Han, Y. Guo, J. Lang, D. Shi, Y. Zhang, Q. Huang, H. Deng, F. Gao, B. Sun *et al.*, "Development of interatomic potentials for Fe-Cr-Al alloy with the particle

- swarm optimization method,” *Journal of Alloys and Compounds*, vol. 780, pp. 881–887, 2019.
- [21] P. Saltykov, V. Witusiewicz, I. Arpshofen, H. Seifert, and F. Aldinger, “Enthalpy of mixing of liquid Al-Cr and Cr-Ni alloys,” *Journal of Materials Science & Technology*, vol. 18, no. 2, pp. 167–170, 2002.
- [22] V. Sudavtsova, N. Sharkina, and A. Shuvalov, “Thermodynamic properties of liquid binary Al-Cr (Ni) alloys,” *Rasplavy*, vol. 1, pp. 97–99, 1990.
- [23] Y. O. Esin, N. Bobrov, M. Petrushevskij, and P. Gel’d, “Formation enthalpy of liquid aluminium alloys with titanium and zirconium,” *Izvestiya Akademii Nauk SSSR, Metall*, pp. 104–109, 1974.
- [24] V. Sudavtsova, G. Batalin, and V. Tutevich, “Thermodynamic Properties of Molten Binary Alloys in Systems Al-Zr(Nb, Mo).(Translation),” *Russ. Metall.*, no. 5, pp. 183–185, 1985.
- [25] V. Witusiewicz, U. K. Stolz, I. Arpshofen, and F. Sommer, “Thermodynamics of liquid Al-Cu-Zr alloys,” *Zeitschrift fuer Metallkunde*, vol. 89, no. 10, pp. 704–713, 1998.
- [26] A. Stukowski, “Visualization and analysis of atomistic simulation data with OVITO—the Open Visualization Tool,” *Modelling and simulation in materials science and engineering*, vol. 18, no. 1, p. 015012, 2009.
- [27] J.-R. Castillo-Sánchez, A. Rincent, A.-E. Gheribi, and J.-P. Harvey, “On the transferability of classical pairwise additive atomistic force field to the description of unary and multi-component systems: Applications to the solidification of Al-based alloys,” *Submitted to Physical Chemistry Chemical Physics*, 2022.
- [28] M. Fine, G. Ghosh, D. Isheim, S. Vaynman, K. Knipling, and J. Liu, “Alloy design of nanoscale precipitation strengthened alloys: Design of a heat treatable aluminum alloy useful to 400 °C,” *Northwestern University, Department of Materials Science and Engineering, McCormick School of Engineering and Applied Science*, 2006.
- [29] S. Han, S. Park, J.-S. Huh, Z.-H. Lee, and H. Lee, “Lattice matching of D0₂₃ and D0₂₂ phases in Al-6at.%(Ti, V, Zr) systems,” *Materials Science and Engineering: A*, vol. 230, no. 1-2, pp. 100–106, 1997.
- [30] S. Otarawanna and A. Dahle, “6 - Casting of aluminium alloys,” in *Fundamentals of Aluminium Metallurgy*, ser. Woodhead Publishing Series in Metals and Surface

- Engineering, R. Lumley, Ed. Woodhead Publishing, 2011, pp. 141–154. [Online]. Available: <https://www.sciencedirect.com/science/article/pii/B9781845696542500067>
- [31] B. Cantor and K. O'Reilly, "Solidification and casting," 2016.
- [32] American Foundry Society. (2022) About metalcasting. [Online]. Available: <https://www.afsinc.org/about-metalcasting>
- [33] R. Rana, R. Purohit, and S. Das, "Reviews on the influences of alloying elements on the microstructure and mechanical properties of aluminum alloys and aluminum alloy composites," *International Journal of Scientific and research publications*, vol. 2, no. 6, pp. 1–7, 2012.
- [34] Z. Yin, Q. Pan, Y. Zhang, and F. Jiang, "Effect of minor Sc and Zr on the microstructure and mechanical properties of Al–Mg based alloys," *Materials Science and Engineering: A*, vol. 280, no. 1, pp. 151–155, 2000.
- [35] J. Hwang, H. Doty, and M. Kaufman, "The effects of mn additions on the microstructure and mechanical properties of Al–Si–Cu casting alloys," *Materials Science and Engineering: A*, vol. 488, no. 1-2, pp. 496–504, 2008.
- [36] P. Spencer, "A brief history of CALPHAD," *Calphad*, vol. 32, no. 1, pp. 1–8, 2008.
- [37] A. D. Pelton, P. Koukkari, R. Pajarre, and G. Eriksson, "Para-equilibrium phase diagrams," *The Journal of Chemical Thermodynamics*, vol. 72, pp. 16–22, 2014.
- [38] A. D. Pelton, G. Eriksson, and C. W. Bale, "Scheil–Gulliver constituent diagrams," *Metallurgical and Materials Transactions A*, vol. 48, no. 6, pp. 3113–3129, 2017.
- [39] M. Zamani, L. Morini, L. Ceschini, and S. Seifeddine, "The role of transition metal additions on the ambient and elevated temperature properties of Al–Si alloys," *Materials Science and Engineering: A*, vol. 693, pp. 42–50, 2017.
- [40] R. Gupta, D. Fabijanic, T. Dorin, Y. Qiu, J. Wang, and N. Birbilis, "Simultaneous improvement in the strength and corrosion resistance of Al via high-energy ball milling and Cr alloying," *Materials & Design*, vol. 84, pp. 270–276, 2015.
- [41] M. Karpets, Y. V. Milman, O. Barabash, N. Korzhova, O. Senkov, D. Miracle, T. Legkaya, and I. Voskoboynik, "The influence of Zr alloying on the structure and properties of Al₃Ti," *Intermetallics*, vol. 11, no. 3, pp. 241–249, 2003.

- [42] A. Mahata, T. Mukhopadhyay, and M. A. Zaeem, “Modified embedded-atom method interatomic potentials for Al-Cu, Al-Fe and Al-Ni binary alloys: From room temperature to melting point,” *Computational Materials Science*, vol. 201, p. 110902, 2022.
- [43] F. Apostol and Y. Mishin, “Interatomic potential for the Al-Cu system,” *Physical Review B*, vol. 83, no. 5, p. 054116, 2011.
- [44] W. Wang, J. Han, H. Fang, J. Wang, Y. Liang, S. Shang, Y. Wang, X. Liu, L. Kecskes, S. Mathaudhu *et al.*, “Anomalous structural dynamics in liquid Al₈₀Cu₂₀: An ab initio molecular dynamics study,” *Acta Materialia*, vol. 97, pp. 75–85, 2015.
- [45] F. Crossley and L. Mondolfo, “Mechanism of grain refinement in aluminum alloys,” *JOM*, vol. 3, no. 12, pp. 1143–1148, 1951.
- [46] F. Wang, D. Qiu, Z.-L. Liu, J. A. Taylor, M. A. Easton, and M.-X. Zhang, “The grain refinement mechanism of cast aluminium by zirconium,” *Acta materialia*, vol. 61, no. 15, pp. 5636–5645, 2013.
- [47] G. Salloum-Abou-Jaoude, D. Eskin, C. Barbatti, P. Jarry, M. Jarrett, and Z. Fan, “Effect of ultrasonic processing on a direct chill cast AA6082 aluminium alloy,” in *Light Metals 2017*. Springer, 2017, pp. 997–1003.
- [48] Z. Chen and K. Yan, “Grain refinement of commercially pure aluminum with addition of Ti and Zr elements based on crystallography orientation,” *Scientific Reports*, vol. 10, no. 1, pp. 1–8, 2020.
- [49] W. Haupin, “Aluminum,” in *Encyclopedia of Physical Science and Technology (Third Edition)*, third edition ed., R. A. Meyers, Ed. New York: Academic Press, 2003, pp. 495–518. [Online]. Available: <https://www.sciencedirect.com/science/article/pii/B0122274105000223>
- [50] B. Sundman, Q. Chen, and Y. Du, “A review of Calphad modeling of ordered phases,” *Journal of Phase Equilibria and Diffusion*, vol. 39, no. 5, pp. 678–693, 2018.
- [51] S. Plimpton, “Fast parallel algorithms for short-range molecular dynamics,” *Journal of computational physics*, vol. 117, no. 1, pp. 1–19, 1995.
- [52] J. Hafner, “Ab-initio simulations of materials using VASP: Density-functional theory and beyond,” *Journal of computational chemistry*, vol. 29, no. 13, pp. 2044–2078, 2008.
- [53] B.-J. Lee and M. Baskes, “Second nearest-neighbor modified embedded-atom-method potential,” *Physical Review B*, vol. 62, no. 13, p. 8564, 2000.

- [54] S. Capuzzi and G. Timelli, "Preparation and melting of scrap in aluminum recycling: A review," *Metals*, vol. 8, no. 4, p. 249, 2018.
- [55] D. Varshney and K. Kumar, "Application and use of different aluminium alloys with respect to workability, strength and welding parameter optimization," *Ain Shams Engineering Journal*, vol. 12, no. 1, pp. 1143–1152, 2021.
- [56] E. Georgantzia, M. Gkantou, and G. S. Kamaris, "Aluminium alloys as structural material: A review of research," *Engineering Structures*, vol. 227, p. 111372, 2021.
- [57] P. G. Sheasby, R. Pinner, and S. Wernick, *The surface treatment and finishing of aluminium and its alloys*. ASM international Materials Park, OH, 2001, vol. 1.
- [58] O. Lunder, J. Walmsley, P. Mack, and K. Nisancioglu, "Formation and characterisation of a chromate conversion coating on AA6060 aluminium," *Corrosion science*, vol. 47, no. 7, pp. 1604–1624, 2005.
- [59] C. J. Donahue and J. A. Exline, "Anodizing and coloring aluminum alloys," *Journal of Chemical Education*, vol. 91, no. 5, pp. 711–715, 2014.
- [60] D. W. J. Harrison, "Creep of Non-Ferrous Metals," in *Encyclopedia of Materials: Metals and Alloys*, F. G. Caballero, Ed. Oxford: Elsevier, 2022, pp. 494–504. [Online]. Available: <https://www.sciencedirect.com/science/article/pii/B9780128197264000855>
- [61] P. Mallick, "Chapter 1 - overview," in *Materials, Design and Manufacturing for Lightweight Vehicles (Second Edition)*, second edition ed., ser. Woodhead Publishing in Materials, P. Mallick, Ed. Woodhead Publishing, 2021, pp. 1–36. [Online]. Available: <https://www.sciencedirect.com/science/article/pii/B978012818712800001X>
- [62] K. Nakajima, O. Takeda, T. Miki, K. Matsubae, S. Nakamura, and T. Nagasaka, "Thermodynamic analysis of contamination by alloying elements in aluminum recycling," *Environmental science & technology*, vol. 44, no. 14, pp. 5594–5600, 2010.
- [63] E. Starke, "Aluminum alloys: Alloy, heat treatment, and temper designation," *Encyclopedia of Materials: Science and Technology*, pp. 106–107, 2011.
- [64] M. S. Kenevisi, Y. Yu, and F. Lin, "A review on additive manufacturing of Al–Cu (2xxx) aluminium alloys, processes and defects," *Materials Science and Technology*, vol. 37, no. 9, pp. 805–829, 2021.

- [65] D. Culliton, A. Betts, and D. Kennedy, "Impact of intermetallic precipitates on the tribological and/or corrosion performance of cast aluminium alloys: a short review," *International Journal of Cast Metals Research*, vol. 26, no. 2, pp. 65–71, 2013.
- [66] F. Tariq, N. Naz, R. A. Baloch *et al.*, "Characterization of material properties of 2xxx series al-alloys by non destructive testing techniques," *Journal of Nondestructive Evaluation*, vol. 31, no. 1, pp. 17–33, 2012.
- [67] P. Rambabu, N. Eswara Prasad, V. Kutumbarao, and R. Wanhill, "Aluminium alloys for aerospace applications," *Aerospace materials and material technologies*, pp. 29–52, 2017.
- [68] T. H. da Silva, E. B. Nelson, I. Williamson, C. M. Efav, E. Sapper, M. F. Hurley, and L. Li, "First-principles surface interaction studies of aluminum-copper and aluminum-copper-magnesium secondary phases in aluminum alloys," *Applied Surface Science*, vol. 439, pp. 910–918, 2018.
- [69] K. Biswas and K. Chattopadhyay, "Formation of ω -Al₁₇Cu₂Fe phase during laser processing of quasicrystal-forming Al–Cu–Fe alloy," *Philosophical magazine letters*, vol. 88, no. 3, pp. 219–230, 2008.
- [70] L. Bindi, P. J. Steinhardt, N. Yao, and P. J. Lu, "Icosahedrite, Al₆₃Cu₂₄Fe₁₃, the first natural quasicrystal," *American Mineralogist*, vol. 96, no. 5-6, pp. 928–931, 2011.
- [71] L. Zhu, S. Soto-Medina, W. Cuadrado-Castillo, R. G. Hennig, and M. V. Manuel, "New experimental studies on the phase diagram of the Al-Cu-Fe quasicrystal-forming system," *Materials & Design*, vol. 185, p. 108186, 2020.
- [72] C. Dong, Q. Zhang, D. Wang, and Y. Wang, "Al-Cu approximants in the alloy," *The European Physical Journal B-Condensed Matter and Complex Systems*, vol. 6, no. 1, pp. 25–32, 1998.
- [73] S. Wang and M. Starink, "Precipitates and intermetallic phases in precipitation hardening Al–Cu–Mg–(Li) based alloys," *International Materials Reviews*, vol. 50, no. 4, pp. 193–215, 2005.
- [74] J. Huang, "On the crystal structure of the T1 phase in Al-Li-Cu alloys," *Scr. Metall. Mater*, vol. 27, no. 6, pp. 755–760, 1992.
- [75] J. Rao, E. J. Payton, C. Somsen, K. Neuking, G. Eggeler, A. Kostka, and J. F. dos Santos, "Where Does the Lithium Go?—A Study of the Precipitates in the Stir Zone

- of a Friction Stir Weld in a Li-containing 2xxx Series Al Alloy,” *Advanced engineering materials*, vol. 12, no. 4, pp. 298–303, 2010.
- [76] W. Shuncaï, L. Chunzhi, and Y. Minggao, “Determination of structure of $\text{Al}_{20}\text{Cu}_2\text{Mn}_3$ phase in Al-Cu-Mn alloys,” *Materials research bulletin*, vol. 24, no. 10, pp. 1267–1270, 1989.
- [77] A. K. Shriwas and V. C. Kale, “Impact of aluminum alloys and microstructures on engineering properties review,” *IOSR Journal of Mechanical and Civil Engineering*, vol. 13, no. 3, pp. 16–22, 2016.
- [78] S. N. Khangholi, M. Javidani, A. Maltais, and X. G. Chen, “Review on recent progress in Al-Mg-Si 6xxx conductor alloys,” *Journal of Materials Research*, pp. 1–22, 2022.
- [79] S. Kairy, P. Rometsch, K. Diao, J. Nie, C. Davies, and N. Birbilis, “Exploring the electrochemistry of 6xxx series aluminium alloys as a function of Si to Mg ratio, Cu content, ageing conditions and microstructure,” *Electrochimica Acta*, vol. 190, pp. 92–103, 2016.
- [80] J. G. Kaufman, “Understanding wrought and cast aluminum alloy designations,” 2013.
- [81] A. Handbook, “Introduction to Aluminum-Silicon Casting Alloys,” *Volume*, vol. 2, pp. 1–9, 2004.
- [82] M. Haghshenas and J. Jamali, “Assessment of circumferential cracks in hypereutectic Al-Si clutch housings,” *Case studies in engineering failure analysis*, vol. 8, pp. 11–20, 2017.
- [83] J. Roger, F. Bosselet, and J. Viala, “X-rays structural analysis and thermal stability studies of the ternary compound $\alpha\text{-AlFeSi}$,” *Journal of Solid State Chemistry*, vol. 184, no. 5, pp. 1120–1128, 2011.
- [84] J. Barbosa, H. Puga, J. Oliveira, S. Ribeiro, and M. Prokic, “Physical modification of intermetallic phases in Al-Si-Cu alloys,” *Materials Chemistry and Physics*, vol. 148, no. 3, pp. 1163–1170, 2014. [Online]. Available: <https://www.sciencedirect.com/science/article/pii/S0254058414006233>
- [85] H. Becker, B. Fankhänel, C. Voigt, A. Charitos, M. Stelter, C. G. Aneziris, and A. Leineweber, “Interaction of Fe-Containing, secondary Al-Si Alloy with Oxide and Carbon-Containing Ceramics for Fe Removal,” *Advanced Engineering Materials*, vol. 24, no. 2, p. 2100595, 2022.

- [86] S. Cui and I.-H. Jung, "Thermodynamic assessments of the cr-si and al-cr-si systems," *Journal of Alloys and Compounds*, vol. 708, pp. 887–902, 2017.
- [87] H. Ghandvar, K. A. Jabbar, M. H. Idris, N. Ahmad, M. H. Jahare, S. S. R. Koloor, and M. Petr, "Influence of barium addition on the formation of primary mg₂si crystals from Al–Mg–Si melts," *Journal of Materials Research and Technology*, vol. 11, pp. 448–465, 2021.
- [88] S. Foss, A. Olsen, C. Simensen, and J. Taftø, "Determination of the crystal structure of the π -AlFeMgSi phase using symmetry- and site-sensitive electron microscope techniques," *Acta Crystallographica Section B: Structural Science*, vol. 59, no. 1, pp. 36–42, 2003.
- [89] J. Shin, T. Kim, D. Kim, D. Kim, and K. Kim, "Castability and mechanical properties of new 7xxx aluminum alloys for automotive chassis/body applications," *Journal of Alloys and Compounds*, vol. 698, pp. 577–590, 2017.
- [90] S. S. Ebrahimi and M. Emamy, "Effects of Al–5Ti–1B and Al–5Zr master alloys on the structure, hardness and tensile properties of a highly alloyed aluminum alloy," *Materials & Design*, vol. 31, no. 1, pp. 200–209, 2010.
- [91] P. Cizek, "Electron microscopy investigation of the TiBAl and TiAl grain refiner master alloys," in *Journal of Physics: Conference Series*, vol. 26, no. 1. IOP Publishing, 2006, p. 025.
- [92] G. V. Kumar, B. Murty, and M. Chakraborty, "Grain refinement response of lm25 alloy towards Al–Ti–c and Al–Ti–B grain refiners," *Journal of Alloys and Compounds*, vol. 472, no. 1-2, pp. 112–120, 2009.
- [93] R.-G. Guan and D. Tie, "A review on grain refinement of aluminum alloys: progresses, challenges and prospects," *Acta Metallurgica Sinica (English Letters)*, vol. 30, no. 5, pp. 409–432, 2017.
- [94] P. Mohanty and J. Gruzleski, "Mechanism of grain refinement in aluminium," *Acta Metallurgica et Materialia*, vol. 43, no. 5, pp. 2001–2012, 1995.
- [95] A. Cornish, "The influence of boron on the mechanism of grain refinement in dilute aluminium-titanium alloys," *Metal Science*, vol. 9, no. 1, pp. 477–484, 1975.
- [96] H. Yang, Z. Qian, H. Chen, X. Zhao, G. Han, W. Du, X. Nie, K. Zhao, G. Liu, Q. Sun *et al.*, "A new insight into heterogeneous nucleation mechanism of Al by non-stoichiometric TiC_x," *Acta Materialia*, p. 117977, 2022.

- [97] E. Clouet, J.-M. Sanchez, and C. Sigli, “First-principles study of the solubility of Zr in Al,” *Physical Review B*, vol. 65, no. 9, p. 094105, 2002.
- [98] P. Jarry and M. Rappaz, “Recent advances in the metallurgy of aluminium alloys. Part i: Solidification and casting,” *Comptes Rendus Physique*, vol. 19, no. 8, pp. 672–687, 2018.
- [99] J.-G. Jung, Y.-H. Cho, S.-D. Kim, S.-B. Kim, S.-H. Lee, K. Song, K. Euh, and J.-M. Lee, “Mechanism of ultrasound-induced microstructure modification in Al–Zr alloys,” *Acta Materialia*, vol. 199, pp. 73–84, 2020.
- [100] L. Zhang, D. Eskin, and L. Katgerman, “Influence of ultrasonic melt treatment on the formation of primary intermetallics and related grain refinement in aluminum alloys,” *Journal of materials science*, vol. 46, no. 15, pp. 5252–5259, 2011.
- [101] D. Kashchiev, *Nucleation*. Elsevier, 2000.
- [102] L. R. Gómez, N. A. García, V. Vitelli, J. Lorenzana, and D. A. Vega, “Phase nucleation in curved space,” *Nature communications*, vol. 6, no. 1, pp. 1–9, 2015.
- [103] L. Baeckerud and M. Johnsson, “The relative importance of nucleation and growth mechanisms to control grain size in various aluminum alloys,” 1996.
- [104] P. PRANGNELL, “3.03 - Precipitation Behaviors in MMCs,” in *Comprehensive Composite Materials*, A. Kelly and C. Zweben, Eds. Oxford: Pergamon, 2000, pp. 61–90. [Online]. Available: <https://www.sciencedirect.com/science/article/pii/B0080429939000036>
- [105] “1 - INTRODUCTION,” in *Handbook of Nucleating Agents*, G. Wypych, Ed. ChemTec Publishing, 2016, pp. 1–3. [Online]. Available: <https://www.sciencedirect.com/science/article/pii/B9781895198935500034>
- [106] S. Karthika, T. Radhakrishnan, and P. Kalaichelvi, “A review of classical and nonclassical nucleation theories,” *Crystal Growth & Design*, vol. 16, no. 11, pp. 6663–6681, 2016.
- [107] Y. Wang, C. Fang, L. Zhou, T. Hashimoto, X. Zhou, Q. Ramasse, and Z. Fan, “Mechanism for Zr poisoning of Al-Ti-B based grain refiners,” *Acta materialia*, vol. 164, pp. 428–439, 2019.

- [108] M. Easton, M. Qian, A. Prasad, and D. StJohn, "Recent advances in grain refinement of light metals and alloys," *Current Opinion in Solid State and Materials Science*, vol. 20, no. 1, pp. 13–24, 2016.
- [109] T. Guan, Z. Zhang, Y. Bai, M. He, H. Zheng, H. Zhao, X. Li, and P. Wang, "The influence of Inter-cooling and electromagnetic stirring above liquidus on the formation of primary Al_3Zr and grain refinement in an Al-0.2% Zr alloy," *Materials*, vol. 12, no. 1, p. 22, 2019.
- [110] A. Cibula, "The grain refinement of aluminium alloy castings by additions of titanium and boron," *J. Inst. Metals*, vol. 80, 1951.
- [111] P. Schumacher, A. Greer, J. Worth, P. Evans, M. Kearns, P. Fisher, and A. Green, "New studies of nucleation mechanisms in aluminium alloys: implications for grain refinement practice," *Materials science and technology*, vol. 14, no. 5, pp. 394–404, 1998.
- [112] X. Wang, J. Song, W. Vian, H. Ma, and Q. Han, "The interface of TiB_2 and Al_3Ti in molten aluminum," *Metallurgical and materials transactions B*, vol. 47, no. 6, pp. 3285–3290, 2016.
- [113] Y. Cui, D. King, A. Horsfield, and C. Gourlay, "Solidification orientation relationships between Al_3Ti and TiB_2 ," *Acta Materialia*, vol. 186, pp. 149–161, 2020. [Online]. Available: <https://www.sciencedirect.com/science/article/pii/S1359645419308420>
- [114] F. Wang, Z. Liu, D. Qiu, J. A. Taylor, M. A. Easton, and M.-X. Zhang, "Revisiting the role of peritectics in grain refinement of Al alloys," *Acta Materialia*, vol. 61, no. 1, pp. 360–370, 2013. [Online]. Available: <https://www.sciencedirect.com/science/article/pii/S1359645412007185>
- [115] A. Greer, "Grain refinement in rapidly solidified alloys," *Materials Science and Engineering: A*, vol. 133, pp. 16–21, 1991.
- [116] T. Pinomaa and N. Provatas, "Quantitative phase field modeling of solute trapping and continuous growth kinetics in quasi-rapid solidification," *Acta Materialia*, vol. 168, pp. 167–177, 2019.
- [117] Z. Hou, K. Dong, Z. Tian, R. Liu, Z. Wang, and J. Wang, "Cooling rate dependence of solidification for liquid aluminium: a large-scale molecular dynamics simulation study," *Physical Chemistry Chemical Physics*, vol. 18, no. 26, pp. 17 461–17 469, 2016.

- [118] M. Mendeleev, M. Kramer, C. A. Becker, and M. Asta, “Analysis of semi-empirical interatomic potentials appropriate for simulation of crystalline and liquid Al and Cu,” *Philosophical Magazine*, vol. 88, no. 12, pp. 1723–1750, 2008.
- [119] Q. Zhang, J. Wang, S. Tang, Y. Wang, J. Li, W. Zhou, and Z. Wang, “Molecular dynamics investigation of the local structure in iron melts and its role in crystal nucleation during rapid solidification,” *Physical Chemistry Chemical Physics*, vol. 21, no. 8, pp. 4122–4135, 2019.
- [120] M. Mendeleev, S. Han, D. Srolovitz, G. Ackland, D. Sun, and M. Asta, “Development of new interatomic potentials appropriate for crystalline and liquid iron,” *Philosophical magazine*, vol. 83, no. 35, pp. 3977–3994, 2003.
- [121] M. Papanikolaou, K. Salonitis, M. Jolly, and M. Frank, “Large-scale molecular dynamics simulations of homogeneous nucleation of pure aluminium,” *Metals*, vol. 9, no. 11, p. 1217, 2019.
- [122] Y. Sun, H. Song, F. Zhang, L. Yang, Z. Ye, M. I. Mendeleev, C.-Z. Wang, and K.-M. Ho, “Overcoming the time limitation in molecular dynamics simulation of crystal nucleation: A persistent-embryo approach,” *Physical review letters*, vol. 120, no. 8, p. 085703, 2018.
- [123] T. Fujinaga, Y. Watanabe, and Y. Shibuta, “Nucleation dynamics in Al solidification with Al-Ti refiners by molecular dynamics simulation,” *Computational Materials Science*, vol. 182, p. 109763, 2020.
- [124] A. Pasturel and N. Jakse, “Influence of cr on local order and dynamic properties of liquid and undercooled al–zn alloys,” *The Journal of Chemical Physics*, vol. 146, no. 18, p. 184502, 2017.
- [125] A. Mahata and M. A. Zaeem, “Effects of solidification defects on nanoscale mechanical properties of rapid directionally solidified Al-Cu alloy: A large scale molecular dynamics study,” *Journal of Crystal Growth*, vol. 527, p. 125255, 2019.
- [126] S. C. C. Prado, J. P. Rino, and E. D. Zanotto, “Successful test of the classical nucleation theory by molecular dynamic simulations of BaS,” *Computational Materials Science*, vol. 161, pp. 99–106, 2019.
- [127] S. Nosé, “A unified formulation of the constant temperature molecular dynamics methods,” *The Journal of chemical physics*, vol. 81, no. 1, pp. 511–519, 1984.

- [128] W. G. Hoover, "Canonical dynamics: Equilibrium phase-space distributions," *Physical review A*, vol. 31, no. 3, p. 1695, 1985.
- [129] S. Nosé, "A molecular dynamics method for simulations in the canonical ensemble," *Molecular physics*, vol. 52, no. 2, pp. 255–268, 1984.
- [130] W. G. Hoover, "Constant-pressure equations of motion," *Physical Review A*, vol. 34, no. 3, p. 2499, 1986.
- [131] D. Frenkel and B. Smit, *Understanding molecular simulation: from algorithms to applications*. Elsevier, 2001, vol. 1.
- [132] S. V. Sukhomlinov and M. H. Müser, "Determination of accurate, mean bond lengths from radial distribution functions," *The Journal of chemical physics*, vol. 146, no. 2, p. 024506, 2017.
- [133] A. Stukowski, "Visualization and analysis of atomistic simulation data with OVITO—the Open Visualization Tool," *Modelling and Simulation in Materials Science and Engineering*, vol. 18, no. 1, p. 015012, dec 2009.
- [134] D. Faken and H. Jónsson, "Systematic analysis of local atomic structure combined with 3D computer graphics," *Computational Materials Science*, vol. 2, no. 2, pp. 279–286, 1994.
- [135] L. Verlet, "Computer" experiments" on classical fluids. i. Thermodynamical properties of Lennard-Jones molecules," *Physical review*, vol. 159, no. 1, p. 98, 1967.
- [136] V. Borovikov, M. I. Mendeleev, and A. H. King, "Effects of stable and unstable stacking fault energy on dislocation nucleation in nano-crystalline metals," *Modelling and Simulation in Materials Science and Engineering*, vol. 24, no. 8, p. 085017, 2016.
- [137] M. Islam, M. S. H. Thakur, S. Mojumder, and M. N. Hasan, "Extraction of material properties through multi-fidelity deep learning from molecular dynamics simulation," *Computational Materials Science*, vol. 188, p. 110187, 2021.
- [138] J. C. Jo and B. C. Kim, "Determination of proper time step for molecular dynamics simulation," *Bulletin of the Korean Chemical Society*, vol. 21, no. 4, pp. 419–424, 2000.
- [139] A. LEACH, "Principle and applications of Molecular Modeling," 1996.
- [140] F. C. Frank, "Supercooling of liquids," *Proceedings of the Royal Society of London. Series A. Mathematical and Physical Sciences*, vol. 215, no. 1120, pp. 43–46, 1952.

- [141] J. Wannasin, D. Schwam, and J. Wallace, "Evaluation of methods for metal cleanliness assessment in die casting," *Journal of materials processing technology*, vol. 191, no. 1-3, pp. 242–246, 2007.
- [142] B. D. Cullity, *Elements of X-ray Diffraction*. Addison-Wesley Publishing, 1956.
- [143] B. Zhou, B. Liu, and S. Zhang, "The advancement of 7xxx series aluminum alloys for aircraft structures: A review," *Metals*, vol. 11, no. 5, p. 718, 2021.
- [144] B. MacDonald, Z. Fu, B. Zheng, W. Chen, Y. Lin, F. Chen, L. Zhang, J. Ivanisenko, Y. Zhou, H. Hahn *et al.*, "Recent progress in high entropy alloy research," *Jom*, vol. 69, no. 10, pp. 2024–2031, 2017.
- [145] S. Intiaz, I. S. Amiin, Y. Xu, T. Kennedy, C. Blackman, and K. M. Ryan, "Progress and perspectives on alloying-type anode materials for advanced potassium-ion batteries," *Materials Today*, vol. 48, pp. 241–269, 2021.
- [146] J. L. Cann, A. De Luca, D. C. Dunand, D. Dye, D. B. Miracle, H. S. Oh, E. A. Olivetti, T. M. Pollock, W. J. Poole, R. Yang *et al.*, "Sustainability through alloy design: Challenges and opportunities," *Progress in Materials Science*, vol. 117, p. 100722, 2021.
- [147] I. Choudhury and M. El-Baradie, "Machinability of nickel-base super alloys: a general review," *Journal of Materials Processing Technology*, vol. 77, no. 1-3, pp. 278–284, 1998.
- [148] H. Long, S. Mao, Y. Liu, Z. Zhang, and X. Han, "Microstructural and compositional design of Ni-based single crystalline superalloys—A review," *Journal of Alloys and Compounds*, vol. 743, pp. 203–220, 2018.
- [149] R. Darolia, "Development of strong, oxidation and corrosion resistant nickel-based superalloys: critical review of challenges, progress and prospects," *International materials reviews*, vol. 64, no. 6, pp. 355–380, 2019.
- [150] M.-H. Tsai and J.-W. Yeh, "High-entropy alloys: a critical review," *Materials Research Letters*, vol. 2, no. 3, pp. 107–123, 2014.
- [151] M. C. Gao, C. Zhang, P. Gao, F. Zhang, L. Ouyang, M. Widom, and J. A. Hawk, "Thermodynamics of concentrated solid solution alloys," *Current Opinion in Solid State and Materials Science*, vol. 21, no. 5, pp. 238–251, 2017.

- [152] L.-Y. Tian, G. Wang, J. S. Harris, D. L. Irving, J. Zhao, and L. Vitos, “Alloying effect on the elastic properties of refractory high-entropy alloys,” *Materials & Design*, vol. 114, pp. 243–252, 2017.
- [153] J. Allison, D. Backman, and L. Christodoulou, “Integrated computational materials engineering: a new paradigm for the global materials profession,” *Jom*, vol. 58, no. 11, pp. 25–27, 2006.
- [154] J.-W. Yeh, “Alloy design strategies and future trends in high-entropy alloys,” *Jom*, vol. 65, no. 12, pp. 1759–1771, 2013.
- [155] J. Neugebauer and T. Hickel, “Density functional theory in materials science,” *Wiley Interdisciplinary Reviews: Computational Molecular Science*, vol. 3, no. 5, pp. 438–448, 2013.
- [156] C. J. Cramer and D. G. Truhlar, “Density functional theory for transition metals and transition metal chemistry,” *Physical Chemistry Chemical Physics*, vol. 11, no. 46, pp. 10 757–10 816, 2009.
- [157] D. Dickel, S. Mun, M. Baskes, S. Gwaltney, R. K. Prabhu, and M. F. Horstemeyer, “Density functional theory and bridging to classical interatomic force fields,” in *Multi-scale Biomechanical Modeling of the Brain*. Elsevier, 2022, pp. 39–52.
- [158] J.-P. Harvey, A. Gheribi, and P. Chartrand, “Accurate determination of the gibbs energy of Cu–Zr melts using the thermodynamic integration method in Monte Carlo simulations,” *The Journal of chemical physics*, vol. 135, no. 8, p. 084502, 2011.
- [159] Y. Huang, J. Kang, W. A. Goddard III, and L.-W. Wang, “Density functional theory based neural network force fields from energy decompositions,” *Physical Review B*, vol. 99, no. 6, p. 064103, 2019.
- [160] M. S. Daw and M. I. Baskes, “Embedded-atom method: Derivation and application to impurities, surfaces, and other defects in metals,” *Physical Review B*, vol. 29, no. 12, p. 6443, 1984.
- [161] M. Finnis and J. Sinclair, “A simple empirical N-body potential for transition metals,” *Philosophical Magazine A*, vol. 50, no. 1, pp. 45–55, 1984.
- [162] F. Cleri and V. Rosato, “Tight-binding potentials for transition metals and alloys,” *Physical Review B*, vol. 48, no. 1, p. 22, 1993.

- [163] M. I. Baskes, “Modified embedded-atom potentials for cubic materials and impurities,” *Physical review B*, vol. 46, no. 5, p. 2727, 1992.
- [164] B.-J. Lee, M. Baskes, H. Kim, and Y. K. Cho, “Second nearest-neighbor modified embedded atom method potentials for bcc transition metals,” *Physical Review B*, vol. 64, no. 18, p. 184102, 2001.
- [165] B.-J. Lee, J.-H. Shim, and M. Baskes, “Semiempirical atomic potentials for the fcc metals Cu, Ag, Au, Ni, Pd, Pt, Al, and Pb based on first and second nearest-neighbor modified embedded atom method,” *Physical Review B*, vol. 68, no. 14, p. 144112, 2003.
- [166] Y.-M. Kim, B.-J. Lee, and M. Baskes, “Modified embedded-atom method interatomic potentials for Ti and Zr,” *Physical Review B*, vol. 74, no. 1, p. 014101, 2006.
- [167] E. C. Do, Y.-H. Shin, and B.-J. Lee, “A modified embedded-atom method interatomic potential for indium,” *Calphad*, vol. 32, no. 1, pp. 82–88, 2008.
- [168] Y.-M. Kim, N. J. Kim, and B.-J. Lee, “Atomistic modeling of pure Mg and Mg–Al systems,” *Calphad*, vol. 33, no. 4, pp. 650–657, 2009.
- [169] H.-S. Jang, K.-M. Kim, and B.-J. Lee, “Modified embedded-atom method interatomic potentials for pure Zn and Mg–Zn binary system,” *Calphad*, vol. 60, pp. 200–207, 2018.
- [170] S.-H. Oh, X.-G. Lu, Q. Chen, and B.-J. Lee, “Pressure dependence of thermodynamic interaction parameters for binary solid solution phases: An atomistic simulation study,” *Calphad*, vol. 75, p. 102342, 2021.
- [171] Y.-K. Kim, W.-S. Jung, and B.-J. Lee, “Modified embedded-atom method interatomic potentials for the Ni–Co binary and the Ni–Al–Co ternary systems,” *Modelling and Simulation in Materials Science and Engineering*, vol. 23, no. 5, p. 055004, 2015.
- [172] Y.-K. Kim, H.-K. Kim, W.-S. Jung, and B.-J. Lee, “Development and application of Ni–Ti and Ni–Al–Ti 2NN-MEAM interatomic potentials for Ni-base superalloys,” *Computational Materials Science*, vol. 139, pp. 225–233, 2017.
- [173] H.-S. Jang, D. Seol, and B.-J. Lee, “Modified embedded-atom method interatomic potentials for Mg–Al–Ca and Mg–Al–Zn ternary systems,” *Journal of Magnesium and Alloys*, vol. 9, no. 1, pp. 317–335, 2021.
- [174] B.-J. Lee, W.-S. Ko, H.-K. Kim, and E.-H. Kim, “The modified embedded-atom method interatomic potentials and recent progress in atomistic simulations,” *Calphad*, vol. 34, no. 4, pp. 510–522, 2010.

- [175] S. Roy, A. Dutta, and N. Chakraborti, “A novel method of determining interatomic potential for Al and Al-Li alloys and studying strength of Al-Al₃Li interphase using evolutionary algorithms,” *Computational Materials Science*, vol. 190, p. 110258, 2021.
- [176] S. Hu, M. Baskes, M. Stan, and L. Chen, “Atomistic calculations of interfacial energies, nucleus shape and size of θ precipitates in Al-Cu alloys,” *Acta materialia*, vol. 54, no. 18, pp. 4699–4707, 2006.
- [177] B. Jelinek, S. Groh, M. F. Horstemeyer, J. Houze, S.-G. Kim, G. J. Wagner, A. Moitra, and M. I. Baskes, “Modified embedded atom method potential for Al, Si, Mg, Cu, and Fe alloys,” *Physical Review B*, vol. 85, no. 24, p. 245102, 2012.
- [178] S. Schönecker, X. Li, K. Koepernik, B. Johansson, L. Vitos, and M. Richter, “Metastable cubic and tetragonal phases of transition metals predicted by density-functional theory,” *RSC advances*, vol. 5, no. 85, pp. 69 680–69 689, 2015.
- [179] M. Jin, N. Miao, W. Zhao, J. Zhou, Q. Du, and Z. Sun, “Structural stability and mechanical properties of Co₃(Al,M) (M=Ti, V, Cr, Zr, Nb, Mo, Hf, Ta, W) compounds,” *Computational Materials Science*, vol. 148, pp. 27–37, 2018.
- [180] S. Riniker, “Fixed-charge atomistic force fields for molecular dynamics simulations in the condensed phase: an overview,” *Journal of chemical information and modeling*, vol. 58, no. 3, pp. 565–578, 2018.
- [181] E. Lee and B.-J. Lee, “Modified embedded-atom method interatomic potential for the Fe-Al system,” *Journal of Physics: Condensed Matter*, vol. 22, no. 17, p. 175702, 2010.
- [182] P. Chartrand and A. D. Pelton, “Thermodynamic evaluation and optimization of the LiF-NaF-KF-MgF₂-CaF₂ system using the modified quasi-chemical model,” *Metallurgical and Materials Transactions A*, vol. 32, no. 6, pp. 1385–1396, 2001.
- [183] A. Dogan and H. Arslan, “Comparative thermodynamic prediction of integral properties of six component, quaternary, and ternary systems,” *Metallurgical and Materials Transactions A*, vol. 46, no. 8, pp. 3753–3760, 2015.
- [184] P. Srinivasan, L. Nicola, and A. Simone, “Modeling pseudo-elasticity in NiTi: Why the MEAM potential outperforms the EAM-FS potential,” *Computational Materials Science*, vol. 134, pp. 145–152, 2017.
- [185] J.-P. Harvey and P. D. Asimow, “Current limitations of molecular dynamic simulations as probes of thermo-physical behavior of silicate melts,” *American Mineralogist*, vol. 100, no. 8-9, pp. 1866–1882, 2015.

- [186] S. Plimpton, “Fast parallel algorithms for short-range molecular dynamics,” Sandia National Labs., Albuquerque, NM (United States), Tech. Rep., 1993.
- [187] J. M. D. Lane, A. P. Thompson, and T. J. Vogler, “Enhanced densification under shock compression in porous silicon,” *Physical Review B*, vol. 90, no. 13, p. 134311, 2014.
- [188] J. H. Rose, J. R. Smith, F. Guinea, and J. Ferrante, “Universal features of the equation of state of metals,” *Physical Review B*, vol. 29, no. 6, p. 2963, 1984.
- [189] Y.-K. Kim, H.-K. Kim, W.-S. Jung, and B.-J. Lee, “Atomistic modeling of the Ti–Al binary system,” *Computational materials science*, vol. 119, pp. 1–8, 2016.
- [190] J. Hafner, “Bond-angle distribution functions in metallic glasses,” *Le Journal de Physique Colloques*, vol. 46, no. C9, pp. C9–69, 1985.
- [191] G. Kresse and J. Hafner, “Ab initio molecular dynamics for liquid metals,” *Physical review B*, vol. 47, no. 1, p. 558, 1993.
- [192] G. Kresse and J. Haffner, “Ab initio molecular-dynamics simulation of the liquid-metal–amorphous-semiconductor transition in germanium,” *Physical Review B*, vol. 49, no. 20, p. 14251, 1994.
- [193] G. Kresse and J. Furthmuller, “Efficiency of ab-initio total energy calculations for metals and semiconductors using a plane-wave basis set,” *Computational materials science*, vol. 6, no. 1, pp. 15–50, 1996.
- [194] G. Kresse and J. Furthmuler, “Efficient iterative schemes for ab initio total-energy calculations using a plane-wave basis set,” *Physical review B*, vol. 54, no. 16, p. 11169, 1996.
- [195] P. E. Blöchl, “Projector augmented-wave method,” *Physical review B*, vol. 50, no. 24, p. 17953, 1994.
- [196] G. Kresse and D. Joubert, “From ultrasoft pseudopotentials to the projector augmented-wave method,” *Physical review b*, vol. 59, no. 3, p. 1758, 1999.
- [197] J. P. Perdew, K. Burke, and M. Ernzerhof, “Generalized gradient approximation made simple,” *Physical review letters*, vol. 77, no. 18, p. 3865, 1996.
- [198] J.-P. Perdew, K. Burke, and M. Ernzerhof, “Generalized Gradient Approximation Made Simple [Phys. Rev. Lett. 77, 3865 (1996)],” *Phys. Rev. Lett.*, vol. 78, pp. 1396–1396, Feb 1997. [Online]. Available: <https://link.aps.org/doi/10.1103/PhysRevLett.78.1396>

- [199] S. Banerjee, “Nuclear Applications: Zirconium Alloys,” in *Encyclopedia of Materials: Science and Technology*, K. J. Buschow, R. W. Cahn, M. C. Flemings, B. Ilschner, E. J. Kramer, S. Mahajan, and P. Veyssi re, Eds. Oxford: Elsevier, 2001, pp. 6287–6299. [Online]. Available: <https://www.sciencedirect.com/science/article/pii/B0080431526011177>
- [200] D. Deardorff and E. T. Hayes, “Melting point determination of hafnium, zirconium, and titanium,” *JOM*, vol. 8, no. 5, pp. 509–510, 1956.
- [201] J. Ding, E. Ma, M. Asta, and R. O. Ritchie, “Second-nearest-neighbor correlations from connection of atomic packing motifs in metallic glasses and liquids,” *Scientific reports*, vol. 5, no. 1, pp. 1–9, 2015.
- [202] J. A. van Meel, L. Filion, C. Valeriani, and D. Frenkel, “A parameter-free, solid-angle based, nearest-neighbor algorithm,” *The Journal of chemical physics*, vol. 136, no. 23, p. 234107, 2012.
- [203] S. Wang, M. Kramer, M. Xu, S. Wu, S. Hao, D. Sordelet, K. Ho, and C. Wang, “Experimental and ab initio molecular dynamics simulation studies of liquid Al₆₀Cu 40 alloy,” *Physical Review B*, vol. 79, no. 14, p. 144205, 2009.
- [204] W. Zhou, L. Liu, B. Li, Q. Song, and P. Wu, “Structural, elastic, and electronic properties of Al-Cu intermetallics from first-principles calculations,” *Journal of electronic materials*, vol. 38, no. 2, pp. 356–364, 2009.
- [205] D. Nguyen-Manh and D. Pettifor, “Electronic structure, phase stability and elastic moduli of AB transition metal aluminides,” *Intermetallics*, vol. 7, no. 10, pp. 1095–1106, 1999.
- [206] M. Mihalkovic and M. Widom, “Alloy database,” URL <http://alloy.phys.cmu.edu>, 2017.
- [207] B. Karki, G. Ackland, and J. Crain, “Elastic instabilities in crystals from ab initio stress-strain relations,” *Journal of Physics: Condensed Matter*, vol. 9, no. 41, p. 8579, 1997.
- [208] Y. Zhang and E. J. Maginn, “A comparison of methods for melting point calculation using molecular dynamics simulations,” *The Journal of chemical physics*, vol. 136, no. 14, p. 144116, 2012.

- [209] D. Kawase, A. P. Tsai, A. Inoue, and T. Masumoto, “Crystallization on supercooled liquid in metallic Zr-Cu-Al glasses,” *Applied physics letters*, vol. 62, no. 2, pp. 137–139, 1993.
- [210] W. Cassada, G. Shiflet, and S. Poon, “Quasicrystalline grain boundary precipitates in aluminium alloys through solid-solid transformations,” *Journal of Microscopy*, vol. 146, no. 3, pp. 323–335, 1987.
- [211] M. Rappaz, P. Jarry, G. Kurtuldu, and J. Zollinger, “Solidification of metallic alloys: Does the structure of the liquid matter?” *Metallurgical and Materials Transactions A*, vol. 51, no. 6, pp. 2651–2664, 2020.
- [212] M. Vimal, S. Sandfeld, and A. Prakash, “Grain segmentation in atomistic simulations using orientation-based iterative self-organizing data analysis,” *Materialia*, p. 101314, 2022.
- [213] L. A. Gowsalya and M. E. Afshan, “Heat Transfer Studies on Solidification of Casting Process,” in *Casting Processes and Modelling of Metallic Materials*. IntechOpen, 2021.
- [214] M. Hillert, “The compound energy formalism,” *Journal of Alloys and Compounds*, vol. 320, no. 2, pp. 161–176, 2001.
- [215] P. Lafaye, K. Oishi, M. Bourdon, and J.-P. Harvey, “Crystal chemistry and thermodynamic modelling of the $\text{Al}_{13}(\text{Fe},\text{TM})_4$ solid solutions (TM = Co, Cr, Ni, Pt),” *Journal of Alloys and Compounds*, p. 165779, 2022. [Online]. Available: <https://www.sciencedirect.com/science/article/pii/S0925838822021703>
- [216] N.-A. Vahabzadeh, A. Boochani, S. M. Elahi, and H. Akbari, “Structural, Half-Metallic, Optical, and Thermoelectric Study on the Zr_2Tix (X= Al, Ga, Ge, Si) Heuslers: by DFT,” *Silicon*, vol. 11, no. 1, pp. 501–511, 2019.
- [217] M. De Jong, W. Chen, T. Angsten, A. Jain, R. Notestine, A. Gamst, M. Sluiter, C. Krishna Ande, S. Van Der Zwaag, J. J. Plata *et al.*, “Charting the complete elastic properties of inorganic crystalline compounds,” *Scientific data*, vol. 2, no. 1, pp. 1–13, 2015.
- [218] J.-Y. Park, I.-H. Kim, A. T. Motta, C. J. Ulmer, M. A. Kirk Jr, E. A. Ryan, and P. M. Baldo, “Irradiation-induced disordering and amorphization of Al_3Ti -based intermetallic compounds,” *Journal of Nuclear Materials*, vol. 467, pp. 601–606, 2015.

- [219] T. Atamanenko, D. Eskin, M. Sluiter, and L. Katgerman, "On the mechanism of grain refinement in Al–Zr–Ti alloys," *Journal of Alloys and Compounds*, vol. 509, no. 1, pp. 57–60, 2011.
- [220] X.-G. Chen and M. Fortier, "TiAlSi intermetallic formation and its impact on the casting processing in Al–Si alloys," *Journal of Materials Processing Technology*, vol. 210, no. 13, pp. 1780–1786, 2010.
- [221] D. Granger, "Microstructure control in ingots of aluminum alloys with an emphasis on grain refinement," in *Essential Readings in Light Metals*. Springer, 2016, pp. 354–365.
- [222] G. K. Sigworth and T. A. Kuhn, "Grain refinement of aluminum casting alloys," *International Journal of Metalcasting*, vol. 1, no. 1, pp. 31–40, 2007.
- [223] K. Kashyap and T. Chandrashekar, "Effects and mechanisms of grain refinement in aluminium alloys," *Bulletin of Materials Science*, vol. 24, no. 4, pp. 345–353, 2001.
- [224] M. Kearns and P. Cooper, "Effects of solutes on grain refinement of selected wrought aluminium alloys," *Materials science and technology*, vol. 13, no. 8, pp. 650–654, 1997.
- [225] A. L. Greer, P. S. Cooper, M. W. Meredith, W. Schneider, P. Schumacher, J. A. Spittle, and A. Tronche, "Grain refinement of aluminium alloys by inoculation," *Advanced Engineering Materials*, vol. 5, no. 1-2, pp. 81–91, 2003.
- [226] B. Murty, S. Kori, and M. Chakraborty, "Grain refinement of aluminium and its alloys by heterogeneous nucleation and alloying," *International Materials Reviews*, vol. 47, no. 1, pp. 3–29, 2002.
- [227] T. Quested, "Understanding mechanisms of grain refinement of aluminium alloys by inoculation," *Materials Science and Technology*, vol. 20, no. 11, pp. 1357–1369, 2004.
- [228] H. Toda, T. Kobayashi, and A. Takahashi, "Mechanical analysis of toughness degradation due to premature fracture of coarse inclusions in wrought aluminium alloys," *Materials Science and Engineering: A*, vol. 280, no. 1, pp. 69–75, 2000.
- [229] M. Baruah and A. Borah, "Processing and precipitation strengthening of 6xxx series aluminium alloys: A review," *International Journal of Materials Science*, vol. 1, no. 1, pp. 40–48, 2020.
- [230] W. B. Lee, Y. Yeon, and S. Jung, "The improvement of mechanical properties of friction-stir-welded A356 al alloy," *Materials Science and Engineering: A*, vol. 355, no. 1-2, pp. 154–159, 2003.

- [231] M.-S. Jo, Y.-H. Cho, J.-M. Lee, S.-H. Kim, J.-Y. Kang, J.-G. Jung, S.-B. Kim, and J.-i. Jang, “A new Zr-rich intermetallic phase in an Al-14Si-3Cu-4.5 Ni casting alloy with trace additions of Zr,” *Intermetallics*, vol. 117, p. 106667, 2020.
- [232] I. Polmear, *Light alloys: from traditional alloys to nanocrystals*. Elsevier, 2005.
- [233] S. K. Das, “Emerging trends in aluminum recycling: Reasons and responses,” *Light Metals*, vol. 4, pp. 911–916, 2006.
- [234] F. Zupanič, M. Steinacher, S. Žist, and T. Bončina, “Microstructure and properties of a novel Al-Mg-Si alloy AA 6086,” *Metals*, vol. 11, no. 2, p. 368, 2021.
- [235] G. Sha, K. O’Reilly, B. Cantor, J. Worth, and R. Hamerton, “Growth related metastable phase selection in a 6xxx series wrought Al alloy,” *Materials Science and Engineering: A*, vol. 304, pp. 612–616, 2001.
- [236] N. Kuijpers, W. Kool, P. Koenis, K. Nilsen, I. Todd, and S. Van der Zwaag, “Assessment of different techniques for quantification of α -Al (FeMn) Si and β -AlFeSi intermetallics in AA 6xxx alloys,” *Materials Characterization*, vol. 49, no. 5, pp. 409–420, 2002.
- [237] M. Kral, P. Nakashima, and D. Mitchell, “Electron microscope studies of Al-Fe-Si intermetallics in an Al-11 Pct Si alloy,” *Metallurgical and Materials Transactions A*, vol. 37, no. 6, pp. 1987–1997, 2006.
- [238] X. Liu, H.-L. Jia, C. Wang, X. Wu, M. Zha, and H.-Y. Wang, “Enhancing mechanical properties of twin-roll cast Al-Mg-Si-Fe alloys by regulating Fe-bearing phases and macro-segregation,” *Materials Science and Engineering: A*, vol. 831, p. 142256, 2022.
- [239] P. P. Seth, O. Parkash, and D. Kumar, “Structure and mechanical behavior of in situ developed Mg₂Si phase in magnesium and aluminum alloys—a review,” *RSC advances*, vol. 10, no. 61, pp. 37 327–37 345, 2020.
- [240] C. Amador, J. Hoyt, B. Chakoumakos, and D. De Fontaine, “Theoretical and experimental study of relaxations in Al₃Ti and Al₃Zr ordered phases,” *Physical review letters*, vol. 74, no. 24, p. 4955, 1995.
- [241] T. Atamanenko, D. Eskin, L. Zhang, and L. Katgerman, “Criteria of grain refinement induced by ultrasonic melt treatment of aluminum alloys containing Zr and Ti,” *Metallurgical and Materials Transactions A*, vol. 41, no. 8, pp. 2056–2066, 2010.

- [242] S. Zhu, J.-Y. Yao, L. Sweet, M. Easton, J. Taylor, P. Robinson, and N. Parson, "Influences of nickel and vanadium impurities on microstructure of aluminum alloys," *Jom*, vol. 65, no. 5, pp. 584–592, 2013.
- [243] R. Boulechfar, H. Meradji, S. Ghemid, S. Drablia, and B. Bouhafs, "First principle calculations of structural, electronic and thermodynamic properties of $\text{Al}_3(\text{Ti}_x\text{V}_{1-x})$ alloy in D0_{22} and L1_2 structures," *Solid state sciences*, vol. 16, pp. 1–5, 2013.
- [244] G. Zhu, Y. Dai, D. Shu, J. Wang, and B. Sun, "Substitution behavior of Si in Al_3Ti (D0_{22}): a first-principles study," *Journal of Physics: Condensed Matter*, vol. 21, no. 41, p. 415503, 2009.
- [245] C. Yang, Z. Liu, Q. Zheng, Y. Cao, X. Dai, L. Sun, J. Zhao, J. Xing, and Q. Han, "Ultrasound assisted in-situ casting technique for synthesizing small-sized blocky Al_3Ti particles reinforced A356 matrix composites with improved mechanical properties," *Journal of Alloys and Compounds*, vol. 747, pp. 580–590, 2018.
- [246] D. Srinivasan and K. Chattopadhyay, "Non-equilibrium transformations involving L1_2 - Al_3Zr in ternary Al-X-Zr alloys," *Metallurgical and Materials Transactions A*, vol. 36, no. 2, pp. 311–320, 2005.
- [247] J. Wang, S.-L. Shang, Y. Wang, Z.-G. Mei, Y.-F. Liang, Y. Du, and Z.-K. Liu, "First-principles calculations of binary Al compounds: Enthalpies of formation and elastic properties," *Calphad*, vol. 35, no. 4, pp. 562–573, 2011.
- [248] P. Norby and A. N. Christensen, "Preparation and structure of Al_3Ti ," *Acta chemica scandinavica, Series A*, vol. 40, p. 157, 1986.
- [249] J. L. Cavazos and R. Colás, "Quench sensitivity of a heat treatable aluminum alloy," *Materials Science and Engineering: A*, vol. 363, no. 1-2, pp. 171–178, 2003.

APPENDIX A BINARY PHASE DIAGRAMS FOR THE STUDIED ALUMINUM ALLOYING ELEMENTS

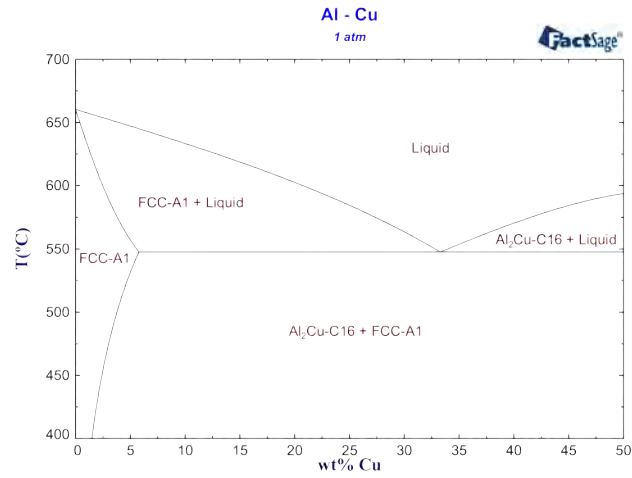


Figure A.1 Al-Cu phase diagram.

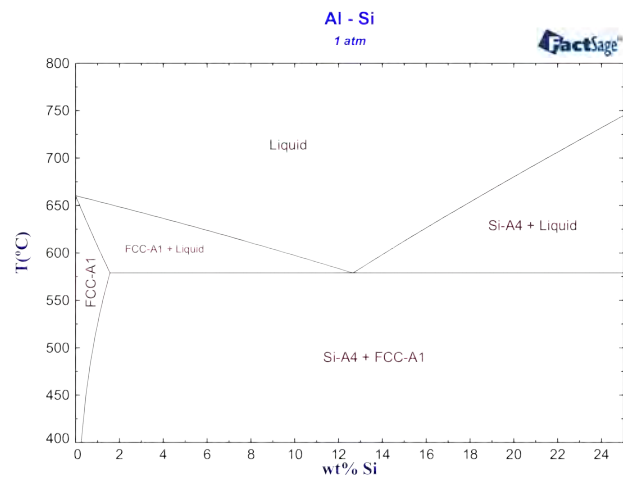


Figure A.2 Al-Si phase diagram.

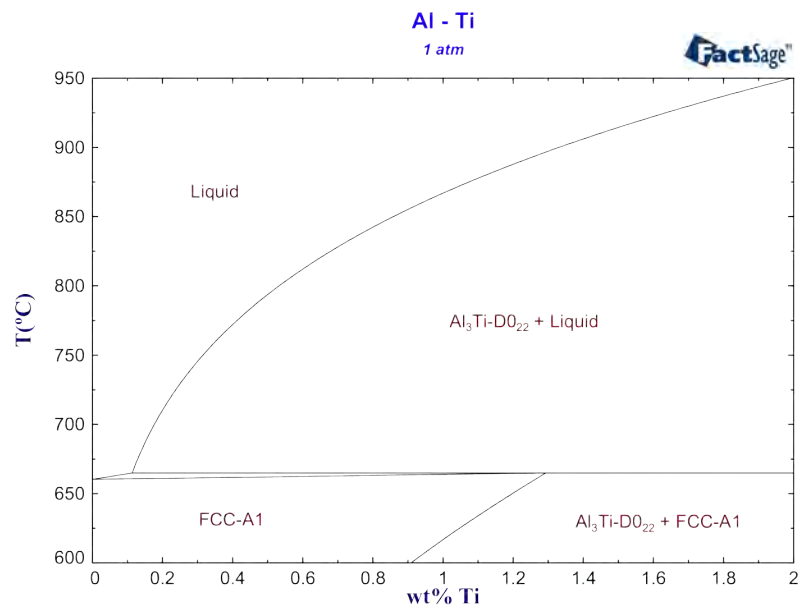


Figure A.3 Al-Ti phase diagram.

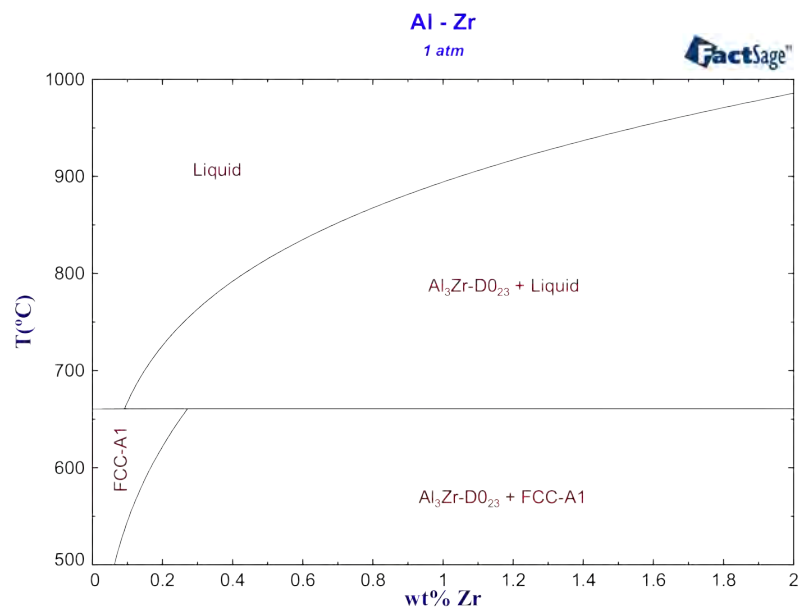


Figure A.4 Al-Zr phase diagram.

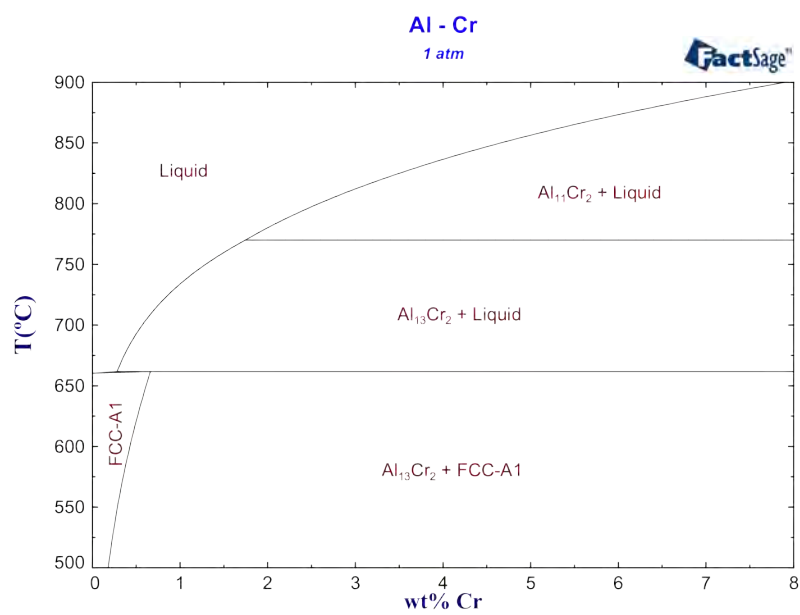


Figure A.5 Al-Cr phase diagram.

APPENDIX B EXAMPLE OF INPUT FILE FOR LAMMPS

This is an example of an input file for the thermal program for the solidification of an Al-Cr alloy, which are presented in Chapter 5. A brief description of the different parts of the script is presented in red and blue.

```

1 #-----Thermal program-----
2 dimension 3
3 units metal
4 boundary p p p
5 atom_style atomic
6 read_data Al-Cr_0.1%-Cr.dat
7
8 #-----Interatomic potential-----
9 pair_style meam/c
10 pair_coeff * * AlCr.library.meam Al Cr AlCr.parameter.meam Al Cr
11
12 #-----Requested properties-----
13 variable N equal step
14 variable pote equal pe
15 variable kine equal ke
16 variable Etotal equal etotal
17 variable Enth equal enthalpy
18 variable T equal temp
19 variable Press equal press
20 variable V equal vol
21 variable longx equal lx
22 variable rdfoutput equal 10000
23 compute RDFseparate all rdf 50 1 1 2 2 1 2 2
24 compute RDFtotal all rdf 50 * *
25
26 #-----Additional settings-----
27 timestep 0.001
28 thermo 10000
29 neighbor 0.6 bin
30 neigh_modify every 5 delay 0 check yes
31 velocity all create 2.5 8225577 dist gaussian
32 fix 1 all ave/time ${rdfoutput} 1 ${rdfoutput} c_RDFseparate[*] file separate.rdf mode vector
33 fix 2 all ave/time ${rdfoutput} 1 ${rdfoutput} c_RDFtotal[*] file total.rdf mode vector
34
35 #-----Output settings-----
36 fix extra all print 1000 "$[N] $[T] $[V] ${pote} ${kine} ${Etotal} ${Enth} ${Press} ${longx}" file data
37 dump 1 all custom 10000 a*.dump.Al-Cr.dat id type x y z
38
39 #-----Initial equilibration at 2.5 K-----
40 fix 3 all nvt temp 2.5 2.5 2 drag 0.2
41 run 100000
42 unfix 3
43
44 #-----Heating from 2.5 K to 2000 K-----
45 fix 3 all npt temp 2.5 2000 10 iso 0 0 10
46 run 1200000
47 unfix 3
48
49 #-----NVT/NTP Mixing at 2000 K-----
50 fix 3 all nvt temp 2000 2000 10
51 run 500000
52 unfix 3
53 fix 3 all npt temp 2000 2000 10 iso 0 0 10
54 run 500000
55 unfix 3
56
57 #-----Cooling at -1 K/ps-----
58 fix 3 all npt temp 2000 300 10 iso 0 0 10
59 run 1700000
60 unfix 3
61
62 #-----Final relaxation-----
63 fix 3 all npt temp 300 300 10 iso 0 0 10
64 run 3000000
65 unfix 3

```

} Defining a simulation in three dimensions with periodic boundary conditions and with "metal" units (i.e., mass = grams/mole, distance = Angstroms, time = picoseconds, energy = eV, force = eV/Angstrom, temperature = Kelvin, pressure = bars, etc.)
} Initial positions' file
} Entry for the interatomic potential
} Simulation step
} Potential energy
} Kinetic energy
} Total energy
} Enthalpy
} Temperature
} Pressure
} Volume
} Size of the simulation box in the "x" axis
} Average value for Radial distribution function (RDF)
} Partial RDF
} Total RDF
} Simulation time step in fs
} Print the thermodynamic properties every 10 000 simulation steps
} Neighbor list settings
} Imposed initial velocity for 2.5 K
} RDF settings
} Export properties every 1 000 simulation steps
} Export position files every 10 000 simulation steps
} Equilibration into the NVT ensemble at 2.5 K for 0.5 ns.
} NPT heating at 1.66 K/s, thermostatting and barostatting the system every 10 simulation steps
} NPT and NPT equilibrations at 2 000K during 0.5 ns each, by thermostatting and barostatting the system every 10 simulation steps.
} Cooling into the NPT at -1K/ps, by thermostatting and barostatting the system every 10 simulation steps.
} Equilibration into the NPT at 300 K, by thermostatting and barostatting the system every 10 simulation steps.

Figure B.1 Example of thermal program for an Al-Cr alloy.